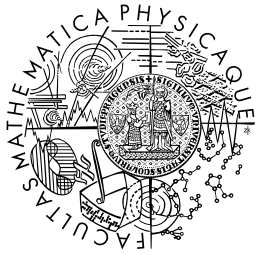

FACULTY
OF MATHEMATICS
AND PHYSICS
Charles University

MASTER THESIS

Jan Dvořák

Associative electron detachment in collision of negative anion

Institute of Theoretical Physics

Supervisor of the master thesis: doc. RNDr. Martin Čížek, PhD.

Study programme: Physics

Study branch: Theoretical Physics

Prague 2017

I declare that I carried out this master thesis independently, and only with the cited sources, literature and other professional sources.

I understand that my work relates to the rights and obligations under the Act No. 121/2000 Sb., the Copyright Act, as amended, in particular the fact that the Charles University has the right to conclude a license agreement on the use of this work as a school work pursuant to Section 60 subsection 1 of the Copyright Act.

In ..... date ..... signature of the author

Title: Associative electron detachment in collision of negative anion

Author: Jan Dvořák

Institute: Institute of Theoretical Physics

Supervisor: doc. RNDr. Martin Čížek, PhD., Institute of Theoretical Physics

Abstract: Low-energy resonant processes in collisions of electrons, atoms, ions and molecules significantly contributed to the evolution of the early Universe. Much attention has not yet been paid to processes involving lithium atoms and ions. In this thesis, we present the theoretical description of two associative detachment processes of Li with H^- and H with Li^- within the nonlocal resonant theory. The nonlocal resonant models were constructed from potential energy curves computed by the MOLPRO package of *ab initio* programs and from electron-molecule scattering data obtained from R-matrix calculations by the UK molecular R-matrix suite of codes. The Lippman-Schwinger equation describing the nuclear motion was solved by the Schwinger-Lanczos algorithm. We developed a new method, which is based on the singular value decomposition method and separates the coupling potential. We predict several orders of magnitude difference between the temperature-dependent rate constants of the studied collisions at temperatures below 1000 K.

Keywords: nonlocal resonant theory, associative detachment collisions, LiH

I gratefully thank my supervisor doc. RNDr. Martin Čížek, PhD. for all his support, useful advices and inspiring discussions. I really appreciate all his help.

I would also like to thank RNDr. Karel Houfek, PhD. for providing me data from quantum chemistry and electron-molecule scattering.

Contents

Introduction

Resonant processes of electrons, atoms, ions and molecules play an important role in many fields of physics, such as plasma physics, astrophysics, laser physics and so on. The proper theoretical description of such processes is desired.

Our theoretical work is primarily motivated by astrophysical applications in the description of the early Universe in the so-called recombination era. The recombination era was a time period in the evolution of our Universe when its temperature decreased low enough to enable a survival of atoms. During this period, the Universe was changing from a fully ionized plasma to a nearly neutral gas. Chemical reactions, which at first involves free electrons, atoms and ions and later molecules, started to occur. The atomic and molecular processes contributed to the formation of the first stars since they served together with the adiabatic expansion of the Universe as cooling mechanisms of gravitational collapse. Before the recombination began, only few species of nuclei existed. Most protons and neutrons occurred as nuclei of H and ^{4}He with trace amounts of deuterium, ^{3}He, and ^{7}Li. The processes involving lithium atoms and ions were often ignored in the past. Even models that included lithium chemistry used only rough estimates of rate constants. Therefore, their contribution to the evolution of the early Universe is not fully understand.

In this thesis, we present the theoretical description of two associative detachment processes of Li with H^- and H with Li^- within the nonlocal resonant theory. These reactive collisions have been studied to our knowledge neither from the theoretical nor experimental point of view so far. The nonlocal resonant theory provides the most advanced description of coupling of electronic and nuclear motions in the presence of electronic continuum. Specifically, we construct the nonlocal resonant models from *ab initio* quantum chemistry data and electron-molecule scattering data provided by K. Houfek, and we calculate the corresponding cross sections and rate constants. We discuss in detail the sensitivity of the results to various numerical and physical parameters. We also develop a new method which approximates the discrete-state-continuum-coupling potential, a function of energy and space variables, as the sum of separable terms.

More detailed information about chemistry in the early Universe can be found in review papers by Lepp et al. [1] and by Glover et al. [2]. The nonlocal resonant theory is well explained in the review paper by Domcke [3] and book [4] and in references therein.

Now, we briefly describe the content of individual chapters of the thesis. We give the brief derivation of the nonlocal resonant theory in general case in the first chapter. In the second half of this chapter, we focus more on associative detachment processes involving diatomic molecules. In the second chapter, we discuss the *ab initio* data from quantum chemistry calculations and from electron-molecule scattering. Then, these data are used in the construction of the nonlocal resonant models for both of the studied collisions. We introduce the proposed separation method in the third chapter. We also test the method on the associative detachment process of H with Br^-. The fourth and fifth chapters are devoted to the analysis of the obtained results for both the studied reactive processes. Their sensitivity to the various parameters is discussed in detail.

1. Description of low-energy collisions

1.1 Introduction

In the first chapter, we look into the description of electron-molecule collisions within the nonlocal resonant theory. The first half is dedicated to the brief derivation of the general theory. The detailed derivation can be found in the review paper by Domcke [3] and in book [4] (Chapters 4 and 5). The mentioned paper and book serve as the primary references for this chapter. The second part of the first chapter mainly focuses on the treatment of associative detachment processes in the case of diatomic molecules and the construction of the nonlocal resonant model for a given collision process.

We use atomic units ($m_\mathrm{e} = 1$, $|e| = 1$, $\hbar = 1$, $1/4\pi\epsilon_0 = 1$) in the entire thesis if it is not stated otherwise.

1.2 Processes of interest

Specifically, the nonlocal resonant theory is suitable for the description of the following low-energy processes, which involve a neutral molecule AB (A and B can be polyatomic parts):

- vibrational excitation (VE)

$$\mathrm{e}^- + \mathrm{AB}(\nu_\mathrm{i}) \rightarrow \mathrm{e}^- + \mathrm{AB}(\nu_\mathrm{f}), \tag{1.1}$$

  where ν_i and ν_f denote the initial and final vibrational states respectively

- dissociative attachment (DA)

$$\mathrm{e}^- + \mathrm{AB} \rightarrow \mathrm{A}^- + \mathrm{B} \tag{1.2}$$

- collision detachment (CD)

$$\mathrm{e}^- + \mathrm{AB} \rightarrow \mathrm{e}^- + \mathrm{A} + \mathrm{B} \tag{1.3}$$

and the closely related inverse processes to DA and CD

- associative detachment (AD)

$$\mathrm{A}^- + \mathrm{B} \rightarrow \mathrm{e}^- + \mathrm{AB} \tag{1.4}$$

- three-particle recombination

$$\mathrm{e}^- + \mathrm{A} + \mathrm{B} \rightarrow \mathrm{e}^- + \mathrm{AB}. \tag{1.5}$$

1.3 Nonlocal resonant theory

1.3.1 Projection-operator approach

At the beginning, we outline the basic physical situation of the processes of interest. In such molecular systems, a resonance state exists embedded in the continuum for some nuclear configurations. This resonance typically disappears for other configurations and it becomes a bound anion state, which causes the failure of the Born-Oppenheimer approximation. The resonance is a quasi-stable state, which means that the electron can be released from the system or captured into the system depending on the type of the studied collision process. In fact, a virtual state or broad resonance may be present in the system instead of the resonance state.[1] The so-called discrete state represents both the resonance (or the virtual state) at some nuclear configurations and the bound anion state at other positions of the nuclei. The discrete state is constructed so that the transition of the bound state to the resonance (or the virtual state) is smooth. Then, the Born-Oppenheimer approximation can be restored for the discrete state.

The resonance can not be described by a square integrable function, and so, it does not belong to the electronic Hilbert space. However, it can be well approximated by such a function. Let us denote the discrete state by $|\mathrm{d}\rangle$ with a wave function $\varphi_\mathrm{d}(\boldsymbol{r};\boldsymbol{R}) = \langle \boldsymbol{r}|\mathrm{d}\rangle$, where $\boldsymbol{r}$ denotes coordinates of the incoming electron. The wave function also parametrically depends on coordinates $\boldsymbol{R}$ of all nuclei.

The Hamilton operator of an electron-molecule collision is given by

$$H = T_\mathrm{N} + V_0(\boldsymbol{R}) + H_\mathrm{el}, \tag{1.6}$$

where T_N is the kinetic energy of the nuclei, $V_0(\boldsymbol{R})$ is the potential energy surface of the molecule AB in the ground electronic state, and H_el is the electronic Hamilton operator consisting of the kinetic energy of the incoming electron and an effective interaction between the incoming electron and molecule. The interaction is of many body (many electron) nature, but can be described by an effective single electron potential (optical potential) [3, 5].

The nonlocal resonant theory is usually derived using the projection-operator approach developed by Feshbach [6] for nuclear reactions and later used by Fano [7] in atomic physics. In this approach, the electronic Hilbert space and then the full Hilbert space are divided into two subspaces, a resonant part and a background part, by projection-operators Q and P defined by

$$Q = |\mathrm{d}\rangle\langle\mathrm{d}|, \;\; P = I - Q. \tag{1.7}$$

The operator P can also be expressed using background scattering states $|\boldsymbol{k}^{(+)}\rangle$ with wave functions $\varphi^{(+)}_{\boldsymbol{k}}(\boldsymbol{r};\boldsymbol{R}) = \langle \boldsymbol{r}|\boldsymbol{k}^{(+)}\rangle$, where $\boldsymbol{k}$ is the wave vector of the incoming electron and its magnitude equals k. These states diagonalize the background part of the electronic Hamiltonian

$$PH_\mathrm{el}P|\boldsymbol{k}^{(+)}\rangle = \frac{1}{2}k^2|\boldsymbol{k}^{(+)}\rangle. \tag{1.8}$$

[1] Hence, the title of the theory may be misleading.

We assume the energy normalization of the scattering states

$$\langle \boldsymbol{k}^{(+)} | \boldsymbol{k'}^{(+)} \rangle = \delta(\epsilon_k - \epsilon_{k'}) \delta_2(\boldsymbol{\Omega}_k - \boldsymbol{\Omega}_{k'}), \tag{1.9}$$

where $\epsilon_k = k^2/2$ is electron energy, $\boldsymbol{\Omega}_k = \boldsymbol{k}/k$ denotes the direction vector. Then, the P operator has the form

$$P = \int \mathrm{d}\epsilon_k \mathrm{d}\boldsymbol{\Omega}_k |\boldsymbol{k}^{(+}\rangle\langle\boldsymbol{k}^{(+}|. \tag{1.10}$$

Further, we use the following notation for matrix elements of the electronic Hamiltonian:

- the discrete-state potential

$$V_\mathrm{d}(\boldsymbol{R}) = V_0(\boldsymbol{R}) + \langle \mathrm{d}|H_\mathrm{el}|\mathrm{d}\rangle \tag{1.11}$$

- the discrete-state-continuum-coupling potential

$$V^{(+)}_{\mathrm{d}\boldsymbol{k}}(\boldsymbol{R}) = \langle \mathrm{d}|H_\mathrm{el}|\boldsymbol{k}^{(+)}\rangle \tag{1.12}$$

- the diagonal background part

$$\begin{aligned} V_{\boldsymbol{k}\boldsymbol{k'}}(\boldsymbol{R}) &= \langle \boldsymbol{k}^{(+)}|(V_0(\boldsymbol{R}) + H_\mathrm{el})|\boldsymbol{k'}^{(+)}\rangle \\ &= (V_0(\boldsymbol{R}) + \epsilon_k)\, \delta(\epsilon_k - \epsilon_{k'}) \delta_2(\boldsymbol{\Omega}_k - \boldsymbol{\Omega}_{k'}), \end{aligned} \tag{1.13}$$

where the diagonal form comes from Equation (1.8). Depending on the studied process, the coupling potential controls the electron release into the continuum or the electron capture into the anionic state.

If we choose the discrete state properly, we can still use the Born-Oppenheimer approximation

$$\frac{\partial \varphi_\mathrm{d}(\boldsymbol{r};\boldsymbol{R})}{\partial \boldsymbol{R}} \simeq 0, \;\; \frac{\partial \varphi^{(+)}_{\boldsymbol{k}}(\boldsymbol{r};\boldsymbol{R})}{\partial \boldsymbol{R}} \simeq 0. \tag{1.14}$$

These assumptions define the so-called diabatic approximation.

Further, we extent the Q and P operators to the full Hilbert space, which consists of the electronic and nuclear part,

$$Q = \int \mathrm{d}\boldsymbol{R} |\boldsymbol{R}\rangle Q_\mathrm{el}(\boldsymbol{R}) \langle \boldsymbol{R}|, \tag{1.15}$$

$$P = \int \mathrm{d}\boldsymbol{R} |\boldsymbol{R}\rangle P_\mathrm{el}(\boldsymbol{R}) \langle \boldsymbol{R}|, \tag{1.16}$$

where the electronic operators Q_el and P_el are those defined earlier by Formulas (1.7). Equation (1.14) implies the following commutation relations

$$[T_\mathrm{N}, Q] = [T_\mathrm{N}, P] = 0. \tag{1.17}$$

The full Hamiltonian is given in the basis constructed from vectors $|\mathrm{d}\rangle$, $|\boldsymbol{k}^{(+)}\rangle$ by

$$\begin{aligned} H =& |\mathrm{d}\rangle \left(T_\mathrm{N} + V_\mathrm{d}(R)\right) \langle \mathrm{d}| \\ &+ \int \mathrm{d}\epsilon_k \mathrm{d}\boldsymbol{\Omega}_k |\boldsymbol{k}^{(+)}\rangle \left(T_\mathrm{N} + V_0(R) + \frac{1}{2}k^2\right) \langle \boldsymbol{k}^{(+)}| \\ &+ \left(\int \mathrm{d}\epsilon_k \mathrm{d}\boldsymbol{\Omega}_k |\mathrm{d}\rangle V^{(+)}_{\mathrm{d}\boldsymbol{k}} \langle \boldsymbol{k}^{(+)}| + \mathrm{h.c.} \right). \end{aligned} \tag{1.18}$$

1.3.2 Equation for the nuclear motion

To derive the equation describing the relative motion of the nuclei in the Q subspace, we rewrite the full Hamiltonian given by Formula (1.6) into the suitable form for the application of scattering theory

$$H = H_0 + V \tag{1.19}$$

with

$$H_0 = H_{\mathrm{Q}} + H_{\mathrm{P}}, \tag{1.20}$$

$$V = PH_{\mathrm{el}}Q + QH_{\mathrm{el}}P = H_{\mathrm{PQ}} + H_{\mathrm{QP}}, \tag{1.21}$$

where we introduce the notation $H_{\mathrm{Q}} = QHQ$, $H_{\mathrm{P}} = PHP$, $H_{\mathrm{PQ}} = PHQ$, and $H_{\mathrm{QP}} = QHP$. The second equality in Formula (1.21) comes from commutation relations (1.17) and from the orthogonality of the Q and P subspaces, that is $QP = PQ = 0$. The Lippman-Schwinger equation with Hamiltonian (1.19) reads

$$|\Psi^{(+)}\rangle = |\Phi^{(+)}\rangle + (E - H_0 + \mathrm{i}\eta)^{-1}\, V|\Psi^{(+)}\rangle, \tag{1.22}$$

where $|\Psi^{(+)}\rangle$ depends on both nuclear and electronic degrees of freedom, $|\Phi^{(+)}\rangle$ characterizes the initial state (electron-molecule collision or atom-ion collision), η is a small positive parameter.

After substitution of H_0 and V defined by Formulas (1.20) and (1.21) into Equation (1.22), we multiply the resulting equation by Q and P operators. So, we obtain the two following equations

$$Q|\Psi^{(+)}\rangle = Q|\Phi^{(+)}\rangle + G_{\mathrm{Q}}H_{\mathrm{QP}}P|\Psi^{(+)}\rangle, \tag{1.23}$$

$$P|\Psi^{(+)}\rangle = P|\Phi^{(+)}\rangle + G_{\mathrm{P}}H_{\mathrm{PQ}}Q|\Psi^{(+)}\rangle, \tag{1.24}$$

where

$$G_{\mathrm{Q}} = Q(E - H_Q + i\eta)^{-1}Q, \tag{1.25}$$

$$G_{\mathrm{P}} = P(E - H_P + i\eta)^{-1}P. \tag{1.26}$$

Next, we replace the term $P|\Psi^{(+)}\rangle$ in Equation (1.23) by the right-hand side of Equation (1.24), which reduces the considered scattering problem in the full Hilbert space to the scattering problem in the small subspace Q

$$Q|\Psi^{(+)}\rangle = Q|\Phi^{(+)}\rangle + G_{\mathrm{Q}}H_{\mathrm{QP}}P|\Phi^{(+)}\rangle + G_{\mathrm{Q}}H_{\mathrm{QP}}G_{\mathrm{P}}H_{\mathrm{PQ}}Q|\Psi^{(+)}\rangle. \tag{1.27}$$

It can be shown that the Q-space part of the wave function is governed by the inhomogeneous Schrödinger equation with the effective Hamiltonian

$$H_{\mathrm{eff}} = H_{\mathrm{Q}} + H_{\mathrm{QP}}G_{\mathrm{P}}H_{\mathrm{PQ}}. \tag{1.28}$$

We can rewrite the effective Hamiltonian given above using the definitions of projectors Q (1.7) and P (1.10) and full Hamiltonian (1.18) into

$$H_{\text{eff}} = T_{\text{N}} + V_{\text{d}}(\boldsymbol{R}) + F(E), \tag{1.29}$$

where $F(E)$ is the energy-dependent complex nonlocal potential

$$F(E, \boldsymbol{R}, \boldsymbol{R'}) = \int \mathrm{d}\epsilon_k \mathrm{d}\boldsymbol{\Omega}_k V_{\mathrm{d}\boldsymbol{k}}^{(+)}(\boldsymbol{R}) \left(E - T_{\text{N}} - V_0(R) - \epsilon_k + \mathrm{i}\eta\right)^{-1} V_{\mathrm{d}\boldsymbol{k}}^{(+)*}(\boldsymbol{R'}). \tag{1.30}$$

Using the well-known formula from theory of distributions $(x + \mathrm{i}\eta)^{-1} = \text{p.v.}/x - \mathrm{i}\pi\delta(x)$, where p.v. denotes the Cauchy principal value, we separate $F(E)$ into the Hermitian and anti-Hermitian parts

$$F(E, \boldsymbol{R}, \boldsymbol{R'}) = \Delta(E - T_{\text{N}} - V_0(\boldsymbol{R}), \boldsymbol{R}, \boldsymbol{R'}) - \frac{\mathrm{i}}{2}\Gamma(E - T_{\text{N}} - V_0(\boldsymbol{R}), \boldsymbol{R}, \boldsymbol{R'}) \tag{1.31}$$

with

$$\Gamma(e, \boldsymbol{R}, \boldsymbol{R'}) = 2\pi \int \mathrm{d}\epsilon_k \mathrm{d}\boldsymbol{\Omega}_k V_{\mathrm{d}\boldsymbol{k}}^{(+)}(\boldsymbol{R}) \delta\left(e - \epsilon_k\right) V_{\mathrm{d}\boldsymbol{k}}^{(+)*}(\boldsymbol{R'}), \tag{1.32}$$

$$\Delta(e, \boldsymbol{R}, \boldsymbol{R'}) = \frac{1}{2\pi}\text{p.v.} \int \mathrm{d}\epsilon \frac{\Gamma(\epsilon, \boldsymbol{R}, \boldsymbol{R'})}{e - \epsilon}. \tag{1.33}$$

Furthermore, we introduce the notation

$$Q|\Psi^{(+)}\rangle = |\mathrm{d}\rangle\langle\mathrm{d}|\Psi^{(+)}\rangle_r = |\mathrm{d}\rangle|\psi^{(+)}\rangle, \tag{1.34}$$

where the subscript r indicates the integration only over electronic degrees of freedom. Thus, the state $|\psi^{(+)}\rangle$ depends only on nuclear coordinates. Rewriting Equation (1.27) with the use of the formulas above, we obtain the Lippman-Schwinger equation describing the nuclear degrees of freedom

$$|\psi^{(+)}\rangle = |\phi^{(+)}\rangle + G_{\text{Q}}^{(+)}(E) F(E) |\psi^{(+)}\rangle \tag{1.35}$$

where the state $|\phi^{(+)}\rangle$, which describes the initial state of the collision, is given by

$$|\phi^{(+)}\rangle = \langle\mathrm{d}|\Phi^{(+)}\rangle_r + \langle\mathrm{d}|G_{\text{Q}} H_{\text{QP}} P|\Phi^{(+)}\rangle_r, \tag{1.36}$$

and with the Green's function

$$G_{\text{Q}}^{(+)}(E) = (E - T_{\text{N}} - V_{\text{d}}(\boldsymbol{R}) + i\eta)^{-1}. \tag{1.37}$$

In the case of the electron-molecule collision e^-+AB (denoted by channel I), the initial state is represented by

$$|\Phi_{\text{I}}^{(+)}\rangle = |\nu_{\text{i}}\rangle|\boldsymbol{k}_{\text{i}}^{(+)}\rangle \Rightarrow |\phi_{\text{I}}^{(+)}\rangle = G_{\text{Q}}^{(+)} V_{\mathrm{d}\boldsymbol{k}_{\text{i}}}^{(+)} |\nu_{\text{i}}\rangle, \tag{1.38}$$

where $|\nu_\mathrm{i}\rangle$ stands for the initial vibrational state of the molecule AB and $\boldsymbol{k}_\mathrm{i}$ is the initial wave vector of the incoming electron.

For the ion-atom collision A^-+B (channel II) the initial state is given by

$$|\Phi_\mathrm{II}^{(+)}\rangle = |\mathrm{d}\rangle|\boldsymbol{K}_\mathrm{i}^{(+)}\rangle \Rightarrow |\phi_\mathrm{II}^{(+)}\rangle = |\boldsymbol{K}_\mathrm{i}^{(+)}\rangle, \tag{1.39}$$

where $\boldsymbol{K}_\mathrm{i}$ is the relative momentum of A^- and B in the centre of mass of the considered process, $|\boldsymbol{K}_\mathrm{i}^{(+)}\rangle$ is then the corresponding scattering state in the discrete-state potential $V_\mathrm{d}(\boldsymbol{R})$.

The resonant part of the T-matrix for the processes of interest reads

$$T_\mathrm{VE} = \langle\Phi_\mathrm{I}^{(-)}|PH_\mathrm{PQ}Q|\Psi^{(+)}\rangle = \langle\nu_\mathrm{f}|V_{\mathrm{d}\boldsymbol{k}_\mathrm{f}}^{(-)*}|\psi_\mathrm{I}^{(+)}\rangle, \tag{1.40}$$

$$T_\mathrm{DA} = \langle\Psi^{(-)}|QH_\mathrm{QP}P|\Phi^{(+)}\rangle = \langle\psi_\mathrm{II}^{(-)}|V_{\mathrm{d}\boldsymbol{k}_\mathrm{i}}^{(+)}|\nu_\mathrm{i}\rangle, \tag{1.41}$$

$$T_\mathrm{AD} = \langle\Phi_\mathrm{I}^{(-)}|PH_\mathrm{PQ}Q|\Psi^{(+)}\rangle = \langle\nu_\mathrm{f}|V_{\mathrm{d}\boldsymbol{k}_\mathrm{f}}^{(-)*}|\psi_\mathrm{II}^{(+)}\rangle, \tag{1.42}$$

where

$$\langle\psi_\mathrm{II}^{(-)}| = \langle\boldsymbol{K}_\mathrm{f}^{(-)}| + \langle\psi_\mathrm{II}^{(-)}|F(E)G_\mathrm{Q}^{(+)}(E). \tag{1.43}$$

The matrix element $V_{\mathrm{d}\boldsymbol{k}}^{(-)}$ is defined similarly as $V_{\mathrm{d}\boldsymbol{k}}^{(+)}$ given by Formula (1.12), but with the use of scattering states $|\boldsymbol{k}^{(-)}\rangle = \hat{\Omega}_-|\boldsymbol{k}\rangle$, where $\hat{\Omega}_-$ is the Møller operator.

1.4 Diatomic molecules and AD processes

The theory, which is briefly derived in the previous section, can be used to study the processes of interest, where AB is in general polyatomic molecule. Next, we restrict to the case of diatomic molecules since associative detachment collisions of an atom with a negative ion are the main topic of the remaining chapters.

Up to the end of the first chapter, we discuss equations and formulas which are actually needed to be solved in order to describe the mentioned collision problem. We present equations without any derivation. The detailed derivation can be again found in book [4] and references therein.

The nuclear degrees of freedom describing the relative motion reduce to one variable,[2] the internuclear distance R, in the case of diatomic molecules. The partial wave expansion is used in order to get rid of angular variables. The low-energy s-wave approximation for the released electron is also applied during the derivation. The approximation assumes that the angular momentum of the electron is negligible, and therefore, the angular momentum of the molecule is conserved. The nuclear wave function $\psi_J(R)$, which depends only on the internuclear distance R, is then the unique solution of

$$\psi_J(R) = \phi_J(R) + \int_0^\infty\int_0^\infty \mathrm{d}R'\mathrm{d}R'' G_J(E,R,R')F_J(E,R',R'')\psi_J(R''), \tag{1.44}$$

[2]The translational motion of the centre of mass is transformed away.

where J is the quantum number of the angular momentum of the molecule, $\phi_J(R)$ describes the initial partial scattering wave in the potential $V_\mathrm{d}(R)$, $G_J(E,R,R')$ and $F_J(E,R',R'')$ denote the radial J-terms in the partial wave expansion of the Green's function (for $V_\mathrm{d}(R)$) and nonlocal potential (1.31) respectively. There is no coupling of equations for different J because we neglect the electron angular momentum in the s-wave approximation.

The nonlocal term F_J appearing in Equation (1.44) can be expanded into eigenstates $\chi_{\nu J}$ (including the continuum) with energies $E_{\nu J}$ of the molecular Hamiltonian

$$\left[T_\mathrm{N} + V_0(R) + \frac{J(J+1)}{2\mu R^2}\right]\chi_{\nu J}(R) = E_{\nu J}\chi_{\nu J}(R), \tag{1.45}$$

where μ is the reduced mass of the molecule. The nonlocal term then reads

$$F_J(E,R,R') = \sum_\nu \chi_{\nu J}(R)\left[\Delta(E-E_{\nu J},R,R') - \frac{i}{2}\Gamma(E-E_{\nu J},R,R')\right]\chi_{\nu J}(R') \tag{1.46}$$

with

$$\Gamma(\epsilon,R,R') = 2\pi V_{\mathrm{d}\epsilon}(R)V^*_{\mathrm{d}\epsilon}(R'), \tag{1.47}$$

$$\Delta(\epsilon,R,R') = \frac{1}{2\pi}\mathrm{p.v.}\int \mathrm{d}e\frac{\Gamma(e,R,R')}{\epsilon-e}. \tag{1.48}$$

The function $\phi_J(R)$ describing the initial state in the ion-atom collision obeys the Lippman-Schwinger equation with the discrete-state potential $V_\mathrm{d}(R)$

$$\phi_J(R) = \hat{j}_J(KR) - \frac{2\mu}{K}\int \mathrm{d}R'\hat{j}_J(KR_<)\hat{h}_J(KR_>)V_\mathrm{d}(R')\phi_J(R'), \tag{1.49}$$

where $K=\sqrt{2\mu E}$, $R_< = \min(R,R')$, $R_> = \max(R,R')$, and the functions $\hat{j}_J$, $\hat{h}_J$ are the Ricatti-Bessel functions defined by Abramowitz and Stegun [8] on page 445.

If we are interested only in the total inelastic cross section, we can compute the cross section from formulas for scattering in a complex potential [9]. First, we define the scattering amplitude for each partial wave

$$a_J = -\frac{2\mu}{K}\langle\phi_J|F_J|\psi_J\rangle = -\frac{2\mu}{K}\int \mathrm{d}R\mathrm{d}R'\phi_J(R)F_J(E,R,R')\psi_J(R'). \tag{1.50}$$

Then, the inelastic cross section is given by

$$\sigma_\mathrm{inel}(E) = \frac{4\pi}{K^2}\sum_J(2J+1)\left[\mathrm{Im}(a_J) - |a_J|^2\right]. \tag{1.51}$$

In this case, the scattering amplitude already includes the sum over vibrational states of the molecule AB, that is over all possible final states of the molecule.

Another possibility of getting the total AD cross section is to sum contributions from individual vibrational states of the neutral molecule

$$sigma_\mathrm{AD}(E) = \frac{2\pi}{KE}\sum_J\sum_\nu(2J+1)\left|\langle\chi_{\nu J}|V_{\mathrm{d}K_\nu}|\psi_J\rangle\right|^2 \tag{1.52}$$

where K_ν is the magnitude of the momentum belonging to energy $E-E_{\nu J}$, that is $K_\nu = K_\nu^{(J)} = \sqrt{2\mu(E-E_{\nu J})}$. We sum over all accessible vibrational states, that is over those values of ν for particular J which fulfil $E_{\nu J} \le E$.

1.5 Nonlocal resonant model

The nonlocal resonant model (NRM) of the given collision process is fully defined by the following three functions:

- the potential $V_0(R)$ of the ground electronic state of the molecule AB,
- the discrete-state potential $V_\mathrm{d}(R)$ of the molecular anion AB^-,
- the energy-dependent discrete-state-continuum-coupling potential $V_{\mathrm{d}\epsilon}(R)$.

All these functions can be obtained from *ab initio* calculations, quantum chemistry and electron-molecule scattering. The eigenphase sum $\delta(\epsilon, R)$, provided by the electron scattering calculations, can be split into a resonant term $\delta_\mathrm{res}(\epsilon, R)$ and a background $\delta_\mathrm{bg}(\epsilon, R)$ term

$$\delta(\epsilon, R) = \delta_\mathrm{res}(\epsilon, R) + \delta_\mathrm{bg}(\epsilon, R). \tag{1.53}$$

The background part is a smooth function in both energy and internuclear distance. The resonant part is given by the generalized[3] Breit-Wigner formula [3]

$$\delta_\mathrm{res}(\epsilon, R) = -\tan^{-1}\left(\frac{\frac{1}{2}\Gamma(\epsilon, R)}{\epsilon - V_\mathrm{d}(R) + V_0(R) - \Delta(\epsilon, R)}\right), \tag{1.54}$$

where $\Gamma(\epsilon, R)$ and $\Delta(\epsilon, R)$ are the energy-dependent width and level-shift functions, which are obtained from operators (1.47) and (1.48) at $R' = R$.

At low energies the width function behaves according to the threshold law introduced by Wigner [10]. In the case of the molecule AB with no electric dipole moment, the threshold law reads

$$\Gamma \propto \epsilon^{(2l+1)/2}, \tag{1.55}$$

where l is the lowest integer allowed by the symmetry. If the molecule possesses any dipole moment, there are two possibilities. If the dipole moment D is subcritical, that is $D < D_\mathrm{crit} = 1.625$ D, the width then behaves in the vicinity of thresholds as follows [3, 4]

$$\Gamma \propto \epsilon^\alpha, \tag{1.56}$$

where α is the so-called threshold exponent depending on the internuclear distance

$$\alpha = \sqrt{d + \frac{1}{4}}, \tag{1.57}$$

where d is a dimensionless reduced dipole moment given by the lowest eigenvalue of an infinite-dimensional tridiagonal matrix [11]. If the dipole moment is supercritical ($D > D_\mathrm{crit}$), the lowest eigenvalue d becomes a complex number [12]

$$d = -\frac{1}{2} + i\xi, \tag{1.58}$$

[3]The resonance width and level shift are energy-independent functions in the original Breit-Wigner formula.

where ξ is real. The resonance width oscillates with increasing frequency as $\epsilon \to 0$ [13]

$$\Gamma \propto \frac{1}{1 + \mathrm{e}^{2\pi\xi} + 2\mathrm{e}^{\pi\xi}\cos(\xi \ln\epsilon + \gamma)}, \tag{1.59}$$

where γ depends on the dipole moment and short-range interaction. The width function vanishes as $\epsilon \to \infty$ and $R \to \infty$ in all above mentioned cases.

1.6 Local approximation

The effective energy-depended nonlocal potential is given by (we suppress the index J)

$$W_E(R, R') = V_\mathrm{d}(R)\delta(R - R') + F(E, R, R'), \tag{1.60}$$

with

$$F(E, R, R') = \Delta(E, R, R') - \frac{i}{2}\Gamma(E, R, R'). \tag{1.61}$$

The energy-independent local approximation also known as local complex potential (LCP) [3] is defined by

$$W_\mathrm{loc}(R) = V_\mathrm{loc}(R) - \frac{i}{2}\Gamma_\mathrm{loc}(R), \tag{1.62}$$

where

$$V_\mathrm{loc}(R) = V_0(R) + E_\mathrm{res}(R), \tag{1.63}$$

$$\Gamma_\mathrm{loc}(R) = \Gamma(E_\mathrm{res}(R), R, R), \tag{1.64}$$

$$E_\mathrm{res}(R) = V_\mathrm{d}(R) - V_0(R) + \Delta(E_\mathrm{res}(R), R, R). \tag{1.65}$$

1.7 Rate constant

Rate constant (or rate coefficient) k characterizes the rate of a chemical reaction. It is defined by the mean value of the product of the relative velocity v and the temperature-averaged cross section $\sigma(v, T)$ of the reaction. In the thermalized gas, the mean value is calculated assuming the Maxwell-Boltzmann distribution $\rho(v, T)$ of velocities

$$\rho(v, T) = \left(\frac{\mu}{2\pi k_\mathrm{B} T}\right)^{3/2} 4\pi v^2 e^{-\frac{\mu v^2}{2k_\mathrm{B}T}}, \tag{1.66}$$

where k_B is the Boltzmann constant. So, the rate constant is equal to

$$k(T) = \int_0^\infty v\sigma(v, T)\rho(v, T)\mathrm{d}v. \tag{1.67}$$

The interpretation of the rate constant is that it expresses the volume of the gas which disappears per unit of time owing to the ongoing reactions.

Particularly, the temperature-dependent rate constant of an associative detachment process is given by (expressed in terms of energy)

$$k(T) = \frac{8\pi}{\mu^2}\left(\frac{\mu}{2\pi k_{\mathrm{B}}T}\right)^{3/2}\int_0^\infty E\sigma_{\mathrm{AD}}(E)e^{-E/k_{\mathrm{B}}T}\mathrm{d}E, \tag{1.68}$$

where $\sigma_{\mathrm{AD}}(E)$ is the total AD cross section and T is the temperature of the thermalized mixture of atoms and ions.

2. Nonlocal resonant models of Li and H processes

2.1 Introduction

We introduce the description of low-energy collisions within the nonlocal resonant theory in the first chapter. In this and the following chapters, we apply the theory to the calculation of cross sections of two associative detachment processes

$$\mathrm{Li} + \mathrm{H}^- \rightarrow \mathrm{LiH} + \mathrm{e}^- \tag{2.1}$$

and

$$\mathrm{Li}^- + \mathrm{H} \rightarrow \mathrm{LiH} + \mathrm{e}^-. \tag{2.2}$$

These two processes together with radiative association were the source of lithium hydride molecule (LiH) in the early Universe [1, 2]. To our knowledge there is neither experimental nor theoretical information on rate constants or cross sections for these AD processes. The only independent information is the estimate of the rate constants for cosmological simulations made by Stancil et al. [14]. The comparison of the mentioned estimate with our results is discussed in Chapters 4 and 5.

The second chapter is devoted to the construction of the nonlocal resonant models from *ab initio* data for both processes of interest (2.2) and (2.1).

2.2 Potential energy curves

2.2.1 Computation methods

For the description of the studied collisions, we need potential energy curves of the ground electronic state of the neutral molecule LiH ($X^1\Sigma^+$),[1] the ground ($X^2\Sigma^+$) and first excited ($A^2\Sigma^+$) electronic states of the molecular anion LiH^-. From the relative positions of the curves and electron affinities, we can determine that the ground state of LiH^- asymptotically goes to $\mathrm{Li}+\mathrm{H}^-$ as $R \rightarrow \infty$, while the first excited anion state goes to $\mathrm{Li}^-+\mathrm{H}$. Therefore, $X^2\Sigma^+$ potential plays a role in the $\mathrm{Li}+\mathrm{H}^-$ collision, and the $A^2\Sigma^+$ state is needed in the description of the $\mathrm{Li}^-+\mathrm{H}$ channel. The ground state of LiH, of course, goes to the Li+H asymptote.

The fixed-nuclei potential curves for both the neutral molecule and molecular anion provided by K. Houfek (personal communication, January 15, 2016) were

[1] The spectroscopic notation of molecular states: X means the ground electronic state, A stands for the first excited electronic state, Σ denotes zero projection of electron orbital angular momentum to the molecular axis, the left superscript determines the spin multiplicity of the electron wave function. The molecule LiH has four electrons, that is an even number of electrons, and therefore, it is a singlet state. The anion LiH^- has one additional electron, hence a doublet state. The plus sign denotes that there is the reflection symmetry with respect to a plain containing nuclei. More information can be found, for example, in the book which deals with atomic and molecular spectra written by Bernath [15].

calculated similarly as results of Gadéa and Leininger [16] by the quantum chemistry codes MOLPRO developed by Werner et al. [17]. Specifically, the multiconfigurational self-consistent field method (MCSCF) [18] and the multireference configuration interaction method (MRCI) [19] were used with the aug-cc-pVQZ basis of Gaussian orbitals developed by Dunning [20]. The complete active space in MCSCF consisted of ten active orbitals[2] with four or five active electrons.[3]

In fact, the determination of the anion potentials occurred in two steps. First, only the ground state was calculated. After that, both the ground and first excited states were computed. The first result for the ground state is more precise than the second result because two states are optimized in the second case. Used quantum chemistry methods are variational, that is the potential of the same system which has lower energy is better. The difference in the energy of the ground state between these two approaches is 41.1 meV at the largest computed internuclear distance[4] $R = 40$. This energy difference is not constant at various internuclear distances. For example, the difference is 42.2 meV at $R = 24$, 44.1 meV at $R = 15$, 42.0 meV at $R = 10.5$, and 33.7 meV at $R = 6.1$. To get more precise potential of the $A^2\Sigma^+$ state, we decided to shift all calculated data for this state by the value at the largest computed R, that is by 41.1 meV.

The shift was the only intervention to the quantum chemistry data that we made. In the description of the studied processes, we want to avoid similar interventions as much as possible because we use the so-called *ab initio* approach.[5] In this kind of approach, potential data or other data are determined from some theoretical model describing interactions in the physical system of interest, where we specify the studied system at the beginning of calculations. We try to avoid any additional empirical tuning of the computed data. Specifically to our scattering problem, we determine the number and type of the nuclei (Li and H), the number of the electrons (four or five) and nuclear configurations (internuclear distance) at the beginning of MOLPRO calculations.

2.2.2 Interpolation and extrapolation

The potential curves were calculated at internuclear distances from $R = 1.5$ to 40. We did not find an accurate fit with a simple function, and thus, we decided to interpolate the data using cubic splines within the computed interval and extrapolate at large and small internuclear distances, see Figure 2.1. The quantum chemistry data are highlighted (full and empty circles). The neutral potential (red) and the ground anion potential (green) come close to each other at small internuclear distances but they never cross. The neutral potential and the excited anion potential (blue) cross each other at the internuclear distance $R_c = 6.7$. The neutral potential represents the continuum threshold.

Quantum chemistry methods are designed to calculate potential energy of bound states of a given system. There exists no excited bound state of the LiH^- system in the region $R < R_c$. The result of the quantum chemistry calculation

[2]The symmetry group of heterogeneous diatomic molecules, which is in fact $C_{\infty v}$, is represented by the point group C_{2v} in MOLPRO. This group has four irreducible representations A_1, B_1, B_2, A_2. The number of active orbitals in each representation was 6,2,2,0.

[3]The systems are small enough to take all electrons active. There are no frozen core electrons.

[4]We remind that we use atomic units if it is not stated otherwise.

[5]It means 'from first principles of quantum mechanics'.

represents the neutral molecule LiH with the free electron far from the molecule. Therefore, the excited anion potential ($A^2\Sigma^+$ state) can not be obtain for these nuclear configurations and the corresponding data (empty circles in Figure 2.1) converge to the neutral potential. The convergence is limited by the finite basis of Gaussian orbitals, which does not allow the electron to move sufficiently away from the molecule, which explains the difference between positions of the empty circles and the data belonging to the $X^1\Sigma^+$ state (red curve). The collapse of the wave function to the state of the neutral molecule with the electron far away is delayed because the self-consistency procedure may capture a false stationary point. The current calculation was performed from outside (in the direction from larger to smaller internuclear separations). This choice delays the collapse, that is the change of the shape of the potential curve does not occur immediately at the crossing point but at the point about $R = 5$.

As described above, the potential of the $A^2\Sigma^+$ state can not be obtained at nuclear configurations with $R < R_c = 6.7$. In fact, quantum chemistry provides the so-called adiabatic potentials, which do not exist in the electronic continuum. The proper generalization is the use of diabatic potentials, that is the discrete-state potentials $V_d(R)$. Data of electron scattering from the molecule LiH are needed to their construction, which we discuss later. The full circles in Figure 2.1 denote the data which were considered in the further use.

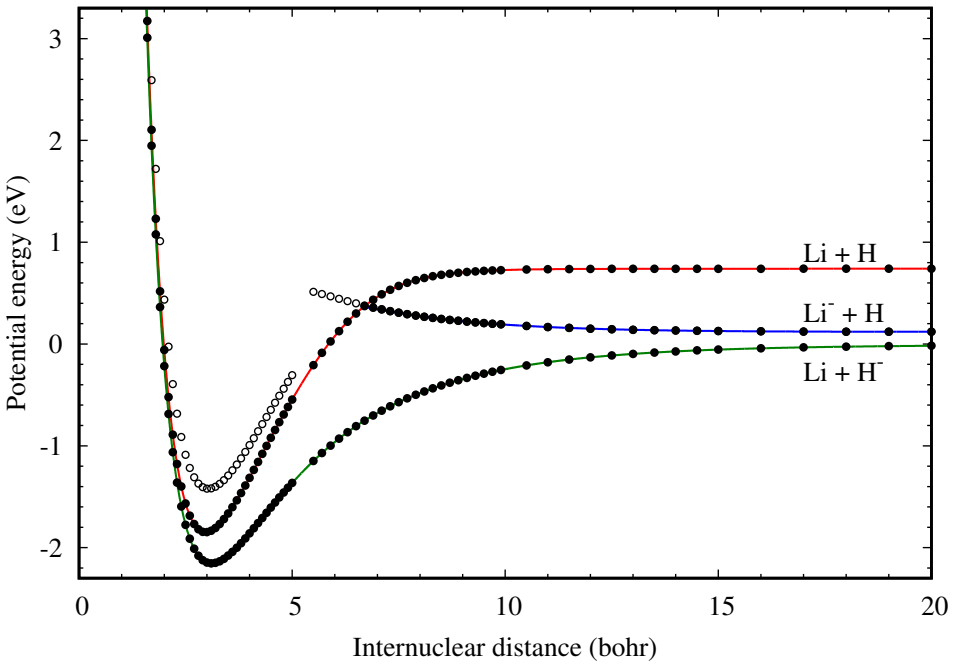

Figure 2.1: The fixed-nuclei potential energy curves of the ground electronic state of LiH (neutral potential, red curve), the ground (green) and first excited (blue) electronic states of LiH^-. Full and empty circles denote the quantum chemistry data. The data represented by the full circles were considered further. The empty circles represent the collapse of the anion wave function due to the representation of autoionizing states in the finite basis used in the electronic structure calculation. These data are not used in further calculations.

The extrapolation at large internuclear distances is given by the polarization potential in the case of anion

$$V_{\text{ion}}(R) \xrightarrow{R\to\infty} -\frac{\alpha}{2R^4}, \tag{2.3}$$

where α is the polarizability of the atom in the A+B$^-$ collision, α_{Li}=164.1 for the Li+H$^-$ collision [21] and α_{H}=4.5 for the Li$^-$+H collision.

The neutral potential behaves like the dispersion (van der Waals) potential at large R

$$V_0(R) \xrightarrow{R\to\infty} -\frac{C}{R^6}, \tag{2.4}$$

where the constant $C = 80$ was obtained by the least-squares fitting in the region from $R = 33$ to 40 (8 data points).

We use the Morse potential as the extrapolation function of the ground potentials at small internuclear distances

$$D\left(e^{-A(R-B)} - 1\right)^2 + F. \tag{2.5}$$

The values of parameters were again determined by the best least-squares fit. We used six data points from the interval of internuclear distances $[1.5, 2]$ in both of the cases. We obtained the following results. For the neutral potential, we have $D = 0.0263$, $A = 0.832$, $B = 3.168$, and $F = -0.100356$. In the case of the ground anion potential, the constants are given by $D = 0.0224$, $A = 0.828$, $B = 3.256$, and $F = -0.082909$. The constants F give correct extrapolations when the corresponding potential vanishes as $R \to \infty$. The mutual vertical positions of the potentials are fixed by electron affinities, which are discussed in the next section.

As we describe above, the extrapolation of the excited anion potential in the region $R < R_{\text{c}} = 6.7$ can not be done without scattering data, which we discuss later.

2.2.3 Electron affinities

We determined the electron affinities of lithium and hydrogen atoms from the extrapolation functions as the difference of the neutral potential and appropriate anion potential at $R \to \infty$ (Table 2.1). The comparison with the experimental values is also included in the table. Furthermore, the electron affinity of the molecule LiH was calculated as the difference of energies of the ground vibrational states of LiH and LiH$^-$. These energies were computed by Fourier DVR method, which we briefly discuss at the end of the next chapter in Section 3.7. Our result of electron affinity of Li corresponds with experiment very well. This agreement could not be attained without the shift of the excited anion potential data by 41.1 meV, which we describe at the end of Section 2.2.1. The errors of H and LiH affinities are in the order of tens of meV, which is the typical error of this kind of quantum chemistry calculations.

Authors of some other studies intentionally shift the potentials to agree with experimental electron affinities. We do not shift the potentials because the magnitude of errors is reasonable and the adjustment of the parameters to experimental data is against the idea of *ab initio* calculations discussed in Section 2.2.1.

Table 2.1: The comparison of the electron affinities of Li, H and LiH obtained from the quantum chemistry data with experimental values in eV.

	this work	experiment[a]
EA(Li)	0.620	0.618
EA(H)	0.740	0.754
EA(LiH)	0.320	0.342

[a] The experimental results were measured by Rienstra-Kiracofe et al. [22].

2.3 Dipole moment of LiH

The electric dipole moment of the molecule LiH was obtained within the electronic structure calculation using the same level of approximation as for the potential energy curves. Lithium hydride molecule possesses a permanent supercritical dipole moment (Figure 2.2).

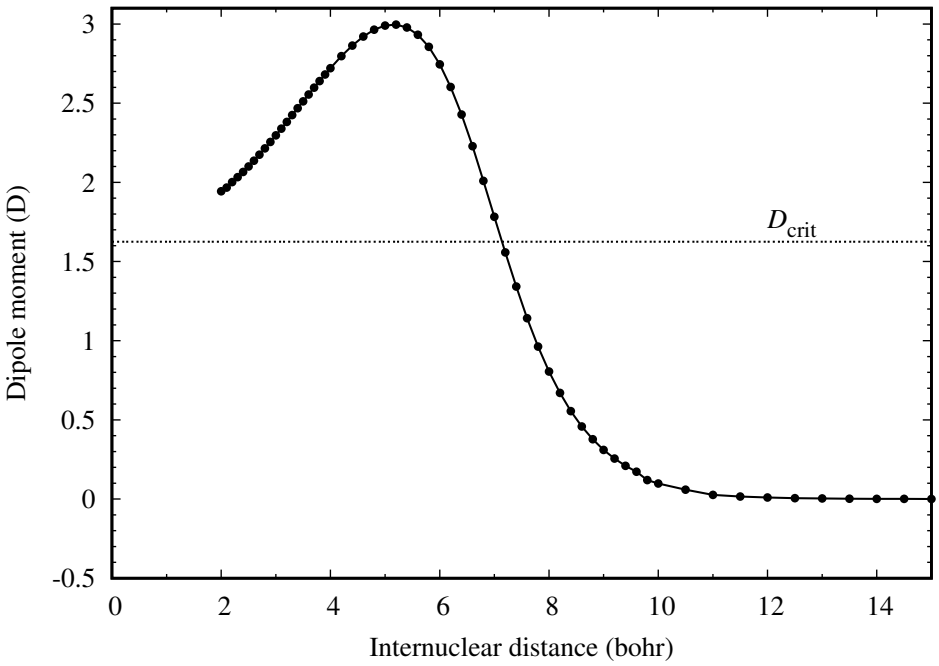

Figure 2.2: The electric dipole moment of the molecule LiH. Cicles represent the quantum chemistry data. The molecule posseses a supercritical dipole moment. The dashed line denotes the value of the critical dipole moment.

2.4 Scattering data

The fixed-nuclei eigenphase sum of the scattered electron from the molecule LiH was computed by K. Houfek (personal communication, July 19, 2016) using the R-matrix method [23] as implemented in the UK molecular R-matrix suite of codes [24, 25]. The target molecule (LiH) was described within the UK R-matrix suite

of codes using the multi-configurational self-consistent field method (MCSCF), particularly the complete active space self-consistent field method (CASSCF) with 4 electrons in 8 active molecular orbitals was used. The target was described by the cc-pVTZ basis of Gaussian orbitals [20], but the two most diffuse s and the two most diffuse p Gaussian basis functions were changed to be less diffuse to avoid problems with the linear dependence of the target basis and continuum basis used in scattering calculations. As a model for scattering, the close-coupling model [20] with only 1 target state and 10 virtual orbitals was used, which proved to be sufficient, because it reproduced closely the anion potential energy curves obtained from the MOLPRO calculations. The scattered electron was allowed in the complete active space and 10 virtual orbitals of the target.

The energy-dependent eigenphase sum was computed at 14 internuclear distances (Figure 2.3). The results logarithmically diverge at zero energy, which corresponds to the supercritical dipole moment of LiH [26] and the infinite number of bound states in e^-+LiH collision complex according to Levinson's Theorem. Resonances, which are visible in the eigenphase sum, determine the position of the excited anion potential at small internuclear distances ($R < R_c = 6.7$). There are no resonances belonging to the ground anion state, because this state is not embedded in the continuum at any internuclear distance (the anion potential is bound at all R, see again Figure (2.1)). Nevertheless, we suspect a strong non-adiabatic coupling between the ground anion state and the electron scattering continuum owing to the close proximity of the anion state to the continuum threshold represented by the neutral potential. The nonlocal theory is capable of the correct description of this situation.

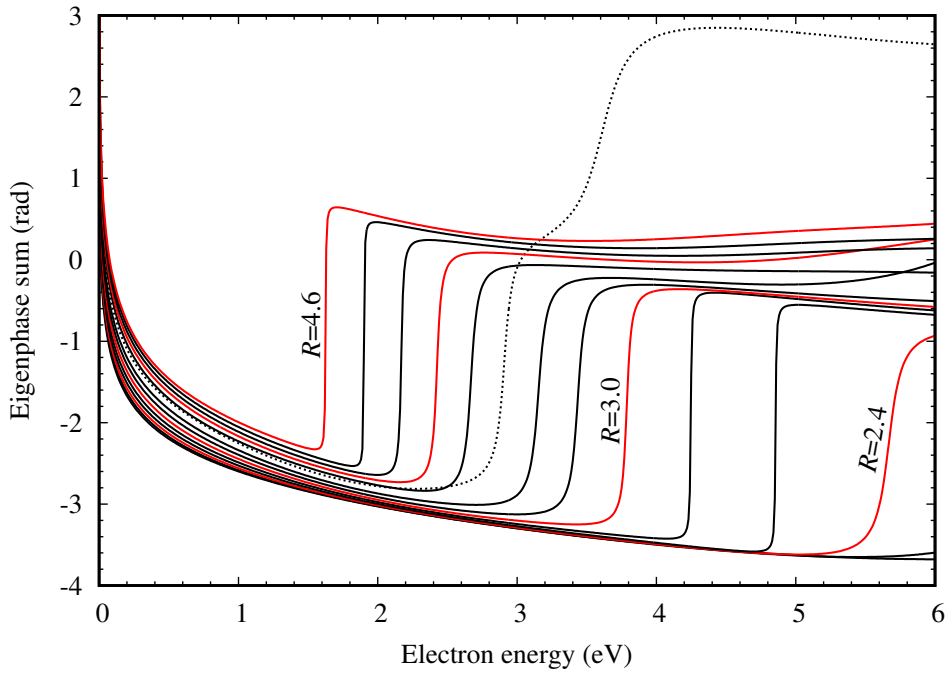

Figure 2.3: The fixed-nuclei eigenphase sum obtained from R-matrix calculations of electron-molecule scattering at 14 internuclear distances ($R = 2.0, \ldots, 4.6$ with step 0.2 from right to left).

Two resonances appear in the eigenphase sum with $R = 3.6$, the dotted curve in Figure 2.3, but there should be only one state embedded in the continuum, the state which has the Li^-+H asymptote as $R \to \infty$. We do not have any explanation for this behaviour. It might have a relation to the numerical problems with linear dependencies. There is even more serious problem. It was not possible to obtain reliable data in the vicinity of the crossing of the ground and excited anion potentials because of the mentioned numerical problems. The largest internuclear distance at which it managed to compute the data is $R = 4.6$, which is quite far from the crossing point $R_c = 6.7$. This region is significant for calculating quantitatively correct cross sections of the Li^-+H collision. We construct the nonlocal model without the data in the vicinity of the crossing and we also omit the curve with two resonances in the further investigation. The constructed model provides some extrapolation to the vicinity of the crossing. We test the sensitivity of results to the uncertainty in the extrapolation by constructing several models in Section 5.5.

2.5 Construction of NRMs

In theory, the nonlocal resonant model which describes both studied AD processes (2.1) and (2.2) can be constructed. The extension of the nonlocal theory for two and more discrete states is straightforward [27]. We decided to describe both the collisions independently. The regions which are important for the nonlocal dynamics are separated in both energy and internuclear distance.

The positions of resonances in the eigenphase sum are significant for the Li^-+H collision because they determine, as we mention earlier, the position of the excited anion potential at $R < R_c$. In terms of internuclear distances, the most important area for the nonlocal dynamics is the vicinity of the crossing of the $X^1\Sigma^+$ and $A^2\Sigma^+$ potentials at $R_c = 6.7$.

The ground anion potential is not embedded in the electronic continuum, but non-adiabatic effects can still play an important role in the region where the anion and neutral potentials approach ($R \leq 2.5$). Information about the $Li+H^-$ channel should be encoded in the low-energy behaviour of the eigenphase sum.

We found out that the dipole moment of LiH is supercritical. To our knowledge, the nonlocal dynamics with a supercritical dipole moment have been carried out only for hydrogen fluoride (HF) molecule by Čížek et al. [13]. The precise behaviour of the resonance width given by Formula (1.59) is significant only in the immediate vicinity of the threshold, and the best achievable resolution of nowadays experiments is about 10 meV. Therefore, it was sufficient to obtain the nonlocal model by fitting the energy-dependent level shift and resonance width by smooth functions, that is the oscillating behaviour was omitted. The detailed information can be found in the cited paper or in the overview of electron scattering by polar molecules by Fabrikant [12] and in references therein.

The full inclusion of a supercritical dipole moment into the nonlocal dynamics is beyond the scope of this master thesis. Thus, we decided to follow the similar approach as in the case of the HF molecule.

The nonlocal model is given by three functions $V_0(R)$, $V_d(R)$, and $V_{d\epsilon}(R)$, see Section 1.5. The neutral potential $V_0(R)$ is determined directly from the quantum chemistry calculations. The discrete-state potential $V_d(R)$ and the coupling

potential $V_{\mathrm{d}\epsilon}(R)$ can be obtained from fitting the eigenphase sum by generalized Breit-Wigner formula 1.54 and the appropriate background term. When determining $V_{\mathrm{d}}(R)$, the anion potentials (local potentials) are used as well. The reduced mass of the LiH molecule is equal to $\mu = 1605.5871$ [28].

The choice of the background term is to a certain extent arbitrary. The background eigenphase sum is assumed to be a smooth and slowly varying function of energy and space variables. On the other hand, all rapid changes should be included in the resonant term.

We parametrize the width function by

$$\Gamma(\epsilon, R) = a(R) \left(\frac{\epsilon}{b(R)} \right)^{\alpha(R)} \mathrm{e}^{-\epsilon/b(R)}. \tag{2.6}$$

The resonant part of the eigenphase sum given by Breit-Wigner formula (1.54) is then parametrized only by functions $a(R)$, $b(R)$, $\alpha(R)$, and the potential $V_{\mathrm{d}}(R)$, because the level-shift function $\Delta(\epsilon, R)$ is computed from the resonance width $\Gamma(\epsilon, R)$ according to Formula (1.48) at $R' = R$, and the neutral potential is known from quantum chemistry. The parameters need to be determined from the fit of the eigenphase sum.[6]

Now, we outline the fitting procedure of the R-dependent parameters $a(R)$, $b(R)$, $\alpha(R)$, $V_{\mathrm{d}}(R)$, and parameters of the background. The particular choices of the background terms as well as the obtained results from this procedure are discussed for both the studied processes in two following sections. We proceed similarly as Čížek et al. [29].

The *ab initio* eigenphase data were first fitted by means of the least squares by the sum of the resonant and background terms for each of 13 internuclear distances separately. So, we obtained 13 data points for each parameter. The next step is to approximate these data by suitable functions. This task was not easy to perform because no clear trend was often observable in the data, which was partly caused by a quite large number of the parameters. Not all parameters are independent of each other. The inclusion of the threshold exponent $\alpha(R)$ into the fitting procedure caused both an increase in the total number of parameters but also the occurrence of correlations among the parameters describing the resonance width in Formula (2.6). In addition, we did not always have the good first guess of the parameters to start the non-linear fit. Thus, reasonable fits were determined by several trial and error steps, which included fixed-R fitting and enforcing smoothness of R-dependencies of the parameters. Despite all efforts, the agreement of the eigenphase sum obtained from the fitted models with the *ab initio* data is not ideal. Furthermore, we did not use the information about the dipole moment of LiH in this procedure at all. Next, we discuss the details of the resulting fits for both of the states in following two sections.

2.6 NRM of the Li+H$^-$ collision

To obtain the nonlocal model of Li+H$^-$ collision (2.1), we need to fit the eigenphase sum in the low-energy region (up to energy about 1.4 eV), but not in the

[6] In the case of polar molecules with a subcritical dipole moment, the threshold exponent $\alpha(R)$ is fully determined from the dipole moment. Here, we include the determination of the threshold exponent to the fitting procedure.

immediate vicinity of the threshold.

We chose a linear function in both energy and internuclear distance as the background term with coefficients $a_{\rm bg}$, $b_{\rm bg}$, and $c_{\rm bg}$

$$\delta_{\rm bg}(\epsilon, R) = a_{\rm bg}\epsilon + b_{\rm bg}R + c_{\rm bg}. \tag{2.7}$$

To fit the low-energy behaviour with Breit-Wigner formula (1.54) was quite difficult. To reduce the number of free parameters, we fixed the threshold exponent to be constant $\alpha(R) = 0.1$ at all internuclear distances. The local anion potential of the $X^2\Sigma^+$ state is well known from the electronic structure calculations, and thus, we determined the discrete-state potential as

$$V_{\rm d}(R) = V_{\rm loc}(R) - \Delta(V_{\rm loc}(R) - V_0(R), R), \tag{2.8}$$

where $V_{\rm loc}(R)$ denotes a local potential, in this case the potential of the ground state of LiH^- ($X^2\Sigma^+$ state).

Values of the parameters were obtained by the fitting procedure described in the previous section. The background parameters are given by

$$a_{\rm bg} = -15.14, \tag{2.9}$$

$$b_{\rm bg} = 0.275, \tag{2.10}$$

$$c_{\rm bg} = -2.612, \tag{2.11}$$

and the R-dependent functions in the resonance width given by Formula (2.6) have the forms

$$\alpha(R) = 0.1, \tag{2.12}$$

$$a(R) = 3.0{\rm e}^{-0.025R^2}, \tag{2.13}$$

$$b(R) = 0.00114R + 0.00088. \tag{2.14}$$

We compared the resulting eigenphase sum with the *ab initio* data at 13 values of internuclear distance, see Figure 2.4. The model eigenphase sum represented by red curves is finite at zero energy instead of the logarithmic divergence of the *ab initio* data (circles). We expect that this flaw in the model influences the final cross sections only on about 10 meV vicinity of the thresholds, and it do not influence the integral cross section and rate constant significantly.

Unexpected resonances appear at larger energies in the eigenphase sum obtained from the nonlocal model. Their physical origin and meaning is unknown to us. We emphasise that the use of the nonlocal theory is not typical in the case of the $Li+H^-$ collision. In the usual situation, an anion state is bound for some nuclear configurations and it disappears in the continuum as a shape resonance for other configurations. Here, the anion state is bound at all internuclear distances.

We at least explain the origin of the odd resonances from the mathematical point of view. Before we get to it, we show the relevant potentials in the description of the Li+H$^-$ collision (Figure 2.5). The separation of the discrete-state potential (black curve) from the local anion potential (green) occurs at a fairly large internuclear distance ($R \approx 15$). Typically, a discrete-state potential first distinctly differs from a local potential in the vicinity of the crossing point.

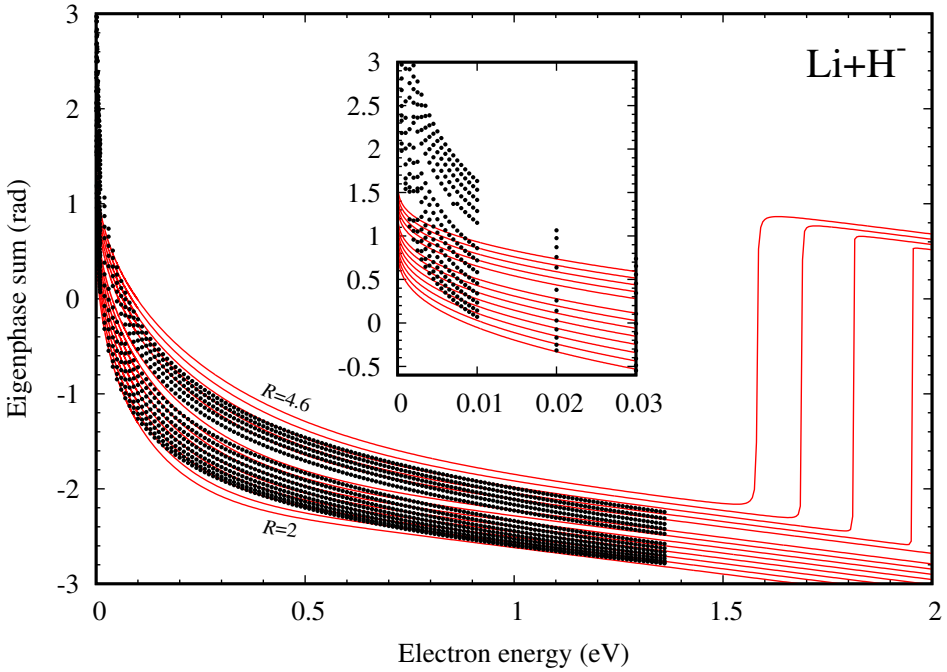

Figure 2.4: The comparison of the eigenphase sum from the *ab initio* calculations (circles) with the results from the constructed nonlocal model (red curves) at 13 internuclear distances ($R = 2.0$ to 4.6 with step 0.2 from bottom to top, $R = 3.6$ is omitted). The inset shows the immediate vicinity of the threshold, where the scattering data logarithmically diverge. The model eigenphase sum is finite at the threshold. The unexptected resonances appear at energies above 1.5 eV.

Now, we describe the origin of the resonances. If the argument of $\tan^{-1}$ in Breit-Wigner formula (1.54) changes the sign, a resonance appears in the eigenphase sum. The resonance here means the change of the value by π. To ensure the continuity of the eigenphase sum, we subtract π from $\tan^{-1}$ if the argument is positive. The width of a resonance is given by $\Gamma(\epsilon, R)/2$ and its position is $V_\mathrm{d}(R) - V_0(R) + \Delta(\epsilon, R)$. The width function $\Gamma(\epsilon, R)$ is always positive, therefore, the resonance appears at energy which is the root of the denominator of the argument at some fixed internuclear distance. The denominator as a function of energy (at fixed R) has two roots independently of R (Figure 2.6). The left-hand root describes the shape of the eigenphase sum in the low-energy region. The other is responsible for the odd resonances at higher energies. At low energies, the behaviour of the denominator is mostly given by $\Delta(\epsilon, R)$. The shape of $\Delta(\epsilon, R)$ at $R = 4.6$ is shown as the blue dashed curve in the latter figure. The term $-V_\mathrm{d}(R) + V_0(R)$ at some fixed R just cause a small vertical shift. The term ϵ is substantial at large energies, where $\Delta(\epsilon, R)$ exponentially decays, and

it is responsible for the occurrence of the second root.

The problem with the resonances may be fundamental in situations similar to the Li+H$^-$ case with the used parametrization of the width function. We need a gradual decline in the eigenphase sum by π, which is achieved by the change of the denominator from positive values to negative. But then, the second root always exists due to the ϵ term and the fact that $\Delta(\epsilon, R)$ vanishes. Thus, the increase by π appears in the eigenphase sum since the change is from negative values to positive.

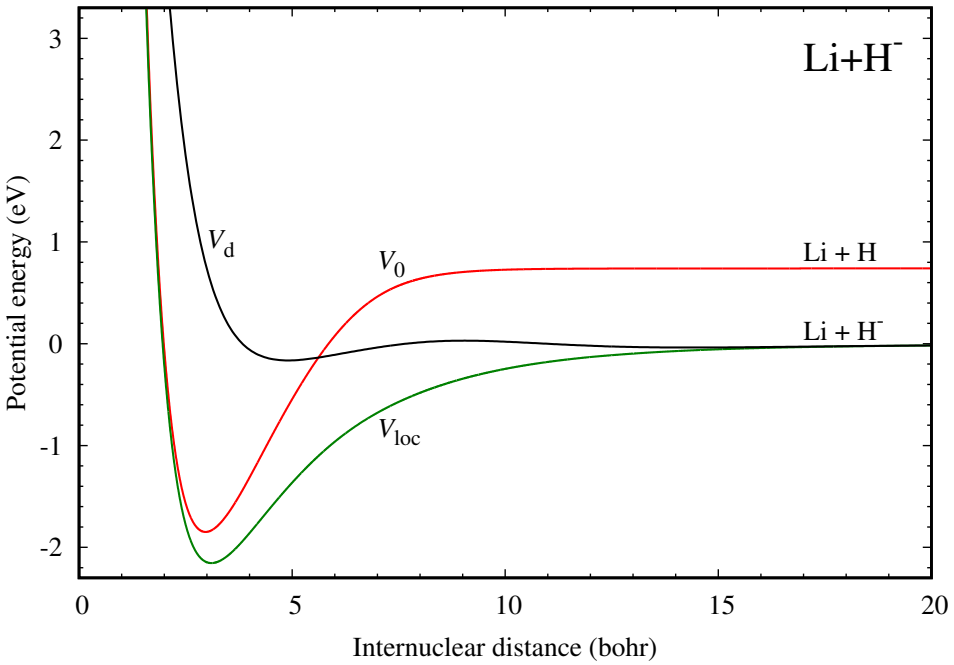

Figure 2.5: The discrete-state potential V_d for the Li+H$^-$ collision together with the neutral potential V_0 of the molecule LiH and the ground potential V_loc of the molecular anion LiH$^-$.

In addition, we found out that the positions of the resonances are sensitive to the magnitude of the parameter $a(R)$ given by Formula (2.13). When we increase the magnitude, the positions move towards higher energies. This parameter changes the overall magnitude of the width and the level-shift functions.[7] Therefore, the local minimum of the denominator is lower with greater $a(R)$, which results in the shift of the second root. The influence of the change of $a(R)$ on the shape of the eigenphase sum is negligible in the low-energy region, because the positions of the respective roots change only slightly. The discrete-state potential is interconnected with the level-shift function by Equation (2.8). The difference $V_\mathrm{loc}(R) - V_0(R)$ is negative since the anion state is bound, $\Delta(\epsilon, R)$ is also negative at $\epsilon < 0$. Therefore, the potential is vertically shifted upwards when the magnitude of $a(R)$ is increased.

We chose the particular magnitude of $a(R)$ (2.13) so that the resonances did not appear in the energy region where we fitted the *ab initio* data, that is up to energy about 1.4 eV. We did not move the resonances to very high energies

[7]The shift function is obtained from the resonance width using Formula (1.48) evaluated at $R' = R$.

because the discrete-state potential would separate from the local potential at even larger internuclear distances, see again Figure 2.5. We discuss different choices of $a(R)$ and their influence on AD cross sections in Chapter 4.

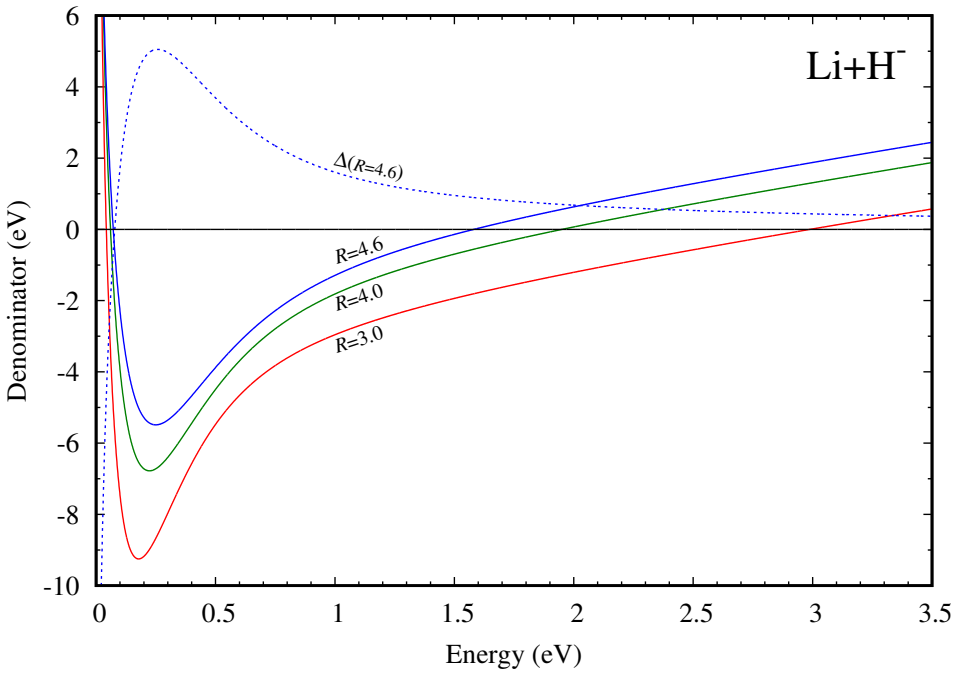

Figure 2.6: The energy dependence of the denominator $\epsilon - V_{\mathrm{d}}(R) + V_0(R) - \Delta(\epsilon, R)$ of the argument in Breit-Wigner formula (1.54) at three fixed values of the internuclear distance $R = 3.0, 4.0, 4.6$ (solid curves from bottom to top respectively). The dashed blue curve represents the energy dependence of $\Delta(\epsilon, R)$ at $R = 4.6$.

2.7 NRM of the Li^-+H collision

Unlike the previous case, the situation is fairly typical in Li^-+H channel (2.2). We fitted the eigenphase sum in the entire interval where the *ab initio* data were calculated. We put emphasis on the positions of resonances. The eigenphase sum logarithmically diverges as $\epsilon \to 0$. Thus, we chose the logarithmic dependence in energy as the background term[8]

$$\delta_{\mathrm{bg}}(\epsilon, R) = a_{\mathrm{bg}}(R)\log(\epsilon) + b_{\mathrm{bg}}(R) \tag{2.15}$$

with coefficients $a_{\mathrm{bg}}(R)$, $b_{\mathrm{bg}}(R)$ depending in general on the internuclear distance.

We determined the parameters of the background term and the width function given by Formula (2.6) by the fitting routine described in Section 2.5 as follows

$$a_{\mathrm{bg}}(R) = -0.0835R - 0.390, \tag{2.16}$$

$$b_{\mathrm{bg}}(R) = 0.0903(R - 2.973)^2 - 4.693, \tag{2.17}$$

[8]We can not choose the same background part in the previous model because the logarithm describes the low-energy behaviour very well and there would be nothing left to include into the resonant part.

$$a(R) = (6.093R^2 - 34.03R + 48.07)\mathrm{e}^{-1.224R}, \tag{2.18}$$

$$b(R) = 0.171\mathrm{e}^{-0.129R^2}, \tag{2.19}$$

$$\alpha(R) = 0.5 - \frac{0.0250}{1.0 - 0.722R + 0.137R^2}. \tag{2.20}$$

The parameter $a(R)$ possesses a local minimum, which is caused by two narrow resonances at $R = 2.6$ and 2.8, the surrounding resonances are wider, see again Figure 2.3.

The parameters above do not only serve as some interpolation of the data from the fitting procedure, but also as an extrapolation in the vicinity of the crossing, where no data are available from the reasons discussed in Section 2.4. Dipole moment vanishes at $R = 0$ and as $R \to \infty$. The threshold exponent equals $(2l+1)/2$ in that case (see Section 1.5). Thus, we chose the function $\alpha(R)$ so that it fulfils this behaviour with $l = 0$, which is the lowest l allowed by symmetry in the Li^-+H collision.

The discrete-state potential was determined from two sets of data (Figure 2.7). In the region $R < R_c = 6.7$, the position of the discrete-state potential is fixed by $\epsilon - V_d(R) + V_0(R) - \Delta(\epsilon, R) = 0$, which comes from Breit-Wigner formula (1.54) and determines the energies of the resonances in the eigenphase sum (scattering data in the figure). At $R > R_c$, the discrete-state represents the $A^2\Sigma^+$ state of the molecular anion LiH^-. Thus, we use the MOLPRO data in this region. The final fit of the discrete-state potential, which was determined by means of the least squares, reads

$$V_d(R) = 188.5e^{-3.233R} + 0.325\frac{1}{R}e^{-0.237R} - \frac{2.25}{\left[(R-10.79)^2 + 38.25\right]^2 + 3627}. \tag{2.21}$$

The quantum chemistry data ensure the proper physical behaviour of the latter potential as $R \to \infty$ (see Section 2.2.2).

The constructed nonlocal model does not follow the *ab initio* eigenphase sum precisely (Figure 2.8). The horizontal difference in the position of the resonance at $R = 4.6$ between the *ab initio* data (circles) and the result from the model (red curves) is 54 meV. As we mention earlier, the R-dependent parameters serve as extrapolation functions in the vicinity of the crossing at $R_c = 6.7$ since the largest internuclear distance, where the scattering data (eigenphase sum) are available, is $R = 4.6$. We test the sensitivity of the final cross sections to this extrapolation in Chapter 5.

We briefly return to the discussion about the denominator in Breit-Wigner formula (1.54) from the previous chapter. The qualitative behaviour of the denominator is the same as in Figure 2.6 except that the shape is horizontally shifted to the left. The denominator is finite and negative at the threshold and it possesses only one root at fixed R, which causes the resonances visible in Figure 2.8.

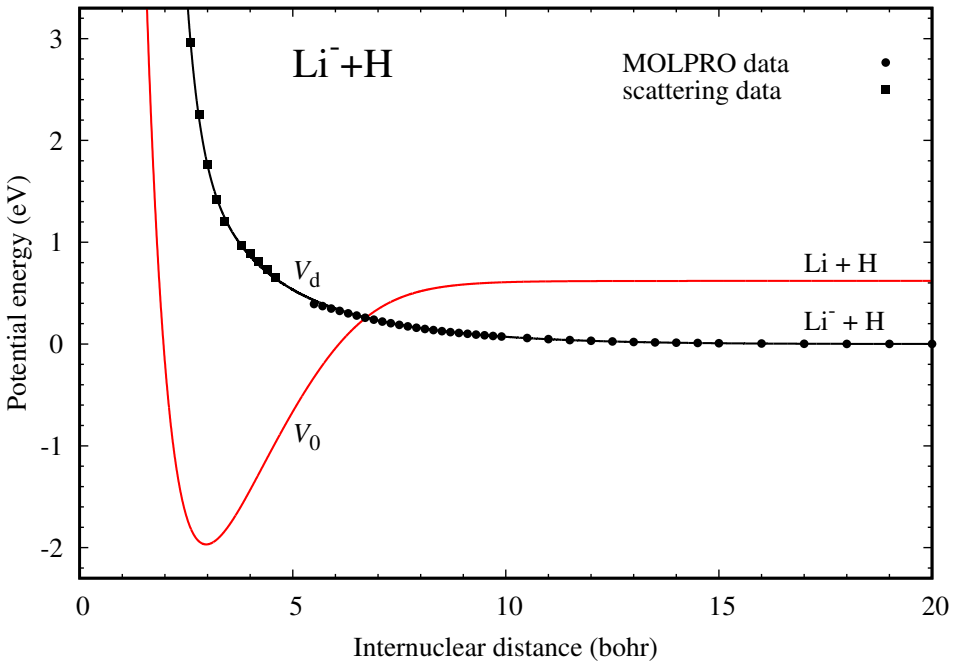

Figure 2.7: The discrete-state potential $V_{\rm d}$ of the $\rm Li^-$+H collision constucted by the fit of the *ab initio* scattering data (squares) and the quantum chemistry data of the $A^2\Sigma^+$ bound state of $\rm LiH^-$ (circles) together with the potential V_0 of the neutral molecule LiH.

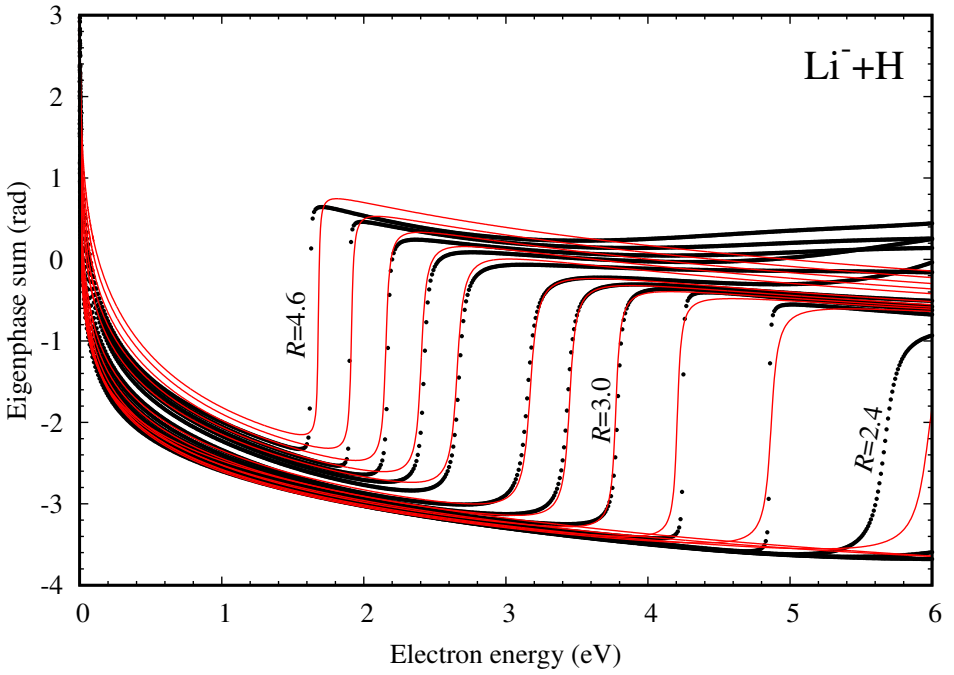

Figure 2.8: The comparison of the *ab initio* eigenphase sum (circles) and the eigenphase sum calculated from the constructed nonlocal model of the $\rm Li^-$+H collision (red curves) at 13 internuclear distances ($R = 2.0, \ldots, 4.6$ with step 0.2 from right to left, $R = 3.6$ is omitted).

3. Separation of the coupling potential

3.1 Introduction

In the third chapter, we discuss the separability and non-separability of the discrete-state-continuum-coupling potential, which greatly influences computational times of the cross section calculation. The coupling potentials constructed for both studied processes (2.1) and (2.2) are not separable in energy and space. We present a new method which approximates non-separable potentials by the sum of separable terms. We also test this method by calculation of the known AD cross sections of the Br^-+H collision. At the end of this chapter, we outline some numerical methods and details which are related to the studied scattering problems.

3.2 Separability of the coupling potential

We use the Schwinger-Lanczos algorithm proposed by Meyer et al. [30] to solve Lippman-Schwinger equation (1.44). The application of nonlocal potential (1.46) on a vector is needed in the algorithm. The potential F acts on a vector x as an integral operator because of the nonlocality. Thus, the resulting vector y is given by

$$y(R) = \int \mathrm{d}R' F(E, R, R') x(R'). \tag{3.1}$$

In fact, this is typically the most time-consuming step in cross section calculations. The use of the Schwinger-Lanczos algorithm is convenient because the nonlocal potential is applied only $2N_{\mathrm{iter}} + 1$ times, where N_{iter} is the number of Lanczos iterations (typically tens of iterations are needed).

If we use the nonlocal potential expressed by Formula (1.46) with a general coupling potential, we have to evaluate Hermitian part (1.48) for each R, R' and $E - E_{\nu J}$ in the calculation of $y(R)$ (3.1). Cauchy principal value integral (1.48) with the resonant width parametrized by Formula (2.6) can be computed analytically in terms of the incomplete gamma function and confluent hypergeometric function [4]. Nevertheless, the calculation of $y(R)$ would be very time-demanding.

The separability of the coupling potential $V_{\mathrm{d}\epsilon}$ is commonly assumed [31], that is the coupling potential equals the product of a function depending on energy and a function which only depends on the space variable

$$V_{\mathrm{d}\epsilon}(R) = f(\epsilon) g(R). \tag{3.2}$$

Assuming the separability, we have the nonlocal potential expressed as[1]

$$\begin{aligned} F(E, R, R') = \sum_{\nu} \chi_\nu(R) \Big[& g(R) \delta(E - E_\nu) g(R') \\ & - \frac{\mathrm{i}}{2} 2\pi g(R) f(E - E_\nu)^2 g(R') \Big] \chi_\nu(R'), \end{aligned} \tag{3.3}$$

[1] In this chapter we suppress the index J whenever it is possible without any confusion.

where the quantity δ depends only on energy and is given by

$$\delta(E - E_\nu) = \text{p.v.} \int \mathrm{d}\epsilon \frac{f(\epsilon)^2}{E - E_\nu - \epsilon}. \tag{3.4}$$

The latter two expressions are derived from Equations (1.46) to (1.48) and the assumption of separability. We also assume that f is a real function. The application of F is effective in this case. We just integrate the product $g(R')\chi_\nu(R')x(R')$ over R' for each ν, and we calculate δ term (3.4) only once for each energy $E - E_\nu$.

However, the constructed coupling potentials are not separable in energy and space because the width function given by Formula (2.6) is not separable. We approximate the non-separable coupling by the finite sum of separable terms

$$V_{\mathrm{d}\epsilon}(R) = \sum_k f_k(\epsilon) g_k(R). \tag{3.5}$$

In such case, the nonlocal potential is expressed by

$$\begin{aligned} F(E, R, R') = & \sum_\nu \chi_\nu(R) \sum_{k,k'} \Big[g_k(R) \delta_{kk'}(E - E_\nu) g_{k'}(R') \\ & - \frac{\mathrm{i}}{2} 2\pi g_k(R) f_k(E - E_\nu) f_{k'}(E - E_\nu) g_{k'}(R') \Big] \chi_\nu(R') \end{aligned} \tag{3.6}$$

with

$$\delta_{kk'}(E - E_\nu) = \text{p.v.} \int \mathrm{d}\epsilon \frac{f_k(\epsilon) f_{k'}(\epsilon)}{E - E_\nu - \epsilon}. \tag{3.7}$$

If the number of terms in expansion (3.5) is small, the calculation of $y(R)$ (3.1) is manageable.

We emphasise that the problem with $V_{\mathrm{d}\epsilon}(R)$ separation concerns only the Hermitian part of the nonlocal potential because of integral (1.48). This integral, a Hilbert transform, couples R and R' for a general form of the coupling potential. The anti-Hermitian part is always separated in R and R' owing to Formula (1.47), therefore we can integrate over R' without any constrains.

Separable expansion (3.5) can be obtained by the approximation proposed by Bateman [32], and used in nonlocal calculations, for example, by Houfek et al. [33] or Horáček et al. [34]. We introduce the new method of $V_{\mathrm{d}\epsilon}(R)$ separation in the next section.

3.3 Separation procedure

We assume that the coupling potential has the form

$$V_{\mathrm{d}\epsilon}(R) = \frac{1}{\sqrt{2\pi}} a(R)^{1/2} \left(\frac{\epsilon}{b(R)} \right)^{\alpha(R)/2} e^{-\epsilon/2b(R)}, \tag{3.8}$$

which comes from Equations (1.47) and (2.6). The basic idea of our proposed method is the evaluation of the potential on some energy and space grid (ϵ-grid and R-grid). The resulting matrix is then decomposed by the singular value decomposition method (SVD).

We briefly review the singular value decomposition. The more detailed description can be found, for example, in Numerical Recipes [35]. Let us assume that we have a real rectangular matrix A with dimensions $m \times n$. Then, A is decomposed by the SVD method to the product of three matrices

$$A = U\Sigma V^T. \tag{3.9}$$

The matrices U and V have dimensions $m\times n$ and $n\times n$ respectively. The columns of U are orthonormal, the same property holds for columns of V, the matrix Σ is diagonal and square $n \times n$. The numbers on the diagonal, the so-called singular values, are real positive and sorted in the descending order by their magnitude. In the quantum mechanics notation, we can rewrite decomposition (3.9) as

$$A = \sum_{k=1}^{n} \sigma_k |u_k\rangle\langle v_k|, \tag{3.10}$$

where u_k and v_k are the k-th columns of the matrices U and V respectively, σ_k is the k-th singular value. The last expression is in the desirable form, the sum of separable terms.

If we denote v_k by f_k and the product $\sigma_k u_k$ by g_k, we achieve the separable form of $V_{\mathrm{d}\epsilon}$ given by Formula (3.5). The only problem is that the functions f_k and g_k are not given by analytic formulas but they are evaluated on the chosen grids. In fact, the knowledge of g_k only in mesh points is convenient. When we choose the R-grid as the grid where the nonlocal dynamics is calculated, we can directly use g_k in the program code without any further interpolation or extrapolation. On the other hand, we need functions f_k in order to calculate integral (3.7). We refer to the functions f_k as the SVD energy functions. As mentioned earlier, there exists an analytic expression used by Domcke and Mündel [36] of the following integral

$$\mathrm{Del}(\epsilon, \alpha) = \mathrm{p.v.} \int \mathrm{d}x \frac{x^\alpha e^{-x}}{\epsilon - x}, \tag{3.11}$$

which we denote by $\mathrm{Del}(\epsilon, \alpha)$ for further use.

We empirically found out that the functions f_k are oscillating with the number of roots equal to $k - 1$, with the threshold behaviour ϵ^α at the origin, and with an exponential decay at large energies. Thus, we suggest to fit the functions f_k by

$$\tilde{f}_k(\epsilon) = \epsilon^{\alpha_k} p_k(\epsilon) e^{-b_k \epsilon}, \tag{3.12}$$

where $p_k(\epsilon)$ is a polynomial with degree N_k. With this assumption, we approximate energy-dependent Hermitian part (3.7) by

$$\delta_{kk'}(E - E_\nu) = \mathrm{p.v.} \int \mathrm{d}\epsilon \frac{f_k(\epsilon) f_{k'}(\epsilon)}{E - E_\nu - \epsilon} \simeq \mathrm{p.v.} \int \mathrm{d}\epsilon \frac{\tilde{f}_k(\epsilon) \tilde{f}_{k'}(\epsilon)}{E - E_\nu - \epsilon}. \tag{3.13}$$

The last integral can be calculated from the analytical expression of integral $\mathrm{Del}(\epsilon, \alpha)$ (3.11), since the product of $\tilde{f}_k$ and $\tilde{f}_{k'}$ has the same structure as function $\tilde{f}_k$ (3.12) itself with the polynomial $p_k(\epsilon)p_{k'}(\epsilon)$, parameters $\alpha_k + \alpha_{k'}$ and

$b_k + b_{k'}$. We denote the coefficients of the latter polynomial by $c_i^{(kk')}$, $i = 0, \ldots, N_k + N_{k'}$, where $N_k + N_{k'}$ is its degree. We substitute expression (3.12) for the functions $\tilde{f}_k(\epsilon)$ and $\tilde{f}_{k'}(\epsilon)$ into Formula (3.13). Then, we obtain the following formula by using a linear substitution and the integral linearity

$$\delta_{kk'}(\epsilon) = \frac{1}{(b_k + b_{k'})^{\alpha_k + \alpha_{k'}}} \sum_{i=0}^{N_k + N_{k'}} \frac{c_i^{(kk')}}{(b_k + b_{k'})^i} \mathrm{Del}\left[(b_k + b_{k'})\epsilon, i + \alpha_k + \alpha'_k\right]. \qquad (\pi)$$

3.4 Fitting of the SVD energy functions

Now, we deal with the fitting of the SVD energy functions f_k by Formula (3.12). One obvious possibility is to use a non-linear least-squares approach. This may be tricky because the number of parameters to find is[2] $N_k + 3$, and the degree N_k of the polynomial can be fairly large (over ten). In that case, the localization of the minimum in a multidimensional parameter space is difficult, especially, if we do not have the good first guess to start iterations of the fitting procedure.

We propose another fitting routine, which gives satisfying results. We make use of the fact that $N_k + 1$ of the total $N_k + 3$ parameters are linear. We manually fit the low-energy behaviour, that is we determine the parameter α_k in Formula (3.12). We fix this parameter in the further investigation. Then, we choose an interval in which we expect the parameter b_k lies and we fix b_k at the lowest value. When we fix both of the non-linear parameters, we can determine the remaining quantities by a linear fit using QR decomposition [35].

Again, we briefly review the QR decomposition method. A rectangular real matrix B can be decomposed into the product of two matrices[3] Q and R

$$B = QR, \qquad (3.15)$$

where Q is orthogonal with the same dimension as B, that is[4] $Q^T Q = I$, and R is upper triangular.

We rewrite the form of fitting function (3.12) into

$$\tilde{f}_k(\epsilon) = \sum_{n=0}^{N_k} c_n^{(k)} \phi_n(\epsilon), \qquad (3.16)$$

where $c_n^{(k)}$ are coefficients of the polynomial $p_k(\epsilon)$ and $\phi_n(\epsilon) = \epsilon^{\alpha_k} \epsilon^n e^{-b_k \epsilon}$. Next, we construct the matrix B. Its elements are given by

$$B_{ij} = \phi_j(\epsilon_i), \; i = 1, \ldots, N_\epsilon, \; j = 0, \ldots, N_k, \qquad (3.17)$$

where N_ϵ is the number of energy mesh points ($N_\epsilon \gg N_k$). We want to find such coefficients $c_n^{(k)}$ which best approximate the function f_k at mesh points

$$Bc^{(k)} \simeq f_k. \qquad (3.18)$$

[2]The polynomial has the degree N_k, which means it is defined by $N_k + 1$ parameters, and then, we have to add parameters α_k and b_k.

[3]In this section, R denotes a matrix and not internuclear distance.

[4]But $QQ^T \neq I$ because the matrix Q is rectangular.

In other words, the vector $c^{(k)}$ solves

$$Bc^{(k)} = P_{QR} f_k, \tag{3.19}$$

where the right-hand side $P_{QR} f_k$ is the orthogonal projection of the vector f_k to the range of the matrix B. We use the QR decomposition, and thus, we have $B = QR$. The projector P_{QR} can be then represented by $P_{QR} = QQ^T$. If we multiply both sides of Equation (3.19) by $Q^{-1}(= Q^T)$ from the left, we obtain

$$Rc^{(k)} = Q^T f_k. \tag{3.20}$$

Since the matrix R is upper triangular, the last equation is solved by the back substitution.

The parameter α_k is well determined by the manual fit, but b_k is not optimal so far. We repeat the procedure for many values of b_k in the chosen interval. We choose an equidistant grid on this interval and we calculate the vector $c^{(k)}$ for each point. After that, the best b_k is determined as the value which minimize the quantity

$$\sum_{i=1}^{N_\epsilon} \left(f_k(i) - \tilde{f}_k(\epsilon_i) \right)^2. \tag{3.21}$$

We briefly discuss the effectiveness of the described procedure. First of all, it is important to realize that the separation of the coupling potential does not depend on the partial wave J or collision energy E. Therefore, the separation and fitting of f_k are done only once for all J and all E at the beginning of cross section calculations. In addition, the computation of the linear fit is not very time-demanding since the number of parameters is low. We see further that maximal polynomial degree is about $N_k \approx 14$. The computational time is typically in the order of seconds when the calculation is performed on a regular PC.

We summarize the separation procedure. The coupling potential $V_{\mathrm{d}\epsilon}(R)$ is decomposed by the SVD method on chosen grids. The SVD expansion is cut at a certain point, only few terms are left. Each function $f_k(\epsilon)$ is fitted by Formula (3.12). The parameter α_k is determined from the manual low-energy fit and its value is fixed. The parameters $c^{(k)}$ and b_k are obtained from the cycle of linear fits. It is necessary to choose convenient values of the degree N_k of the polynomial $p_k(\epsilon)$ before the procedure starts.

3.5 Comparison with the Bateman approximation

We briefly compare the Bateman approximation with the developed method. The first Bateman approximation [32] of a function $V(x, y)$ reads

$$V_1(x, y) = \frac{V(x, y_1) V(x_1, y)}{V(x_1, y_1)}, \tag{3.22}$$

and the M-th approximation is given by

$$V_M(x, y) = V_{M-1}(x, y) + \frac{W_{M-1}(x, y_M) W_{M-1}(x_M, y)}{W_{M-1}(x_M, y_M)} \tag{3.23}$$

with

$$W_{M-1}(x,y) = V(x,y) - V_{M-1}(x,y). \tag{3.24}$$

Houfek et al. [33] proposed to choose the points (x_i, y_i), $i = 1, \ldots, M$ only on the diagonal $x = y$ as follows. The point (x_1, y_1) is the point where the maximum of $|V(x,y)|$ occurs, and analogously further, $|W_{i-1}(x,y)|$ have the maxima at the points (x_i, y_i).

The Bateman approximation was used by Houfek et al. [33] to separate the energetic term δ in the Hermitian part of the nonlocal potential in the R and R' variables

$$\Delta(E,R,R') = g(R)\delta(E,R,R')g(R'). \tag{3.25}$$

The symmetry $\Delta(E,R',R) = \Delta(E,R,R')$ is used by considering the points only on the diagonal $(x = y)$. On the other hand, we separate directly the coupling potential $V_{\mathrm{d}\epsilon}(R)$, which possesses no such symmetry. The good choice of the points (x_i, y_i) may be problematic in general case, that is without the symmetry.

The Bateman approximation has to be performed for each collision energy while the SVD separation is done once at the beginning of the calculation. However, our procedure is not fully automatic and it requires manual interventions, which may not be worth saving some computational time.

The advantage of the SVD method is the better control of the separation precision. The magnitude of contributions of individual terms in SVD expansion (3.10) is given by the singular values, because the columns u_k and v_k are normalized. In contrast to the convergence of the SVD expansion with respect to the L^2-norm, the M-th Bateman approximation minimizes the residue of $M-1$-th approximation ($W_{M-1}(x,y)$) with respect to the absolute value (maximum norm).

We conclude this discussion by saying that the comparison of both the methods on a particular example is desirable, but we will no longer deal with it in this thesis.

3.6 Test of the separation method

We illustrate the described separation method on the associative detachment process

$$\mathrm{Br}^- + \mathrm{H} \rightarrow \mathrm{HBr} + \mathrm{e}^-. \tag{3.26}$$

The cross sections of this collision, which were computed by the use of the Bateman approximation, are available to us. Here, we compare these results with the cross sections obtained with the coupling separated by the SVD method.

We present the nonlocal resonant model of process (3.26), which was constructed by Čížek et al. [29]. The reduced mass of the molecule HBr is 1813.0066 and the electron affinity of the bromine atom equals 3.373 eV.

The potential curve of the ground electronic state of HBr is given by the Morse potential

$$V_0(R) = 0.144\left(e^{-1.92(R-R_0)} - 2e^{-0.96(R-R_0)}\right), \tag{3.27}$$

where $R_0 = 2.67$ is the equilibrium distance.

The dipole moment of HBr is subcritical, and thus, the threshold exponent is given by the interpolation formula

$$\alpha(R) = \frac{1}{2} + a_1 M^2 + a_2 M^4 + a_3 M^6 + a_4 M^8 \tag{3.28}$$

with the following constants[5] $a_1 = -0.101157$, $a_2 = -1.4833 \times 10^{-2}$, $a_3 = 7.486 \times 10^{-3}$, and $a_4 = -3.735 \times 10^{-3}$, M is the R-dependent dipole moment of HBr, which is represented by the Padé approximation

$$M = M_0(1+x)^3 \left(1 + \sum_{i=1}^{7} e_i x^i\right)^{-1}, \tag{3.29}$$

where $x = (R - R_0)/R_0$, $M_0 = 0.81788$, $e_1 = 2.199$, $e_2 = 0.808$, $e_3 = 1.483$, $e_4 = 3.868$, $e_5 = -2.612$, $e_6 = 13.209$, and $e_7 = 0.255$.

The discrete-state potential is given by

$$V_{\mathrm{d}}(R) = 9.934 e^{-1.535R} - 2.25[(R - 1.437)^2 + 2.884]^{-2}. \tag{3.30}$$

The width function has the following form

$$\Gamma(\epsilon, R) = g(R)^2 \left[\beta(R)\epsilon\right]^{\alpha(R)} e^{-\beta(R)\epsilon} \tag{3.31}$$

with

$$g(R) = \begin{cases} 0.8688 - 0.1835R, & R < 4.7345 \\ 0, & R \geq 4.7345 \end{cases}, \tag{3.32}$$

$$\beta(R) = 4.865R - 4.788. \tag{3.33}$$

The background term of the eigenphase sum is equal to

$$\delta_{\mathrm{bg}}(\epsilon, R) = \frac{\pi}{2}\left(\frac{1}{2} - \alpha(R)\right) + a(R)\epsilon^{\alpha(R)} + b(R)\epsilon, \tag{3.34}$$

where

$$a(R) = 0.437R - 4.483, \tag{3.35}$$

$$b(R) = -2.0281. \tag{3.36}$$

Now, we have to evaluate the coupling potential, which can be obtained from width (3.31) by using Formula (1.47), on some energy and space grids. We chose the interval where the coupling is non-zero as the R-grid with 1000 mesh points, that is the interval $[0, 4.7375]$. The nonlocal dynamics is also calculated on this grid. The energy grid $[0.1, 100]$ eV with the logarithmic distribution of 600 energies turned out to be optimal since it seems that the low-energy behaviour and

[5] There is a typo in the sign of a_4 in cited paper [29].

also the exponential decay[6] are well captured on this grid. The nonlocal model was constructed from the low-energy data but the evaluation at large energies is necessary. We have to describe the whole shape of functions f_k in order to get the correct Hermitian part of the nonlocal potential given by integral transform (3.7). So, we have to choose the grid where the exponential decay is recognizable.

We fitted the first ten energy functions of the separable expansion of $V_{\mathrm{d}\epsilon}(R)$. We found out that six terms are sufficient to the good description of the AD cross sections. We discuss converging properties of the SVD expansion later. The fits are illustrated in Figure 3.1, which shows the first six SVD functions at mesh points (circles) and the resulting fits (curves). The parameters of the fitted functions together with the singular values σ_k are listed in Table 3.1. The particular values of the polynomial coefficients $c_n^{(k)}$ are not listed. As an example we show only the polynomial coefficients of the sixth energy function

$$\begin{aligned} p_6(\epsilon) = 0.05 - 2.2\epsilon + 16.3\epsilon^2 - 40.7\epsilon^3 + 48.2\epsilon^4 - 33.2\epsilon^5 \\ + 14.6\epsilon^6 - 4.0\epsilon^7 + 0.6\epsilon^8 - 0.04\epsilon^9. \end{aligned} \tag{3.37}$$

The other polynomials similarly change sings. The absolute value of the largest coefficient does not exceed the value of one hundred.

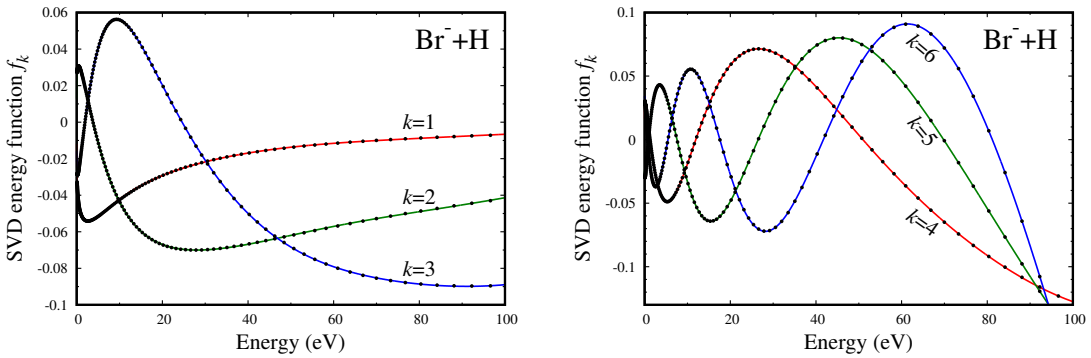

Figure 3.1: The SVD energy-dependent functions f_k of the $\mathrm{Br}^- + \mathrm{H}$ collision at logarithmically-distributed mesh points (dots) compared with the functions $\tilde{f}_k$ obtained by the fitting procedure (curves) for $k = 1, 2, 3$ (left) and $k = 4, 5, 6$ (right). The functions $k = 4, 5, 6$ have one more maximum, and then, they exponentially decay to zero.

Table 3.1: Parameters of the fitted SVD energy functions $\tilde{f}_k$ with $k = 1, \ldots, 6$ for the test example, the Br^-+H collision.

k	N_k	α_k	b_k	σ_k
1	4	0.222	1.6	49.68
2	5	0.170	1.6	14.82
3	6	0.138	1.7	5.09
4	7	0.135	1.9	1.53
5	8	0.085	1.9	0.42
6	9	0.035	1.8	0.10

[6]In fact, the exponential decay is not fully captured for $k = 4, 5, 6$ on this energy grid. However, we later see that the precision of the obtained results is sufficient.

We also investigated the influence of the chosen energy and space grids to the shape of the functions f_k. These functions are fairly independent of the choice of the space grid, whether we change the endpoints of the R-grid or the number of grid points. They do not dramatically depend on the ϵ-grid either. The functions are just rescaled in the vertical axis when we modify the number of mesh points. Roots of f_k are shifted closer to the origin when we decrease the lower endpoint of the ϵ-grid.

Next, we compare the eigenphase sum constructed directly from the nonlocal model with the eigenphase sum calculated from the coupling approximated by the sum of six separable terms (Figure 3.2). We calculated the AD cross sections with the same approximation of $V_{\mathrm{d}\epsilon}(R)$ for the partial waves $J = 0, \ldots, 19$ (Figure 3.3), and we compared the results with the cross sections computed by M. Čížek (personal communication, March 28, 2017) with the use of the third Bateman approximation. The difference is almost indistinguishable on the showed scale.

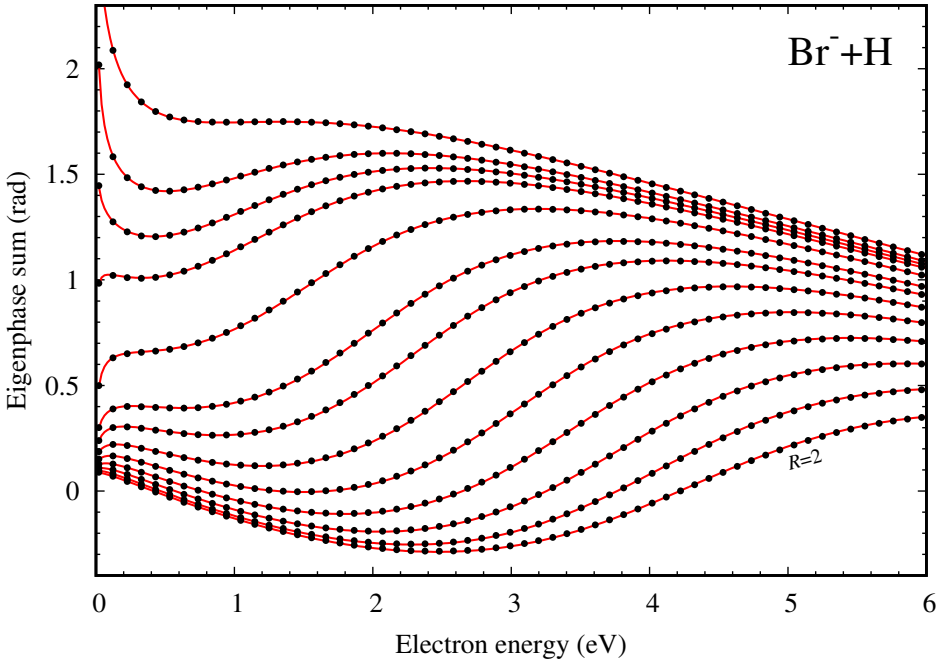

Figure 3.2: The comparison of eigenphase sum of the Br^-+H collision constructed directly from the nonlocal model [29] (red curves) with the eigenphase sum computed from the separated coupling potential (dots) at 13 values of the internuclear distance ($R = 2.0, 2.1, 2.3, 2.4, 2.5, 2.6, 2.6729, 2.8, 2.9, 2.95, 3.0,$ and 3.1 from bottom to top). The *ab initio* data are not shown.

In the end, we discuss the convergence of the $V_{\mathrm{d}\epsilon}(R)$ separation with the increasing number of SVD terms N_{c}. We calculated the cross section for the partial wave $J = 19$ with $N_{\mathrm{c}} = 2, \ldots, 6$ (Figure 3.4), and we compare the results with the Bateman approximation. The relative difference between the Bateman approximation and the curve with $N_{\mathrm{c}} = 6$ is much less than 1 %. In fact, we computed the cross section up to $N_{\mathrm{c}} = 10$. But the differences of these results and the calculation with $N_{\mathrm{c}} = 6$ are negligible. It seems that the developed method works well and we can use it in the investigation of the processes of interest.

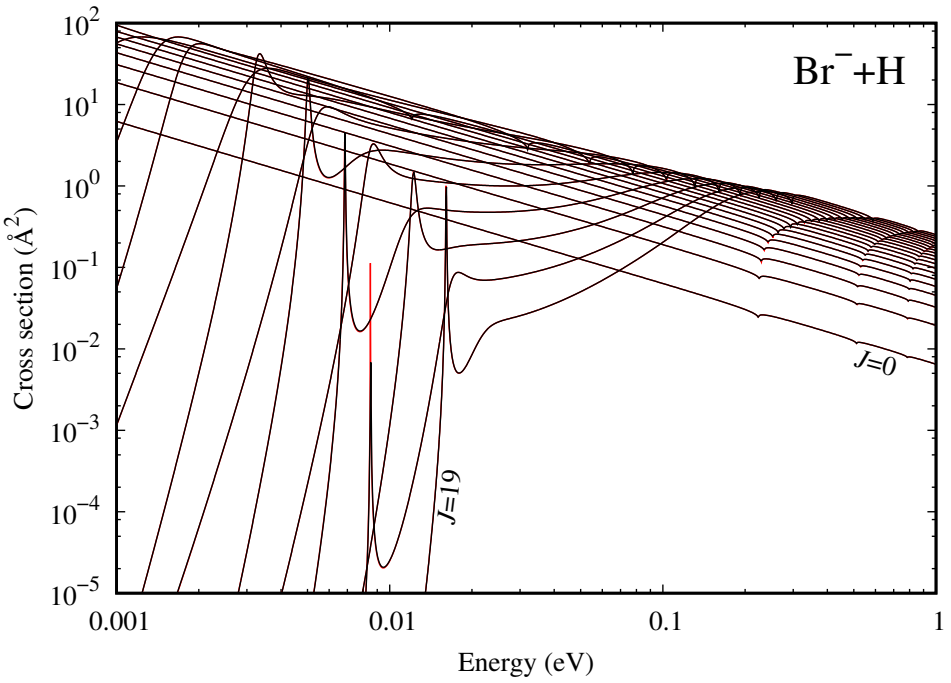

Figure 3.3: The AD cross sections of the $Br^- + H$ collision computed by two methods of the coupling separation, the third Bateman approximation (black) and the SVD method with six separable terms (red), for partial waves $J = 0, \ldots, 19$ (from bottom to top) in the logarithmic scale. The curves obtained by the different methods are almost indistinguishable on this scale.

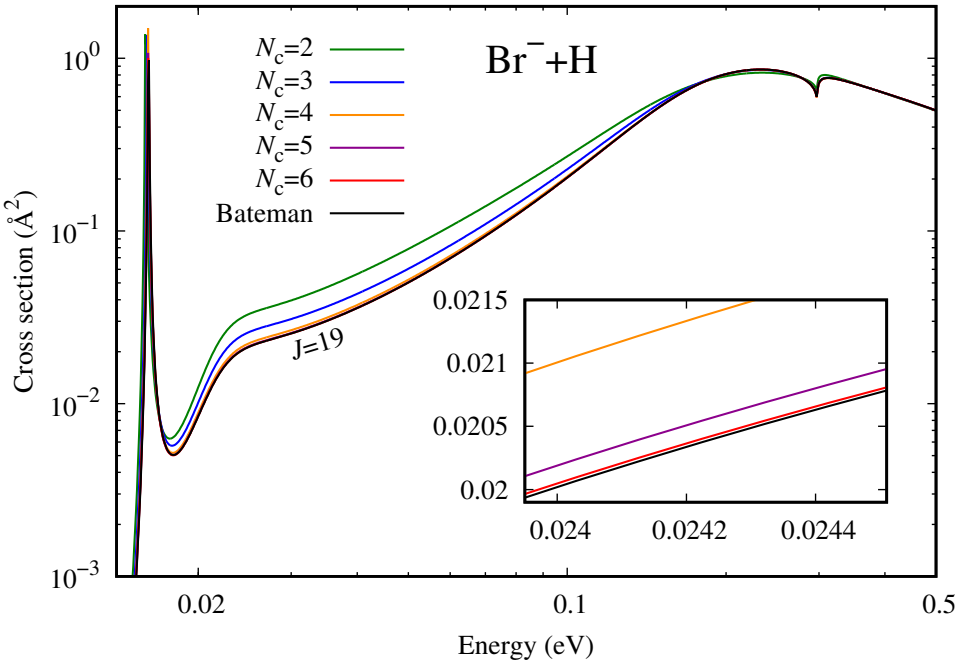

Figure 3.4: The convergence of the AD cross section of the $Br^- + H$ collision with the increasing number of SVD terms N_c in the logarithmic scale and the comparison with the third Bateman approximation.

3.7 Numerical details

In the last section of this chapter, we very briefly mention some numerical methods used in cross section calculations within the nonlocal resonant theory. The detailed description is again included in book [4] and references therein.

Lippman-Schwinger equation (1.44) with the nonlocal potential is solved. We first need to obtain the initial state $\phi_J(R)$ and be able to act with the integral kernel on a vector. The initial state satisfies Lippman-Schwinger equation (1.49), which is the Fredholm integral equation of the second kind. The equation is rewrite to the Volterra equation of the second kind. Then, an effective algorithm provides the regular $\phi_J(R)$ and irregular $\phi_J^{(\mathrm{irr})}(R)$ solutions, and also the local part of the T-matrix. The local Green's function G_J is given from these two solutions by

$$G_J(E, R, R') = -\frac{2\mu}{K}\phi_J(R_<)\phi_J^{(\mathrm{irr})}(R_>), \tag{3.38}$$

where $R_< = \min(R, R')$ and $R_> = \max(R, R')$.

The Fourier DVR method is used to calculate vibrational states $\chi_{\nu J}(R)$ (1.45) of the neutral molecule, which are contained in the expansion of nonlocal potential (3.6). The expansion is cut off at some point, that is only finite number of vibrational states is considered. The molecule is closed into a box. The vibrational functions are expressed as an expansion in the Fourier basis. The coefficients of the Fourier expansion are then determined as the eigenvectors of the molecular Hamiltonian expressed in the Fourier basis. The energies of the vibrational states correspond to the eigenvalues. The idea of the DVR method [37] is so that matrix elements of the potential energy are obtained using a matrix transformation, which diagonalizes the operator $\hat{x}$ in the basis. The DVR method give the correct discretization of the continuum, which contributes to cross sections [38].

Finally, Equation (1.44) is solved by the Schwinger-Lancozs algorithm (SL) developed by Meyer et al. [30], which is based on the Schwinger variational principle and the Lanczos algorithm from matrix iteration methods. The SL algorithm also provides the resonant part of the T-matrix.

In some cases, it is possible to accelerate the convergence of the SL algorithm by the energy-dependent local approximation investigated by Horáček et al. [39]. In the Lippman-Schwinger equation, the effective potential is partitioned as

$$V = V_\mathrm{d} + F_J. \tag{3.39}$$

Another partitioning can accelerate the convergence

$$V = V'_\mathrm{d} + F'_J, \tag{3.40}$$

where $V'_\mathrm{d} = V_\mathrm{d} + F_J^\mathrm{loc}$ and $F'_J = F_J - F_J^\mathrm{loc}$ with the energy-dependent local approximation defined by

$$F_J^\mathrm{loc}(E, R) = \int \mathrm{d}R' F_J(E, R, R'). \tag{3.41}$$

This approach is equivalent to a certain form of preconditioning well known in iterative matrix methods.

When we analyse the studied processes in the next chapters, we also discuss the sensitivity of cross sections to major numerical parameters, which are listed in Table 3.2 together with the explanation of their meaning.

Table 3.2: Major numerical parameters of nonlocal calculations and their meaning.

R_{min}	the lower endpoint of the nonlocal grid[a]
R_{max}	the upper endpoint of the nonlocal grid
R_{DVR}	the upper endpoint[b] of the DVR grid[c]
N_{R}	the number of mesh points of the nonlocal grid
N_{v}	the number of vibrational states in the expansion of F
N_{c}	the number of separable terms in the SVD approximation of $V_{\mathrm{d}\epsilon}$

[a] The grid where the nonlocal dynamics is solved.
[b] The lower endpoint of the DVR grid is the same as R_{min}.
[c] The grid where the vibrational states are computed by the Fourier DVR method.

4. Li+H$^-$ collision

4.1 Introduction

After the development of the separation procedure, we are finally able to calculate AD cross sections of the studied processes. This chapter is devoted to the analysis of Li+H$^-$ collision (2.1). First, we discuss the separation of the discrete-state-continuum-coupling potential. Second, we show and discuss the obtained cross sections and we examine their sensitivity to various numerical parameters. Third, we present two additional nonlocal resonant models of the Li+H$^-$ channel, which are consistent with the *ab initio* data, and we compare the results. In the end, we discuss rate constants and their comparison with the estimate used previously for cosmological simulations [1].

4.2 Coupling separation

To separate the coupling potential $V_{\mathrm{d}\epsilon}(R)$, we follow the procedure outlined in Section 3.3. We found out that the appropriate energy grid is [0.001,10] eV with the logarithmic distribution of 600 energies. The low-energy behaviour and the exponential decay of the SVD energy functions f_k are well recognizable on the chosen mesh. The space grid is again selected as the grid where the nonlocal dynamics takes place. We discuss the particular choice later.

We show the best obtained fit of the first six SVD functions f_k in Figure 4.1. The parameters N_k, α_k, and b_k of fits by function (3.12) and the singular values σ_k are listed in Table 4.1.

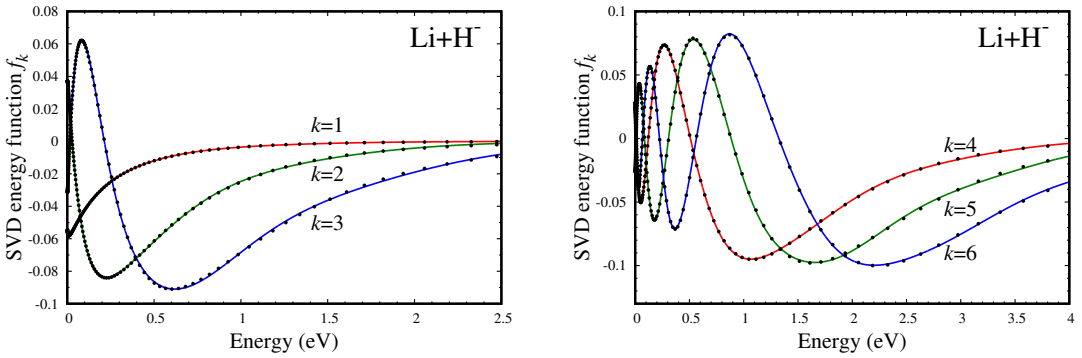

Figure 4.1: The SVD energy-dependent functions f_k of the Li+H$^-$ collision at logarithmically-distributed mesh points (dots) compared with the functions $\tilde{f}_k$ obtained by the fitting procedure (curves) for $k = 1, 2, 3$ (left) and $k = 4, 5, 6$ (right).

In contrast to the test example, the parameter b_k has much higher values, compare the results in Tables 3.1 and 4.1. The reason for the mentioned behaviour comes from the comparison of the energy functions in these two cases, compare Figures 3.1 and 4.1. The oscillations are located in much smaller energy region (several eV) in the Li+H$^-$ channel than it is in the test case (tens of eV).

Apparently for this reason, the polynomial coefficients are very large in the absolute value in the Li+H^- case. For example, the polynomial of the sixth term in the separable expansion is given by

$$\begin{aligned} p_6(\epsilon) = 0.05 &- 0.21 \times 10^3\epsilon + 0.13 \times 10^6\epsilon^2 - 0.29 \times 10^8\epsilon^3 \\ &+ 0.32 \times 10^{10}\epsilon^4 - 0.22 \times 10^{12}\epsilon^5 + 0.97 \times 10^{13}\epsilon^6 \\ &- 0.30 \times 10^{15}\epsilon^7 + 0.63 \times 10^{16}\epsilon^8 - 0.92 \times 10^{17}\epsilon^9 \\ &+ 0.89 \times 10^{18}\epsilon^{10} - 0.55 \times 10^{19}\epsilon^{11} + 0.19 \times 10^{20}\epsilon^{12} \\ &- 0.30 \times 10^{20}\epsilon^{13}. \end{aligned} \tag{4.1}$$

The coefficients of the highest powers reach values in the order of 10^{20} in the absolute value. The exponential decay has to be strong enough to compensate the polynomial growth, which implies the large values of b_k, but it overly suppresses the oscillations at higher energies. Therefore, a high-degree polynomial is needed to describe the full range where the functions are non-zero.

The described behaviour of the polynomial coefficients may cause numerical problems. The fitted functions are used to calculate energy-dependent part (3.13) of the nonlocal potential, where the multiplication of two energy functions occurs. The resulting product, which is a quite small number, is obtained as the sum of $N_k + N_{k'} + 1$ terms with alternating signs. In addition, some of these terms are fairly large. The rounding error of the sum may be significant compared to the magnitude of the result. This kind of error is called 'smearing error' in numerical analysis. To avoid these problems we calculate the polynomial multiplication in the quadruple precision (twice more precise than the standard double precision). We performed some numerical tests and we found out that we are capable of calculating the mentioned product in the quadruple precision with the error less than 10^{-8} for polynomials with the maximal degree about $N_k \approx 15$. The error is determined as the difference between two calculations for tests of precision. We multiply the polynomials, and then, we calculate the result at some energy, or we can first calculate the values of both polynomials at the given energy, and afterwards, we multiply these two numbers. The second method is much less burdened by rounding errors, because we sum fewer and smaller terms, but the latter method is not applicable in calculation of cross sections, because we need the analytical formula of the resulting polynomial in order to be able to compute the energy-dependent part of F.

We calculated the AD cross section for the partial wave $J = 0$ with the number of separable terms $N_c = 2, \ldots, 6$ (Figure 4.2).[1] The separable expansion converges faster than it is in the test example, see Section 3.6, four terms are sufficient. The relative differences between the cross sections with $N_c = 4$ and the best result with $N_c = 6$ are less than 1.4 % in the entire interval where the cross section was computed (from 1 meV to 1 eV). The largest difference occurs around local maxima of the cross section. The figure shows the region below the first local maximum.[2] For the most energies the difference is much less than 1 %. Therefore, we use only four terms in the next calculations in order to shorten the

[1] Here, there is no reason to omit the eigenphase sum at $R = 3.6$ since we do not compare the results with the *ab initio* data and the model predicts the curve at this R without the second resonance, see Section 2.4.

[2] The maximum occurs above the first Wigner cusp. We explain this term in the next section.

computational time. The time complexity is quadratic in the number of separable terms N_c, since we sum over k, k' in the expansion of the nonlocal potential given by Formula (3.6).

The eigenphase sum determined from the separable approximation of $V_{d\epsilon}(R)$ with four terms agrees with the direct results from the nonlocal model very well (Figure 4.3).

Table 4.1: Parameters of the fitted SVD energy functions $\tilde{f}_k$ with $k = 1, \ldots, 6$ for the Li+H$^-$ collision.

k	N_k	α_k	b_k	σ_k
1	4	0.049	123.5	166.39
2	5	0.046	132.5	24.28
3	7	0.040	131.0	6.09
4	9	0.030	125.0	1.69
5	11	0.036	126.0	0.50
6	13	0.040	123.5	0.15

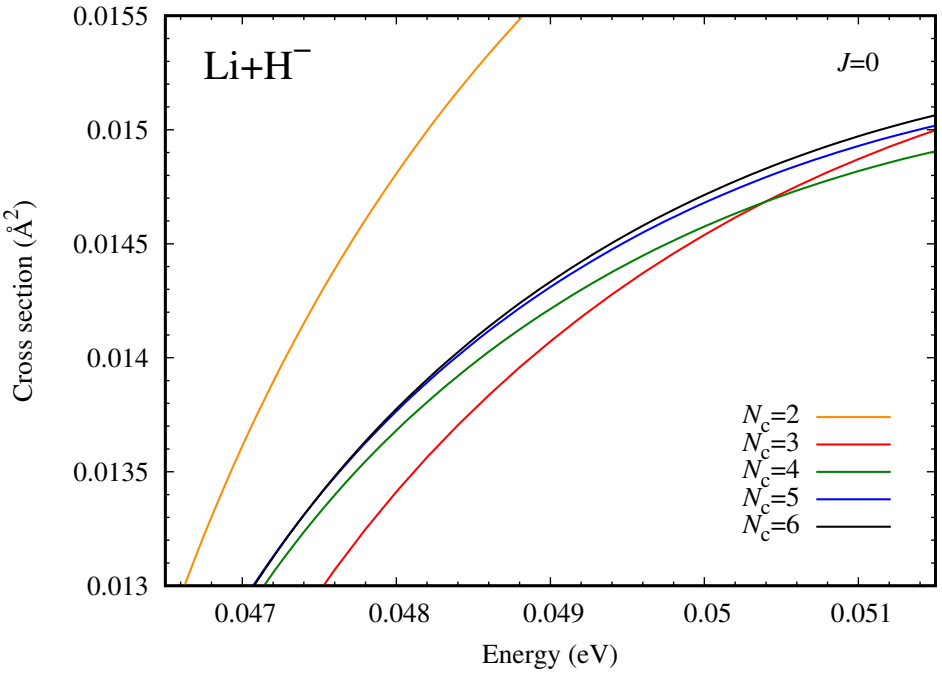

Figure 4.2: The convergence of the AD cross section of the Li+H$^-$ collision for the partial wave $J = 0$ with the increasing number of separable terms $N_c = 2, \ldots, 6$. The figure depicts one of energy regions where differences among the curves are largest.

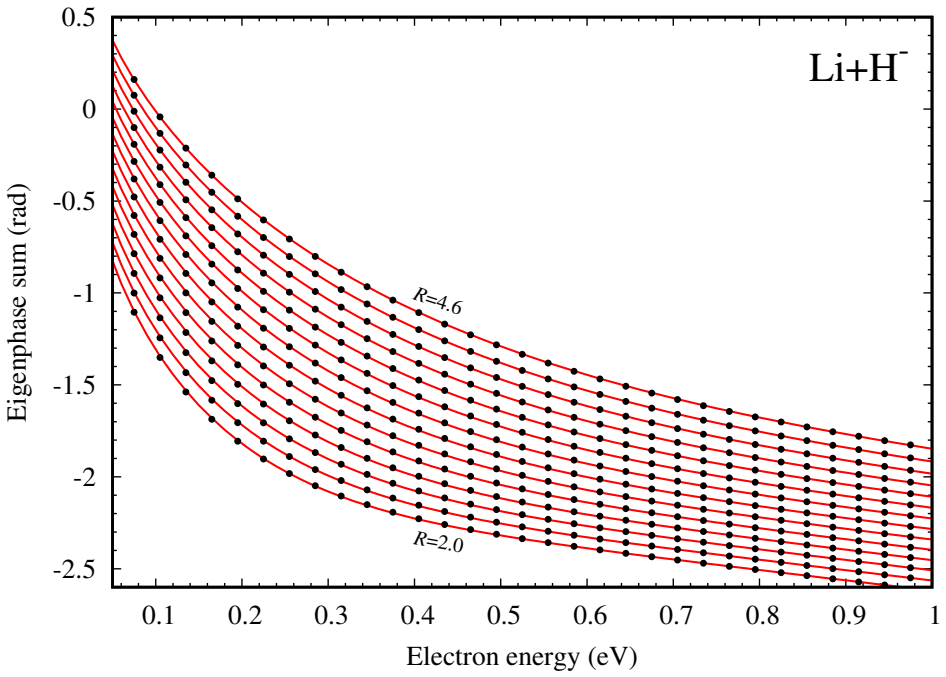

Figure 4.3: The comparison of the eigenphase sum of the Li+H$^-$ collision constructed directly from the nonlocal model (red curves) with the eigenphase sum computed from the separated coupling potential with four SVD terms (dots) at 14 values of the internuclear distance ($R = 2.0$ to 4.6 with step 0.2 from bottom to top).

4.3 AD cross sections

We first show the obtained AD cross sections for the individual partial waves $J = 0, \ldots, 60$ together with the total AD cross section. All final results were calculated with the optimal values of numerical parameters, which are listed in Table 4.2 (their meaning is in Table 3.2). Here, we interpret various phenomena and structures visible in the shape of the cross sections. In the next section, we also discuss the choice of the optimal numerical parameters and their influence to the cross sections.

Table 4.2: The optimal numerical parameters of nonlocal calculations for the Li+H$^-$ collision.

parameter	partial waves J
$R_{\mathrm{min}} = 0.01$	$0, \ldots, 35$
$R_{\mathrm{min}} = 0.05$	$36, \ldots, 48$
$R_{\mathrm{min}} = 0.10$	$49, \ldots, 60$
$R_{\mathrm{max}} = 20$	all
$R_{\mathrm{DVR}} = 20$	all
$N_{\mathrm{R}} = 6000$	all
$N_{\mathrm{v}} = 90$	all
$N_{\mathrm{c}} = 4$	all

For clarity, we split up the results into Figures (4.4) and (4.5), which depict the AD cross sections for the partial waves $J = 0, \ldots, 12$ and $J = 18, \ldots, 60$ respectively in the logarithmic scale. The total AD cross section (green) determined as the sum of all partial contributions is shown as well in both the figures. The number of computed partial waves is sufficient to obtain the converged total AD cross section in the entire considered energy interval (from 1 meV to 1 eV). The partial waves $J = 13, \ldots, 17$ are not shown. Their shape is similar to the curves $J = 0, \ldots, 12$.

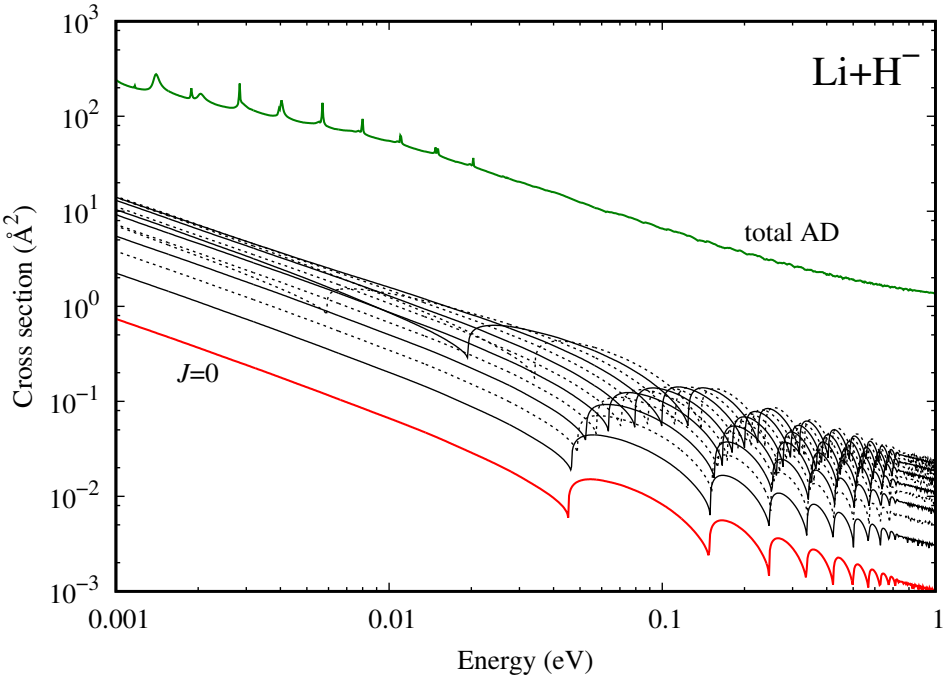

Figure 4.4: The AD cross sections of the Li+H$^-$ collision for the partial waves $J = 0, \ldots, 12$ (from bottom to top, each other curve is dashed, $J = 0$ red) together with the total AD cross section (green) in the logarithmic scale.

The nonlocal resonant model of the Li+H$^-$ collision does not correspond with the *ab initio* data at very low energies, see Section 2.6 and Figure 2.4. This disagreement influences the shape of the cross sections in the immediate vicinity (about 10 meV) of vibrational thresholds. These sharp structures in the cross sections are discuss in detail below.

The presented results may not be valid at energies above the dissociation limit, which is given by the electron affinity of the hydrogen atom[3] 0.740 eV in this case. Above this limit, the dissociation channel opens

$$\mathrm{Li} + \mathrm{H}^- \rightarrow \mathrm{Li} + \mathrm{H} + \mathrm{e}^-. \tag{4.2}$$

The process is necessary to consider in the description of associative detachment at these energies. We show the results above the dissociation threshold up to 1 eV but we keep in mind that their validity is questionable.

The overall shape of the cross sections is given by the attraction of the ground anion potential at large internuclear distances, see again Figure 2.1. Thus, the

[3]We use the electron affinities obtained from the MOLPRO calculations, see Section 2.2.3.

particle[4] with small energy reaches the region where the electron detachment may occur, that is the region where the coupling potential is non-zero. The mutual vertical shift, which is well visible for lower partial waves in Figure 4.4, is caused by the multiplicative factor $2J + 1$, which appears in the cross section formula, see Formulas (1.51) or (1.52). The partial waves $J = 0, \ldots, 18$ seem to diverge at zero energy.[5] On the other-hand, the cross sections $J \geq 19$ rise from zero. This behaviour is related to the height of the centrifugal barrier. We return to this problem later.

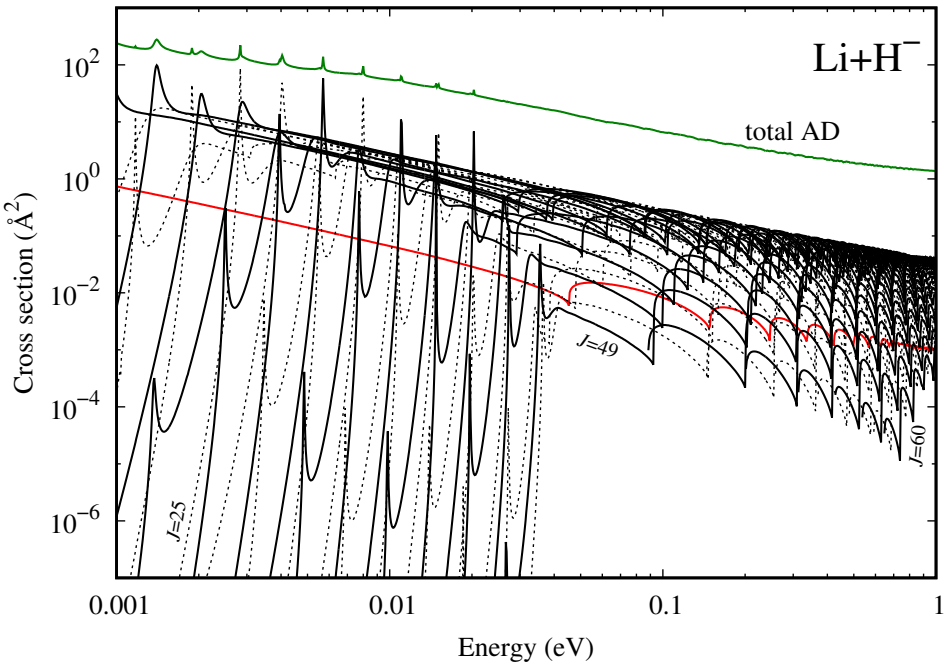

Figure 4.5: The AD cross sections of the Li+H$^-$ collision for the partial waves $J = 18, \ldots, 60$ (from left to right, each other curve is dashed) together with the total AD cross section (green) in the logarithmic scale. For comparison, the partial wave $J = 0$ (red) is shown as well.

Two types of structures are visible in the cross sections, Wigner cusps and orbital resonances. The Wigner cusps are the sudden change of cross sections at the opening of a new vibrational excitation channel, that is a new final state of the molecule LiH comes to existence. Sharp peaks visible in higher partial waves ($J \geq 20$ in Figure 4.5) are called the orbital resonances. We explain the origin of both the structures using an effective potential

$$V_{\text{eff}}^{(J)}(R) = V(R) + \frac{J(J+1)}{2\mu R^2}, \tag{4.3}$$

where we add the centrifugal term proportional to R^{-2} to a potential $V(R)$, which represents the neutral potential $V_0(R)$ in the interpretation of the Wigner cusps

[4]The description of the scattering problem of two colliding particles is reformulated to scattering of one particle with the reduced mass by an effective spherical, in our case nonlocal, potential.

[5]The cross sections are shown in the logarithmic scale.

and the local anion potential $V_{\mathrm{loc}}(R)$ (the potential of the $X^2\Sigma^+$ state) in the case of the orbital resonances.

The local anion potential is attractive at large internuclear distances, see again Figure 2.5. Therefore, quasi-stable states with positive energies[6] may exist in the effective potential with the local potential for $J > 0$. The particle can tunnel through the centrifugal barrier and reach the inner potential well, which we graphically illustrate below. Then, if the collision energy is close to the energy of some quasi-stable state, the particle is trapped in this state. The state is not bound, and thus, the particle can again escape by the tunnel effect, but the probability of the detachment to some vibrational state of LiH increases as the particle orbits the scattering centre, which implies the rapid increase in the magnitude of AD cross sections at collision energies close to the energies of the quasi-stable states.

We graphically illustrate the described structures in terms of potentials (Figure 4.6) and later on an example for a particular partial wave. The Wigner cusps appear in the cross section if the collision energy, which is measured from zero fixed by the asymptote of $V_{\mathrm{loc}}(R)$ as $R \to \infty$ (highlighted by the green horizontal line), is close to some vibrational state of LiH (horizontal dashed lines). Local minima of effective neutral potentials (red curves) rise with increasing J. Thus, the energies of vibrational states rise as well, which explains the shift of the Wigner cusps towards higher energies in higher partial waves. The cusp appears at 6 meV in the partial wave $J = 10$, that is at lower energy than the energy of the lowest Wigner cusp in the partial wave $J = 0$. This is caused by the fact that the energy of the corresponding vibrational state is negative for $J < 10$ and it becomes positive in partial waves $J \geq 10$.

The bottom of the neutral potential well is so high for partial waves $J \geq 49$ that energy of the ground vibrational state is positive. The associate detachment channel is closed at collision energies which are lower than the energies of these ground states. In other words, AD cross section is strictly zero at these energies because there is no possible final state of the molecule LiH. Therefore, high partial waves start at finite value of cross section, which is barely visible in Figure 4.5.

The orbital resonances are caused by the presence of quasi-stable states of effective local potentials (blue curves in Figure 4.6). The centrifugal barrier exists for each $J > 0$, and the corresponding effective potential is attractive at some internuclear distances even for the largest considered partial wave $J = 60$. If the barrier is high enough, states with positive energies exist.

Now, it is convenient to return to the problem regarding the low-energy behaviour of the cross sections that we start talking about few paragraphs above. The incoming particle first needs to overcome the centrifugal barrier because the coupling potential is located at small internuclear distances up to 10-15 bohrs. The barrier is located at similar or larger R, especially for low partial waves. We provide further details later when we deal with the optimal size of the non-local grid. If the collision energy is small compared to the centrifugal barrier, the influence of the quantum tunnel effect is weak and the particle bounce back with high probability. In that case, the cross section is substantially suppressed. The height of the centrifugal barrier increases with the increasing value of J, and thus, the initial growth of the cross sections is shifted to larger energies. There

[6] Zero energy is fixed by $V_{\mathrm{loc}}(R) \to 0$ as $R \to \infty$.

is no visible initial growth in the partial waves $J = 1, \ldots, 18$ because the height of the barrier is less than 1 meV. The AD cross section of the partial wave $J = 0$ truly diverges since there is no centrifugal barrier. Therefore, the total AD cross section divergences at zero energy as well.

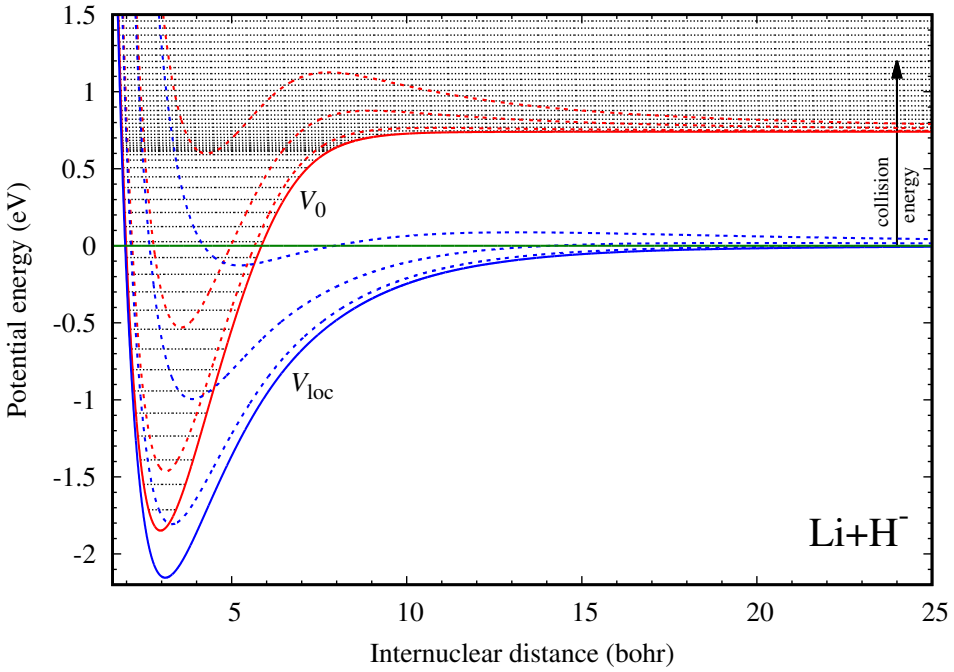

Figure 4.6: The illustration of the structures in the AD cross sections using effective neutral and anion potentials with the centrifugal barrier (red and blue curves for $J = 0, 20, 40, 60$ from bottom to top respectively). Horizontal dashed lines denote vibrational levels in the neutral potential ($J = 0$). The green line highlights zero energy.

To illustrate the origin of the Wigner cusps and orbital resonances even more transparently, we give a particular example in the case of the partial wave $J = 45$ in Figure 4.7, which consists of two parts. The left-hand figure depicts neutral and local effective potentials with $J = 45$ (red and blue curves respectively).The right-hand figure shows the AD cross section $J = 45$ rotated by 90 degrees counter-clockwise, that is the energy axis is vertical. Dotted horizontal lines indicate the connection of the structures with the positions of quasi-stable and vibrational states. To estimate the positions of the quasi-stable anion states, we again used the Fourier DVR method with the box [0.01,17.70].

We conclude the discussion by mentioning the local complex approximation introduced in Section 1.6 in the case of the Li+H$^-$ collision. The neutral and anion potentials do not cross. The anion state is bound at all internuclear distances. In this situation, it can be shown that $E_{\rm res}(R)$ defined by Equation (1.65) is negative for each R. The anti-Hermitian component $\Gamma(\epsilon, R, R')$ of the nonlocal potential vanishes at negative energies, which implies that imaginary part (1.64) of the local complex potential vanishes as well. So, we can not compute AD cross sections in this approximation.

In general, the correct overall qualitative but usually not quantitative behaviour of AD cross sections and even the orbital resonances can be described in

the local approximation. Wigner cusps come from the description within the non-local theory since the potential of the local approximation is energy-independent.

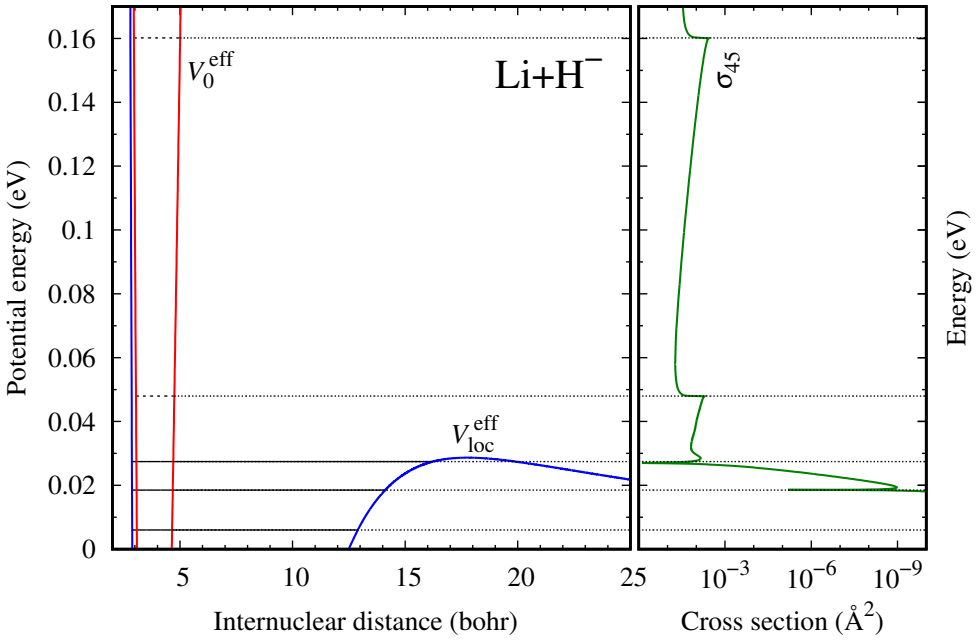

Figure 4.7: The demonstration of the orbital resonances and Wigner cusps in the AD cross section of the Li+H$^-$ collision for the partial wave $J = 45$. The left-hand figure shows neutral and local effective potentials in this case (red and blue), vibrational energies of the neutral potential with $J = 45$ (dashed horizontal lines), quasi-stable levels of the anion potential with $J = 45$ (solid horizontal lines). The right-hand figure depicts the AD cross section of the partial wave $J = 45$ (green curve) rotated by 90 degrees counter-clockwise. Dotted horizontal lines indicate the connection between the structures in the cross section and the vibrational and quasi-stable levels in the potentials.

4.4 Numerical tests

It turned out that the Schwinger-Lanczos algorithm converges very slowly in this case, see Table 4.3, where we list examples of the needed numbers of iterations. These results were obtained with the use of the preconditioning described in Section 3.7. The iterations stop when the relative error of two consecutive results for the T-matrix is less than 10^{-13}. The sufficient number of iterations is typically up to 20 in similar scattering problems.

In addition to the high number of iterations, the relatively large number of mesh points and vibrational states were required, which significantly increased computational times, which can be seen in Table 4.4, where we show indicative times in hours that elapsed during the calculations with the use of preconditioning and without it. The preconditioning was not always beneficial. Each calculation was performed on one CPU core of a computer cluster with the optimal numerical parameters at 1000 logarithmically-distributed energies in the energy interval [0.001,1] eV. Higher partial waves take less time that the lower ones since the calculation stops when the cross section is less than 10^{-8} Å^2.

Table 4.3: Numbers of the Schwinger-Lanczos iterations in nonlocal calculations of the Li+H$^-$ collision for the partial waves $J = 0, 20, 40$ at various energies.

E (eV)	$J = 0$	$J = 20$	$J = 40$
1.000	196	230	158
0.320	146	101	75
0.100	102	85	67
0.032	79	66	167
0.010	72	79	—
0.003	69	101	—
0.001	69	80	—

Table 4.4: Computational times of cross section calculations of the Li+H$^-$ collision for the partial waves $J = 0, 20, 40$ at 1000 logarithmically distributed energies in the energy interval [0.001,1] eV.

J	preconditioning	no preconditioning
0	8.5 h	11.8 h
20	8.6 h	9.9 h
40	6.6 h	4.9 h

Now, we come to the sensitivity of the cross sections to numerical parameters listed in Table 3.2. We justify the choice of the optimal parameters, which are listed in Table 4.2. We already discuss the convergence of the cross sections with the increasing number of separable terms in the $V_{\mathrm{d}\epsilon}(R)$ separation. Four terms are sufficient, see Section 4.2.

The correct boundary condition of a regular solution is that the corresponding wave function vanishes at $R = 0$, that is the proper choice of the lower endpoint of the nonlocal grid would be $R_{\mathrm{min}} = 0$. But non-zero value of R_{min} is convenient because the centrifugal term diverges as $R \to 0$. A small non-zero value has no influence on cross sections. Small internuclear distances are classically forbidden regions since potentials are repulsive there, and thus, the regular solution is exponentially suppressed and the irregular solution is exponentially enhanced. We verified that the results are not truly sensitive to the particular values of R_{min} listed in Table 4.2. It is necessary to increase R_{min} for large J since the exponential suppression/enhancement of wave functions is too strong that causes numerical overflow.

The nonlocal potential is non-zero only in the finite interval of internuclear distances in the test example, see Equations (3.31) and (3.32). The upper endpoint of this interval is the natural choice of the upper endpoint of the nonlocal grid R_{max}. In the Li+H$^-$ collision, we constructed discrete-state potential (2.8) from the knowledge of the local potential. The discrete-state potential is non-smooth if the coupling completely vanishes at a finite distance. Therefore, the nonlocal model was constructed to exponentially decay to zero as $R \to \infty$, see

Formula (2.13). The upper endpoint needs to be chosen in the region where the coupling is negligible. The magnitude of the width and level-shift functions is about 10^{-4} and 10^{-8} at $R = 15$ and 20 respectively.

The upper endpoint R_{DVR} of the DVR grid and the number N_{v} of vibrational states are closely related to the value of R_{max}. We ran series of tests for the cross section $J = 0$, where we fixed R_{DVR} and performed several calculations with various R_{max}, $N_{\mathrm{v}} = 150$, and with a constant step of the equidistant nonlocal mesh (Table 4.5). To ensure the same description of the vibrational states within the DVR method with different values of R_{DVR}, we changed the total number of calculated vibrational states N_{DVR} and we kept the ratio $R_{\mathrm{DVR}}/N_{\mathrm{DVR}}$ to be constant. The number N_{DVR} designates the total number of vibrational states that are calculated but only N_{v} states are used in the expansion of the nonlocal potential given by Formula 3.6.

Table 4.5: Test calculations of the cross section $J = 0$ of the Li+H^- collision with various values of R_{DVR}, N_{DVR}, and R_{max}.

R_{DVR}	N_{DVR}	R_{max}
20	160	15, 18, 20
25	200	15, 18, 20, 25
30	240	15, 18, 20, 25, 30

From the tests described above, we found out that the computed cross sections are fairly independent with respect to R_{DVR}. The relative errors are in hundredths of percent. The sufficient upper endpoint turned out to be $R_{\mathrm{max}} = 20$, which is illustrated in Figure 4.8, where the energy region around the first Wigner cusp of the cross section $J = 0$ is shown. We chose $R_{\mathrm{max}} = 20$ and $R_{\mathrm{DVR}} = 20$ as the optimal values.

The above calculations were all carried out with $N_{\mathrm{v}} = 150$. Further, we test the sensitivity of the cross section for the partial wave $J = 0$ to different numbers of vibrational states (Figure 4.9). There exist 24 vibrational states with energies below the dissociation limit but their number depends on the total number of computed vibrational states N_{DVR} and on the upper endpoint of the DVR grid R_{DVR}. We obtained 24 bound states with $N_{\mathrm{DVR}} = 160$ and $R_{\mathrm{DVR}} = 20$. We need at least $N_{\mathrm{v}} = 90$ states to obtain the converged cross sections up to 1 eV. So, the continuum-discretized states greatly contributes at energies below the dissociation limit. We remind that the results above the limit are questionable because we did not consider the dissociation channel given by Equation (4.2).

In theory, cross sections calculated from the T-matrix by Formula (1.51) and from individual vibrational contributions by Formula (1.52) give the same results. However, the latter formula is better from the numerical point of view. The first mentioned formula is numerically unstable since the subtraction of typically close numbers occurs (Figure 4.10). The numerical instability is clearly visible in the left-hand part of the figure. Sum over vibrational contributions (1.52) is not only stable but also provides more accurate results with fewer mesh points because the rounding errors of the T-matrix approach are not negligible.

At last, we discuss the proper choice of the number N_{R} of nonlocal mesh

points. We calculated the cross section $J = 22$ with various values of N_{R} (Figures 4.11 and 4.12). The first figure depicts the region around the orbital resonance. The region above the second Wigner cusps is shown in the other figure. It is sufficient to choose $N_{\mathrm{R}} = 6000$, which corresponds to the equidistant grid step $1/3 \times 10^{-3}$. The relative difference between the curves with $N_{\mathrm{R}} = 6000$ and 8000 is much less than 1 %.

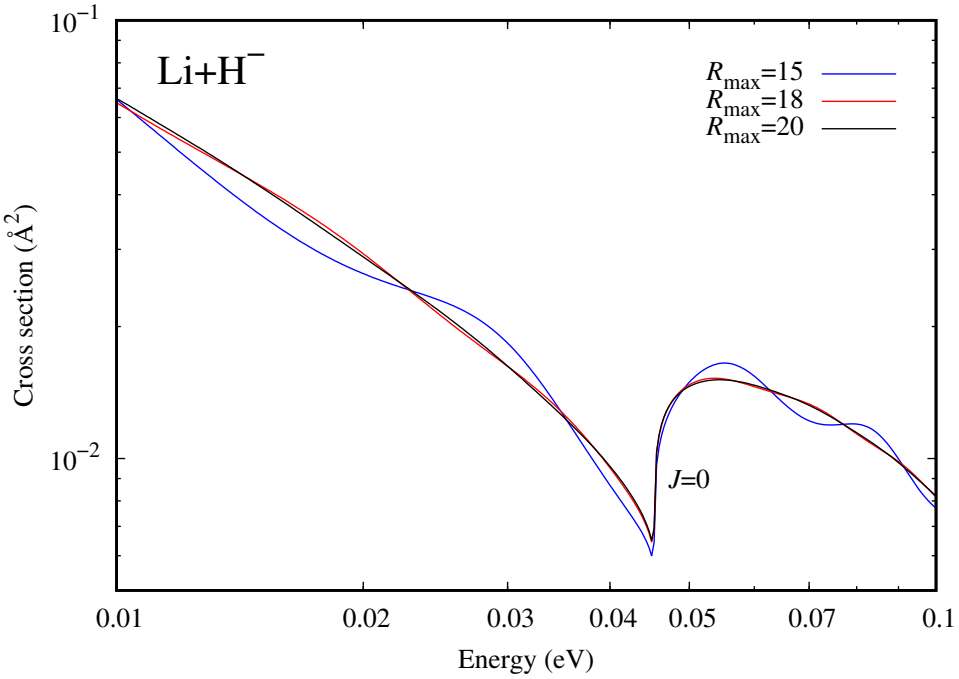

Figure 4.8: The sensitivity of the AD cross section of the Li+H^- collision for the partial wave $J = 0$ to the upper endpoint of the nonlocal grid $R_{\max} = 15, 18, 20$ in the logarithmic scale. The showed region is located around the first Wigner cusp, where the differences are the largest.

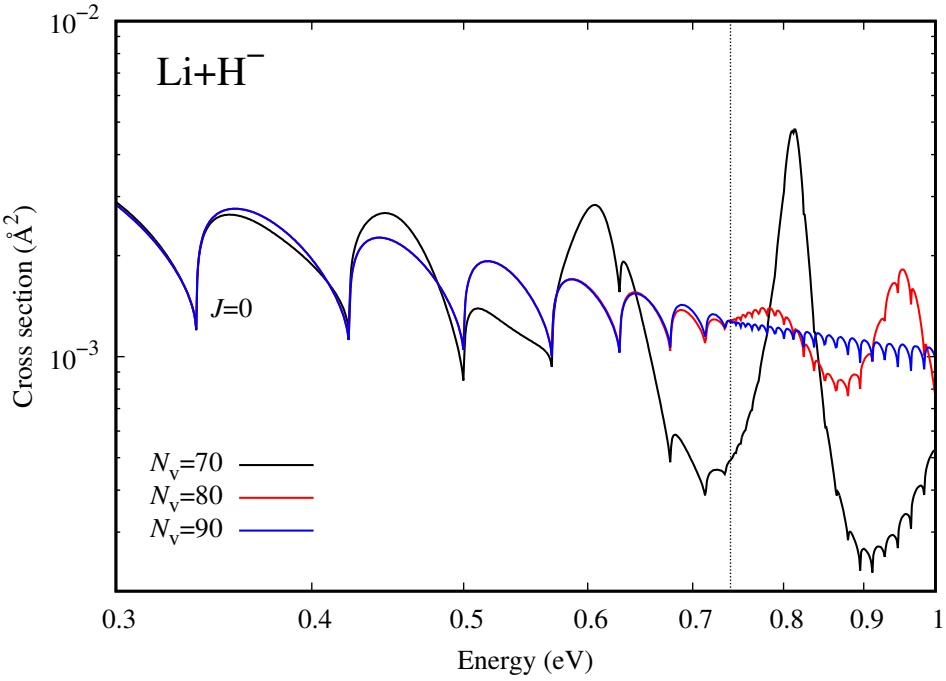

Figure 4.9: The sensitivity of the AD cross section of the Li+H$^-$ collision for the partial wave $J = 0$ to the number of vibrational states $N_\mathrm{v} = 70, 80, 90$ in the expansion of the nonlocal potential in the logarithmic scale. The vertical dashed line denotes the dissociation limit 0.74 eV given by the electron affinity of hydrogen atom from the MOLPRO calculations.

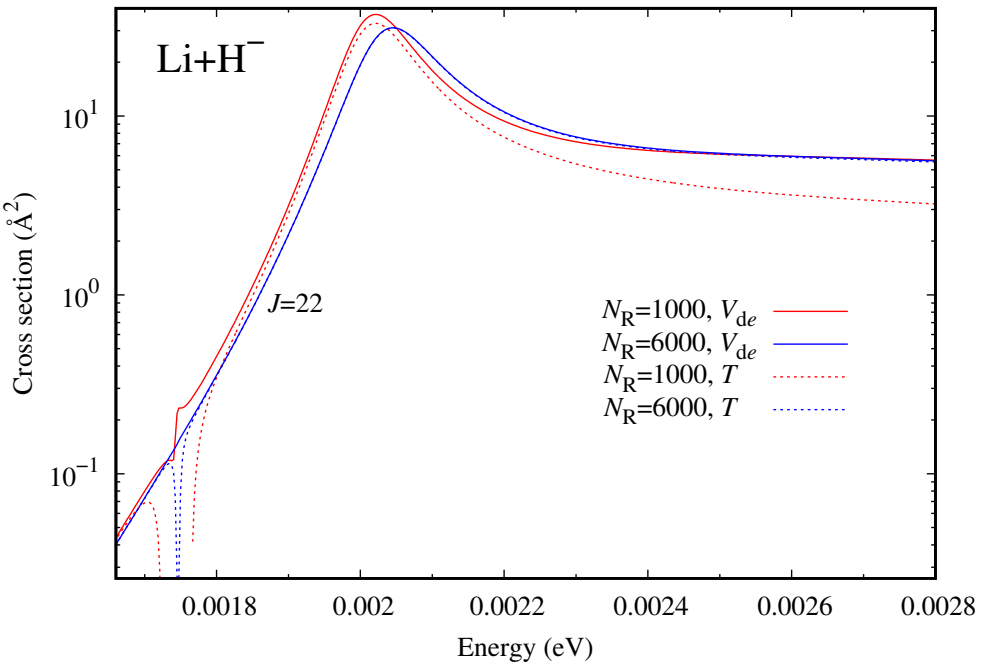

Figure 4.10: The comparison of the AD cross section of the Li+H$^-$ collision for the partial wave $J = 22$ calculated by two different formulas, the numerically unstable formula which uses the T-matrix (dashed, designated by T), and the sum of individual vibrational contributions (solid, designated by V_de).

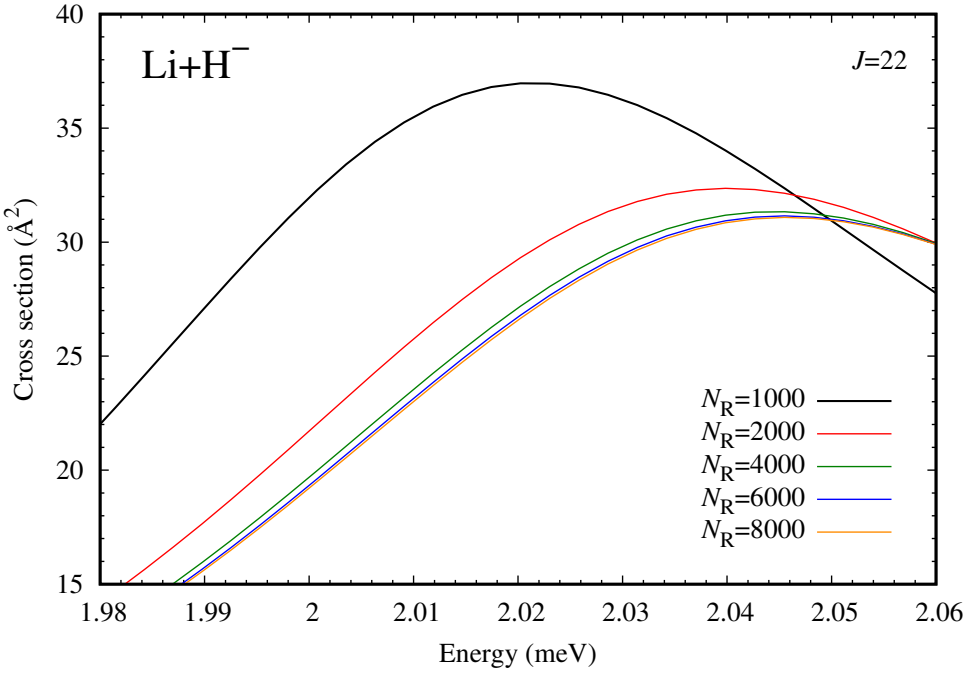

Figure 4.11: The sensitivity of the AD cross section of the Li+H$^-$ collision for the partial wave $J = 22$ to the number of mesh points. The figure shows the area around the orbital resonance.

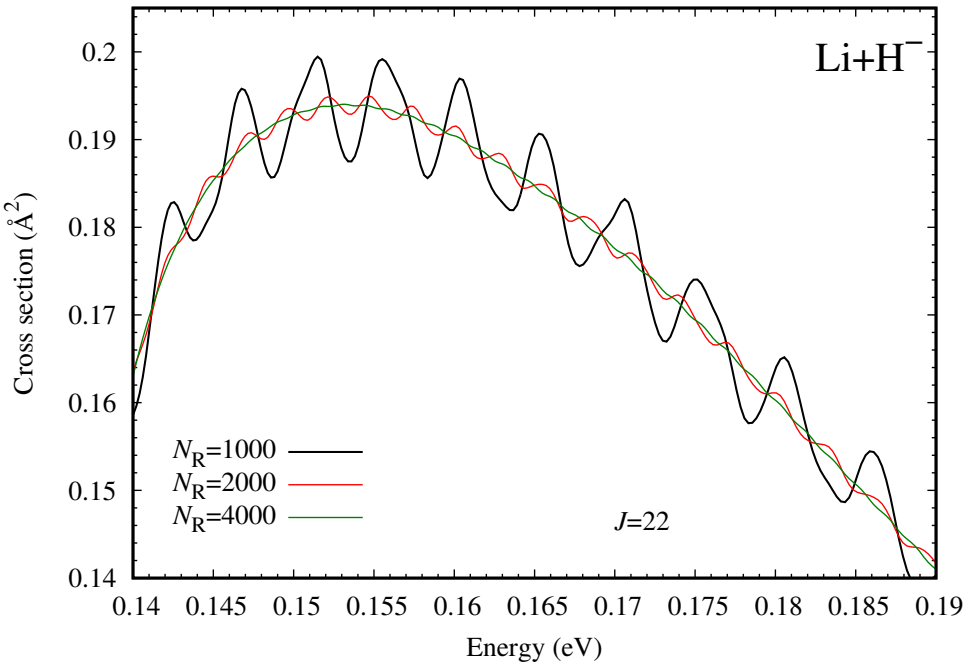

Figure 4.12: The AD cross section of the Li+H$^-$ collision for the partial wave $J = 22$ calculated with various numbers of mesh points in the energy region above the second Wigner cusp.

4.5 Test of physical parameters

The choice of the discrete state is arbitrary to a certain extent. In theory, various nonlocal models are consistent since the change in the discrete state is compensated with the corresponding change of the level-shift function or rather the change of the Hermitian part of the nonlocal potential. In practise, the model is often not constructed by the projection-operator approach but rather from *ab initio* data, and thus, the consistency does not have to be preserved. Here, we test this arbitrariness in the choice of the discrete state by presenting two additional nonlocal resonant models, which give the very similar eigenphase sum as the original model constructed in Section 2.6, but the shapes of the discrete-state potential $V_{\mathrm{d}}(R)$ sufficiently differ.

We describe the appearance of the unexpected resonances in the eigenphase sum and their behaviour with variations of the parameter $a(R)$ in Section 2.6. The modifications of the model concern especially the parameter $a(R)$. We decrease its magnitude as much as possible in order to avoid the appearance of the resonances at energies below 1 eV. To achieve even the lower value of $a(R)$ without the resonances below 1 eV, we modified the threshold exponent $\alpha(R)$ in one of the models as well (Table 4.6). We refer to these three nonlocal models by the designations NRM1, NRM2 and NRM3. The NRM1 denotes the original model.

Table 4.6: The parameters $a(R)$ and $\alpha(R)$ of the original (NRM1) and two additional (NRM2 and NRM3) nonlocal resonant models of the Li+H$^-$ collision.

model	$a(R)$	$\alpha(R)$
NRM1	$3.0\exp(-0.025R^2)$	0.10
NRM2	$2.0\exp(-0.025R^2)$	0.10
NRM3	$1.8\exp(-0.025R^2)$	0.05

The significant change in the eigenphase sum of the models NRM2 and NRM3 is the shift of the resonances towards lower energies. The differences in the shape at energies below 1 eV are minor (Figure 4.13). The modification of the original model have also influence on the shape of the discrete-state potential (Figure 4.14).

We separated the coupling potentials $V_{\mathrm{d}\epsilon}(R)$ of the additional models as described in Section 4.2. In fact, we only manually changed the parameter α_1 in the first separable term in the case of the NRM3. Then, the fitting procedure provided reasonable separations. We also verified that the convergence of the separable expansion is preserved. To shorten computational times we reduce the number of mesh points to $N_{\mathrm{R}} = 4000$ and we calculated cross sections only at 500 logarithmically-distributed energies compared to the original 1000 energies. The choice of $N_{\mathrm{R}} = 4000$ is well justifiable since the relative error of the cross section $J = 22$ with $N_{\mathrm{R}} = 6000$ and 4000 is at most 1 %. The other parameters were chosen as before, see Table 4.2.

The resulting total AD cross sections differ minimally, which can be seen in Figure 4.15, where the results are shown up to 50 meV, or rather in Figure 4.16, where we depict the more detailed comparison at very low energies. The relative

difference between the NRM1 and NRM2 is about 2 %, between the NRM1 and NRM3 is less than 1 %. The differences may be mostly caused by the choice of fewer mesh points. The lesser energy resolution may be responsible for differences in positions of the orbital resonances. To describe the resonance well, we should calculate the cross sections at more energies, but it would significantly increase computational time.[7]

Furthermore, we compared individual partial waves. There is no distinct difference between their shapes even at low energies. Such difference would not be reflected in the total cross section.

The good agreement of the results for all proposed models indicates that the descriptions within the nonlocal theory with different discrete states are equivalent in this case.

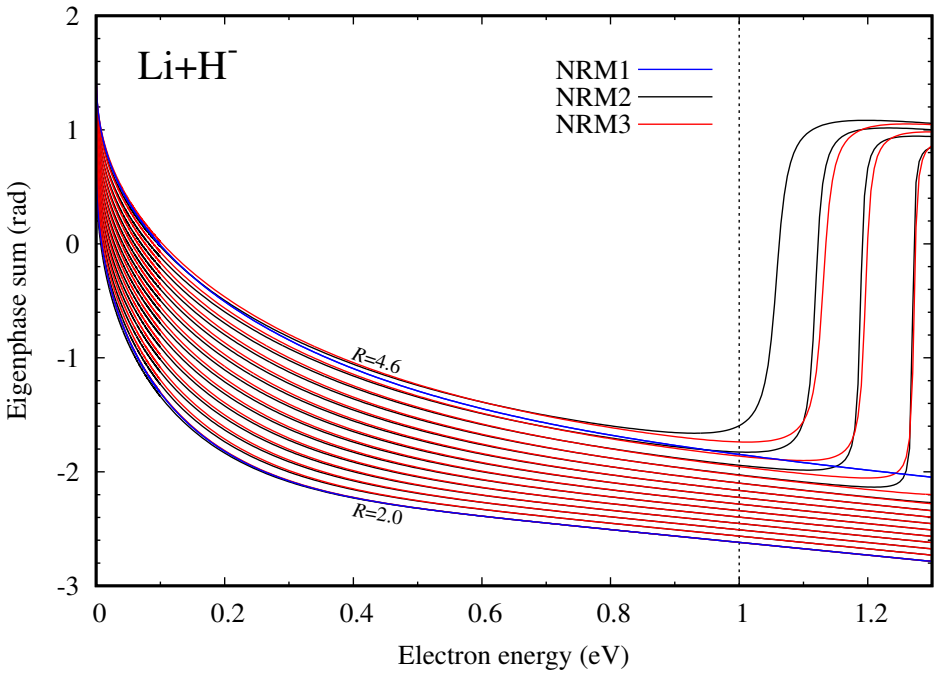

Figure 4.13: The comparison of the eigenphase sum determined from the three nonlocal resonant models NRM1, NRM2, and NRM3 of the Li+H$^-$ collision at 14 values of internuclear distance ($R = 2.0$ to 4.6 with step 0.2 from bottom to top). For clarity, only the most bottom and most top curves are shown in the case of the original model NRM1. The difference of the other curves is similar to the difference between NRM2 and NRM3.

[7] In fact, the computational time does not depend linearly on the number of energies owing to the use of the logarithmic distribution. More data points are located in the low-energy region, where calculations typically require fewer iterations of the Schwinger-Lanczos algorithm.

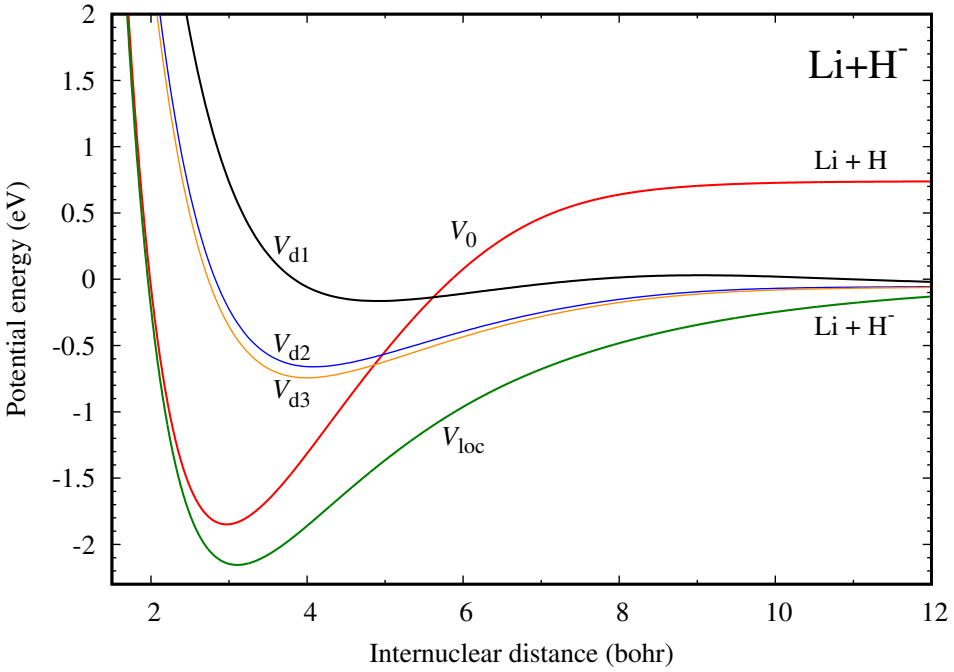

Figure 4.14: The discrete-state potentials of the nonlocal resonant models NRM1 (original model), NRM2, and NRM3 of the Li+H$^-$ collision designated by V_{d1}, V_{d2}, and V_{d3} respectively together with the neutral potential V_0 and the local anion potential V_{loc}.

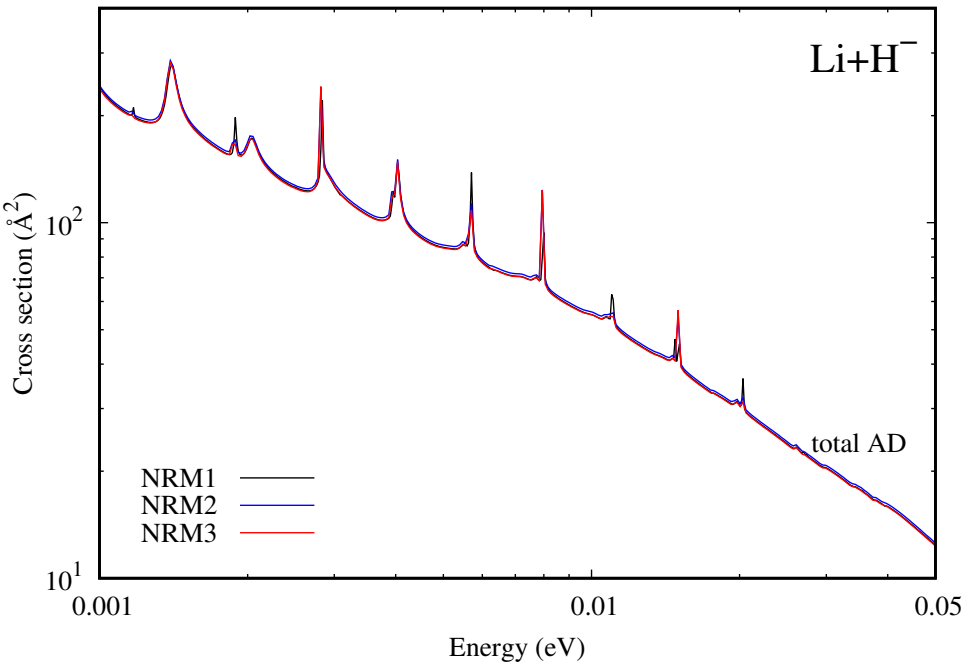

Figure 4.15: The comparison of the total AD cross sections of the Li+H$^-$ collision calculated from the nonlocal resonant models NRM1 (original model), NRM2, and NRM3 in the logarithmic scale.

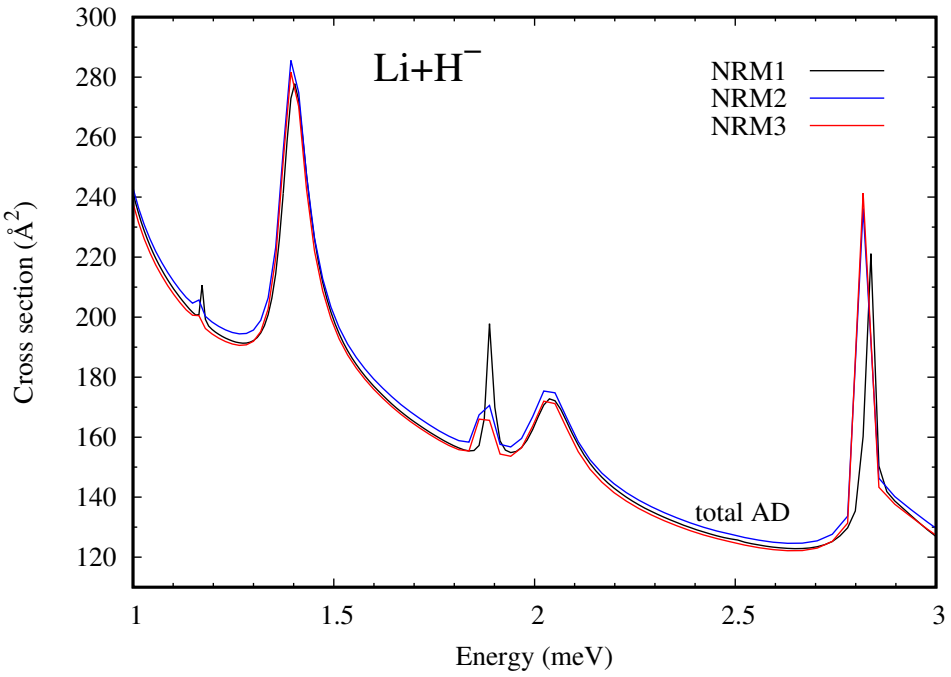

Figure 4.16: The detailed comparison of the total AD cross sections of the $Li+H^-$ collision calculated from the nonlocal resonant models NRM1 (original model), NRM2, and NRM3.

4.6 Rate constant

In the last section of the fourth chapter, we discuss the AD rate constant of the $Li+H^-$ collision calculated by Formula (1.68). Sharp peaks, which originate from orbital resonances, appear in the total AD cross section. The precise integration of a function with sharp peaks may be problematic because their description is limited due to a relatively small energy resolution. The peaks do not appear to be so high, see Figure 4.17, where we show the integrand of the rate constant integral including all constants. There is a possibility that we miss the real maxima of the peaks, and thus, they may be significantly higher. To get an idea about the contribution of the peaks to the integral, we computed the approximate area of the peaks. We use the trapezoidal rule on the non-equidistant grid to calculate the result. We determined the contribution of the peaks as the difference of the whole area beneath the integrand (beneath the red curve in Figure 4.18) and the area without the peaks (beneath the green curve). The relative areas of the peaks determined by trapezoids with respect to the whole integral are about 1.2 % and 0.8 % at temperatures $T = 100$ K and 200 K respectively.

The real area may differ but we assume that the difference is not by several orders of magnitude. The assumption is made up from the analysis of one particular peak. We recalculated the orbital resonance appearing in the partial wave $J = 30$, which is responsible for the peak in the left-hand side of Figure 4.18, at more energies to determine the precise height (Figure 4.19). The difference of the height of the last calculation and the original result is insignificant, it is about 5 %.

We conclude the discussion about the integration by saying that the area of

the peaks is probably slightly larger, but still the original energy resolution is large enough to describe the peaks with the maximal relative error about tens of percent. Thus, we assume that the contribution of the peaks to the result is not substantial.

Finally, we calculated the temperature-dependent rate constants for all three nonlocal models (Figure 4.20). The results for the NRM1 and NRM2 are almost indistinguishable in the used scale because the relative errors are the same as the errors of the total cross sections, see Section 4.5. The determination of the rate constant is restricted by the interval [0.001,1] eV, where the cross sections were calculated. The part of the integrand located above 1 eV starts to significantly contribute to the result at temperatures $T \geq 1500$ K. On the other hand, there is a problem with the divergence of the total AD cross section at zero energy at very low temperatures. Extrapolation of the total cross section beyond the energy interval can be used, but we will not deal with it any longer.[8]

The temperature-independent rate constant of the Li+H$^-$ collision was estimated by Stancil et al. [14] as 4×10^{-10} cm^{3}s^{-1}. The estimation was based on associative detachment processes of Na$^-$ and K$^-$ ions with hydrogen atom experimentally investigated by Fedchak et al. [40]. Our temperature-dependent result is smaller but of the same order of magnitude at temperatures up to 1000 K.

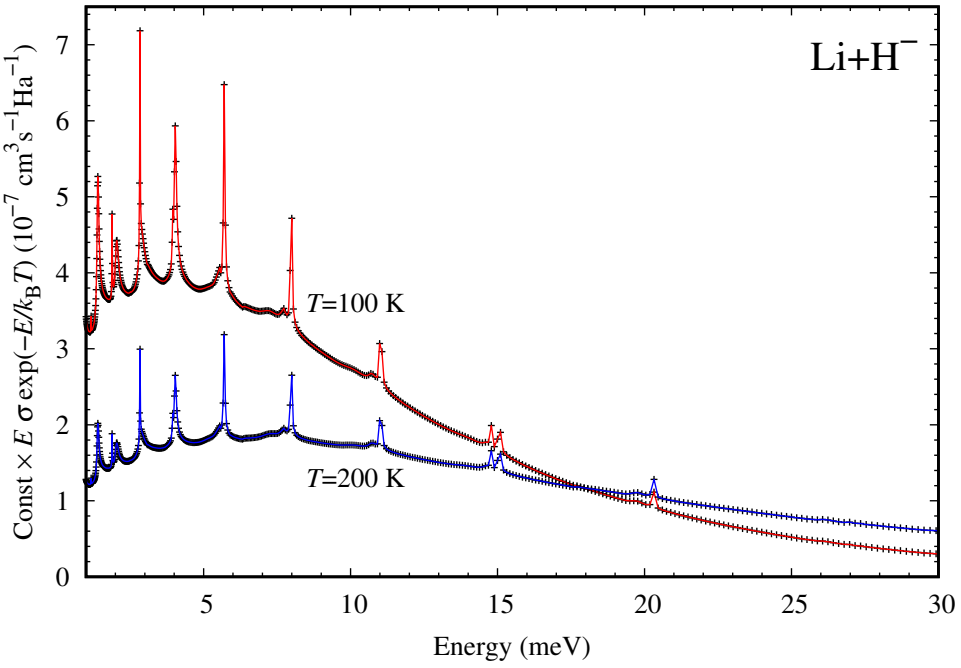

Figure 4.17: The integrand of the rate constant integral of the Li+H$^-$ collision at the temperatures $T = 100$ K and 200 K (red and blue curves respectively). Data points are denoted by crosses.

[8]The more detailed analysis of the rate constant at low and high temperatures should be done before we publish the results. However, the publication should be preceded by the clarification of the uncertainties in the scattering data.

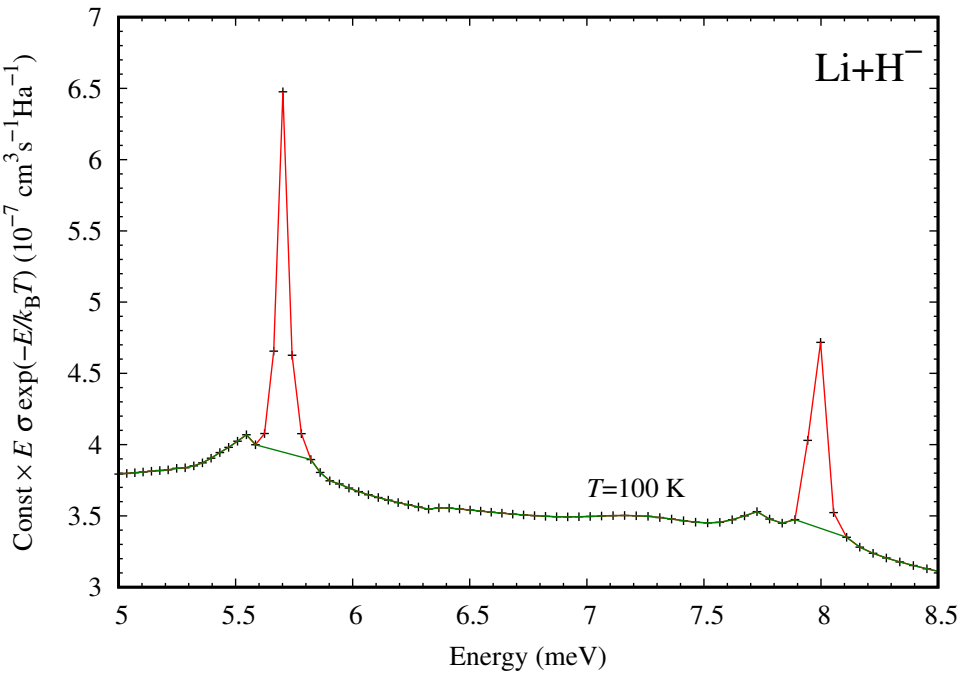

Figure 4.18: The illustration of the approximate area of the peaks in the integrand of the rate constant of the Li+H$^-$ collision determined as the difference of the areas beneath the red and green curves respectively. Data points are denoted by crosses.

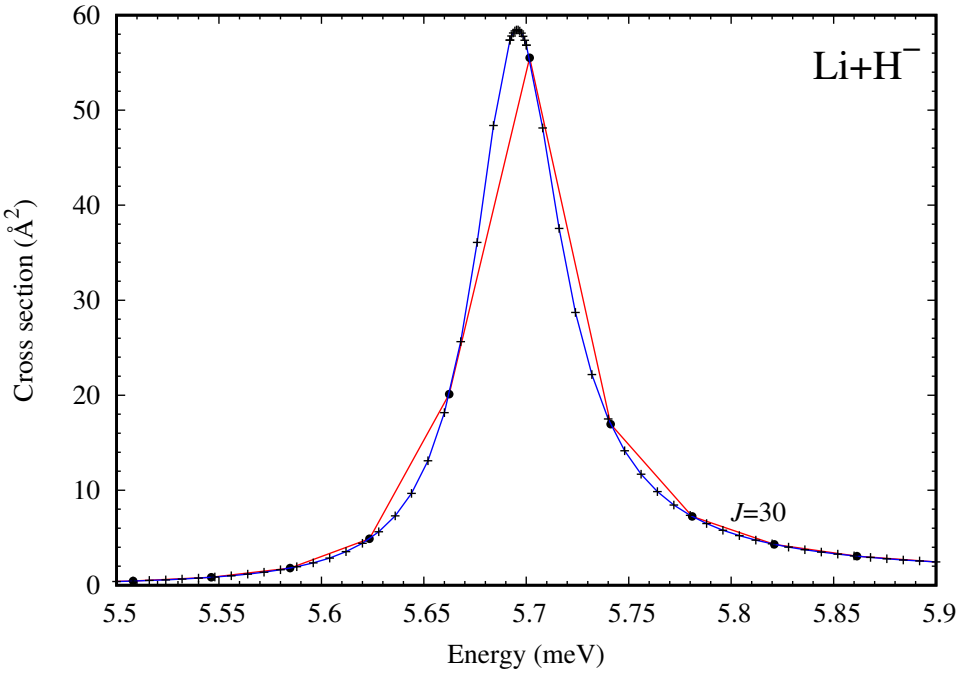

Figure 4.19: The detailed description of the orbital resonance in the partial wave $J = 30$ of the Li+H$^-$ collision, full circles and the red curve denote the original calculation, crosses and the blue curve designate the calculation with a better energy resolution.

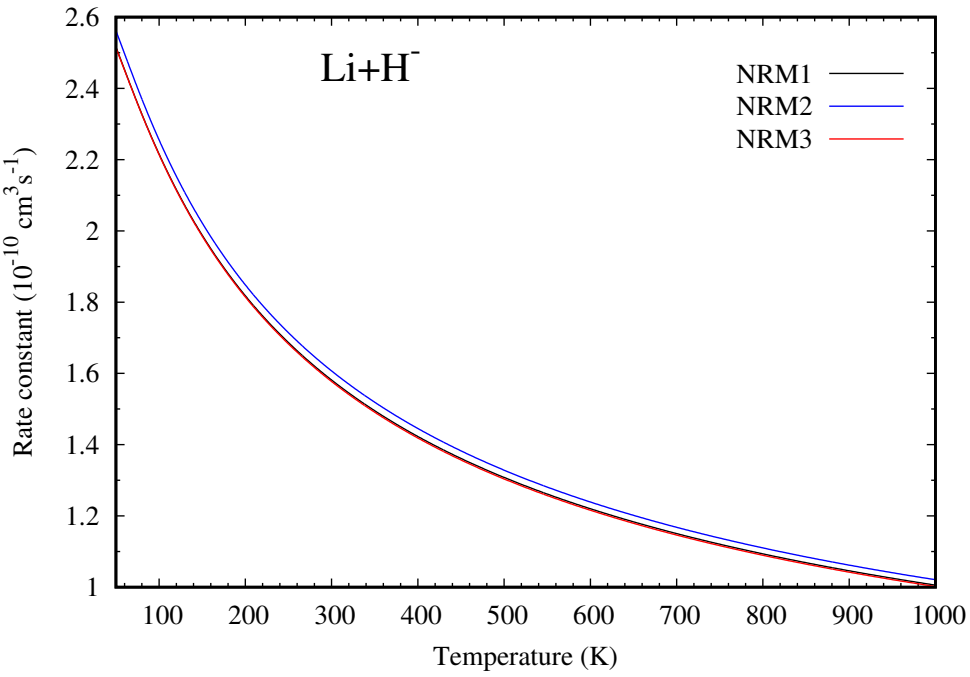

Figure 4.20: The temperature-dependent rate constant of the Li+H$^-$ collision calculated for all three nonlocal models NRM1, NRM2, and NRM3.

5. Li^-+H collision

5.1 Introduction

In the last chapter of this thesis, we focus on the detailed description of the second studied process, Li^-+H collision (2.2). We start again with the separation of the discrete-state-continuum-coupling potential. Then, we discuss AD cross sections and the choice of optimal numerical parameters. We propose three new nonlocal models to test the extrapolation in the vicinity of the crossing. We also compare the nonlocal results with the local approximation, which can be computed in this case. In the end, we present rate constants determined from both nonlocal and local results.

5.2 Coupling separation

It turned out that the proposed separation method does not work very well in this case. The sum of separable terms does not converge fast enough. Here, we explain the probable source of the failure of this procedure.

We separated the coupling potential using the SVD method on energy and space grids as in the previous process. The energy grid was chosen as [0.1,100] eV. We fitted the first ten SVD energy functions f_k, see Table 5.1, where the resulting parameters α_k, b_k, N_k together with the singular values σ_k are listed. The polynomials of the functions $k = 5, \ldots, 10$ have the same degree $N_k = 13$. The restriction of the polynomial degree is caused by rounding errors. These errors appear in the calculation of the Hermitian part of the nonlocal potential for $N_k > 13$ at some energies, which is described in more detail in Section 4.2. The reached precision of the fit $k = 1, \ldots, 4$ is comparable with the precision of the fit for the Li+H^- collision. The fits of $k = 6, \ldots, 10$ are not so precise, see below, because of the numerical limitations of the polynomial degree.

Table 5.1: Parameters of the fitted SVD energy functions $\tilde{f}_k$ with $k = 1, \ldots, 10$ for the Li^-+H collision.

k	N_k	α_k	b_k	σ_k
1	1	0.226	3.0	155.20
2	7	0.020	8.4	9.15
3	9	0.005	10.1	2.71
4	11	0.200	17.8	1.12
5	13	0.200	20.2	0.47
6	13	0.200	21.5	0.19
7	13	0.010	47.7	0.09
8	13	0.010	43.8	0.05
9	13	0.010	47.7	0.02
10	13	0.010	50.1	0.01

We found out that the cross sections do not convergence fast enough with the increasing number of separable terms (Figure 5.1). Even with the most considered separable terms ($N_c = 10$), the resulting cross section still significantly differs from the result calculated with the non-separated coupling potential (top black curve). We give more details about calculations without a separable approximation later.

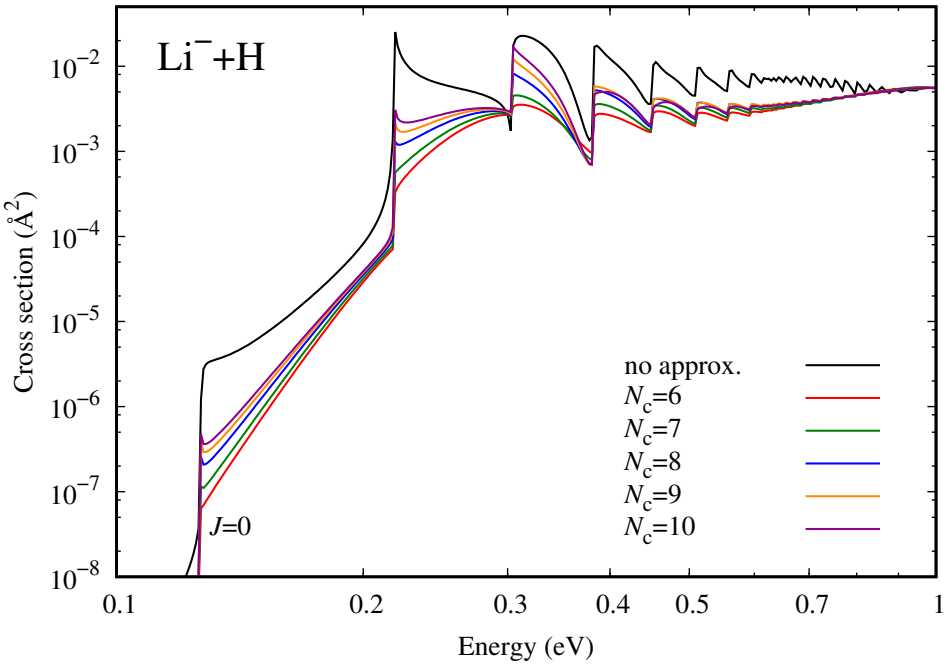

Figure 5.1: The non-convergence of the cross section of the Li^-+H collision for the partial wave $J = 0$ with the increasing number of separable terms $N_c = 6, \ldots, 10$ compared to the same cross section computed without any separable approximation (top black curve) in the logarithmic scale.

One possibility, which may cause the convergence problem, is that the approximation converges very slowly with the increasing number of terms, and we are just not able to reasonably fit more separable terms. This conjecture is based on the comparison of convergence speeds of SVD expansions. The first six singular values descend to zero as fast as in both of the previous cases, compare the last columns of Tables 3.1, 4.1 and 5.1. But then, the convergence is slowed down. In the Li+H^- and Br^-+H collisions, the tenth and fifteenth singular values are in the order of 10^{-3} and 10^{-6} respectively while they are only in the order of 10^{-1} and 10^{-3} respectively in the Li^-+H channel.

However, we are not convinced that the slow SVD convergence is the main reason of the failure of the separation method. We assume that the insufficiently precise description of the low-energy behaviour of the functions f_k is mostly responsible for it. Positions of resonances in the eigenphase sum are well described by the separable approximation (Figure 5.2), but the difference in the low-energy region is apparent, especially at internuclear distances close to the crossing (Figure 5.3). The presented curves were calculated with six separable terms. The agreement at low energies is not considerably improved with more terms. The various approximations of the cross section $J = 0$ most differ at vibrational

thresholds, see again Figure 5.1. The difference reduces with increasing energy to the point where the next vibrational threshold appears. This behaviour indicates that the low-energy description causes the disagreement in the cross sections.

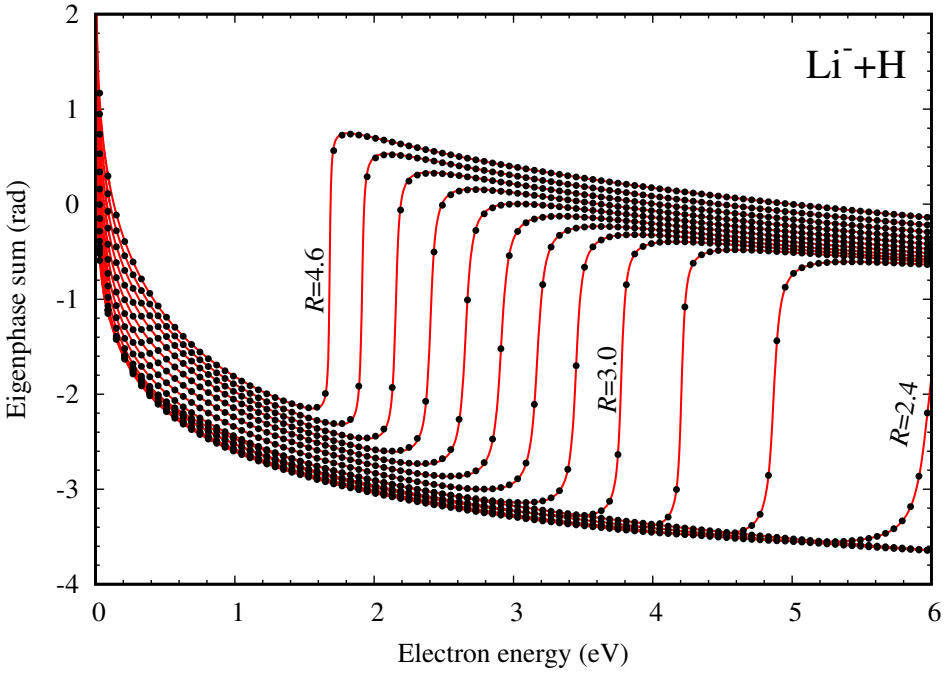

Figure 5.2: The comparison of the eigenphase sum of the Li^-+H collision constructed directly from the nonlocal model (red curves) with the eigenphase sum computed from the separated coupling potential with six terms (dots) at 14 values of the internuclear distance ($R = 2.0$ to 4.6 with step 0.2 from right to left).

The low-energy behaviour of the functions f_k is poorly recognizable for $k \geq 3$ even if the lower endpoint of the energy grid is fairly low (10^{-6} eV or lower). Thus, the manual fit of the parameter α_k misrepresents the proper shape (Figure 5.4). The first two fits ($k = 1, 2$) describe well the low-energy behaviour. In the third term, the slight disagreement appears at the lowest energies. The fits $k \geq 4$ describe the behaviour very roughly. It seems that the functions f_k diverge at zero energy for some k, but the choice of negative values of α_k did not solve the convergence problem. The functions rapidly change in a small low-energy region, which is difficult to describe and it causes the large magnitude of the polynomial coefficients, which implies a strong exponential decay. We also encounter this polynomial behaviour in the Li+H^- channel, see Section (4.2). The cross sections are also fairly sensitive to the magnitude of the parameters α_k, especially in the vicinity of vibrational thresholds.

The source of the low-energy behaviour is probably encoded in the nonlocal model and it may have a connection with the supercriticality of the dipole moment of LiH. We suspected that the local minimum in the parameter $a(R)$ given by Formula (2.18) caused the problems, but the non-convergence persists even if we replace $a(R)$ with a similar monotonous function. We did not encounter similar difficulties in the previous processes. The low-energy behaviour is quite apparent and reasonably well approximated by manual fitting.

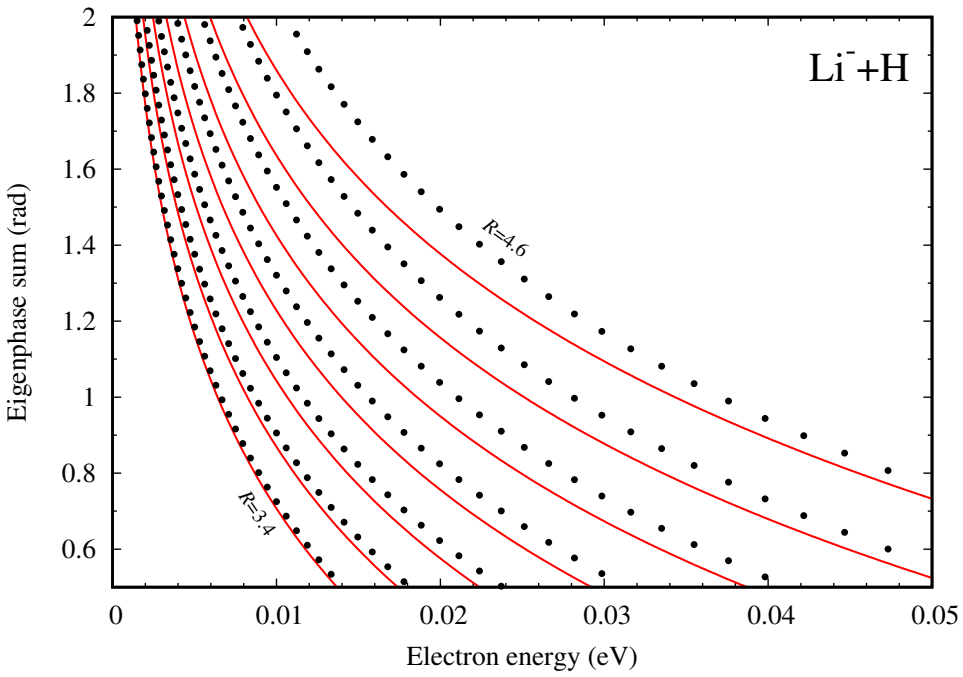

Figure 5.3: The low-energy detail of the comparison of the eigenphase sum of the Li^-+H collision constructed directly from the nonlocal model (red curves) with the eigenphase sum computed from the separated coupling potential with six terms (dots) at 7 values of the internuclear distance ($R = 3.4$ to 4.6 with step 0.2 from left to right).

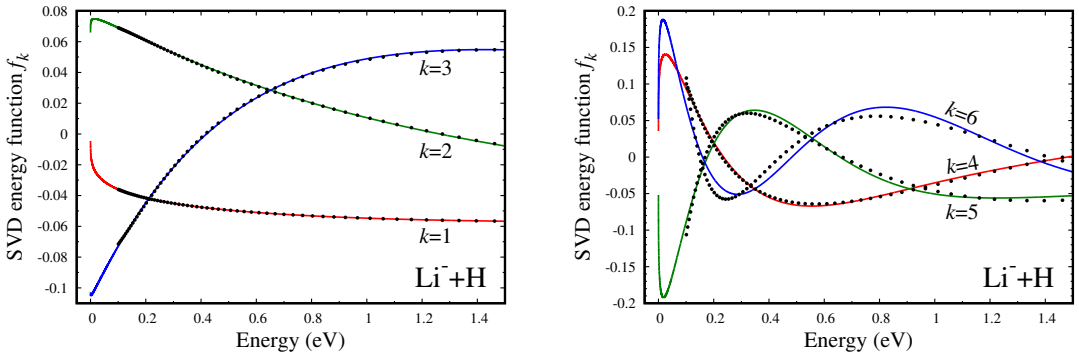

Figure 5.4: The illustration of the low-energy behaviour of the SVD energy functions f_k of the Li^-+H collision (dots) compared with the fitted functions $\tilde{f}_k$(curves) for $k = 1, 2, 3$ (left) and $k = 4, 5, 6$ (right).

Another indication of the non-correct separation of $V_{d\epsilon}(R)$ is the comparison of two formulas for AD cross sections. The coupling potential was approximated by the separable expansion with $N_c = 10$, and then, we calculated the AD cross section $J = 0$ from the T-matrix by Formula (1.51) and as the sum of individual vibrational contributions by Formula (1.52). The second result differs less from the cross section calculated without any $V_{d\epsilon}(R)$ approximation (Figure 5.5). Our explanation of this phenomenon is the following. If we determine the cross section from the T-matrix, we use only the separable expansion of $V_{d\epsilon}(R)$. In the second case, the wave function $\psi_J(R)$ is also computed from the separation form, but

the matrix element $\langle\chi_{\nu J}|V_{\mathrm{d}k_\nu}|\psi_J\rangle$ is obtained from the non-separated $V_{\mathrm{d}\epsilon}(R)$, which seems to partly compensate the inaccuracy of the separation. We remark that both the formulas give the same results in the Li+H$^-$ collision except the numerical instabilities of the formula which uses the T-matrix.

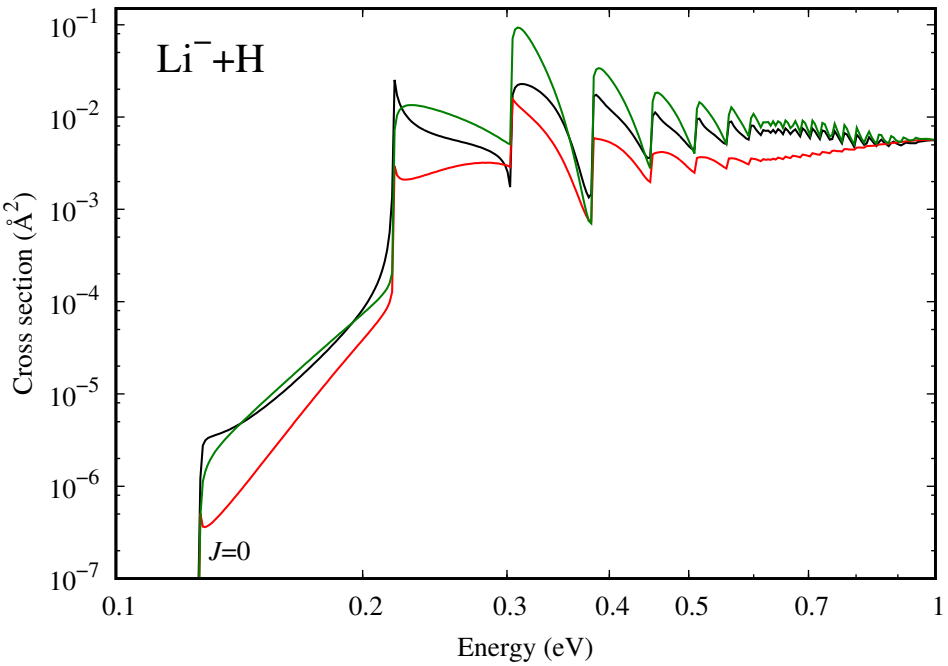

Figure 5.5: The comparsion of the cross section of the Li$^-$+H collision for the partial wave $J = 0$ determined from the T-matrix (red), from the sum of individual vibrational contributions (green) and without any separable approximation (black). The coupling potential was approximated by ten separable terms in the first two cases.

The conclusion of the above discussion is that the separation method with the proposed fitting procedure can not be used in the case of the Li$^-$+H collision. One possibility is to enhance the fitting procedure, a full non-linear fit might provide better results, or abandon the method and use another approach, for example the mentioned Bateman approximation [33, 34]. We decided to use the most straightforward but not effective approach, that is we do not approximate the coupling potential at all.

The nonlocal potential is given by the expansion over vibrational states by Formula (1.46). The calculation of the anti-Hermitian part is simple. We just substitute particular values of R and R' into the definition by Formula (1.47). The evaluation of the Hermitian part is little more complicated. The Hermitian component is equal to

$$\Delta_J(E,R,R') = \sum_\nu \chi_{\nu J}(R)\Delta(E-E_{\nu J},R,R')\chi_{\nu J}(R'), \tag{5.1}$$

where

$$\Delta(E-E_{\nu J},R,R') = \mathrm{p.v.}\int \mathrm{d}\epsilon \frac{V_{\mathrm{d}\epsilon}(R)V_{\mathrm{d}\epsilon}(R')}{E-E_{\nu J}-\epsilon}. \tag{5.2}$$

The coupling potential is given from the width function by Formula (3.8). We substitute this expression into the last integral and we introduce the notation $a = a(R)$, $a' = a(R')$, $b = b(R)$, $b' = b(R')$, $\alpha = \alpha(R)$, $\alpha' = \alpha(R')$, and $B = (1/b + 1/b')/2$. Then, the Hermitian part can be calculated using

$$\Delta(E - E_{\nu J}, R, R') = \frac{1}{2\pi}\sqrt{\frac{aa'}{b^{\alpha}b'^{\alpha'}}}B^{-(\alpha+\alpha')/2}\mathrm{Del}\left[B(E - E_{\nu J}), (\alpha + \alpha')/2\right], \quad (5.3)$$

where the analytic formula for integral $\mathrm{Del}(E, \alpha)$ (3.11) is used.

The direct calculation of the nonlocal potential is not very effective but it is manageable in this case. In fact, we see later that the calculation of cross sections takes less time than it is in the Li+H^- collision, where the separable approximation is used.

5.3 AD cross sections

Here, we present the AD cross sections of the Li^-+H channel calculated with the optimal values of numerical parameters (Table 5.2). The choice of these parameters is described in the next section.

Table 5.2: The optimal numerical parameters of nonlocal calculations for the Li^-+H collision.

parameter	partial waves J
$R_{\mathrm{min}} = 0.01$	$0, \ldots, 35$
$R_{\mathrm{min}} = 0.05$	$36, \ldots, 48$
$R_{\mathrm{min}} = 0.10$	$49, \ldots, 60$
$R_{\mathrm{max}} = 10$	all
$R_{\mathrm{DVR}} = 20$	all
$N_{\mathrm{R}} = 800$	all
$N_{\mathrm{v}} = 60$	all

We calculated the AD cross sections of the Li^-+H collision for the partial waves $J = 0, \ldots, 60$, see Figures 5.6 and 5.7, where the partial waves $J = 0, \ldots, 10$ and $J = 0, 20, 30, \ldots, 50, 60$ are shown respectively in the logarithmic scale. In addition, the total AD cross section (green) obtained as the sum of all computed partial contributions is depicted in both of the figures as well.

We note that the results do not have to be valid at energies above the dissociation limit, where the dissociation channel, which is given by Equation 4.2 but with Li^-+H on the left-hand side, is not considered. The dissociation threshold is determined by the electron affinity of lithium atom EA(Li)=0.62 eV in this case obtained from the MOLPRO calculations, see Section 2.2.3.

There is a distinct difference in the shapes of the presented results when we compare them to the AD cross sections of the Li+H^- channel, see Figures 4.4 and 4.5. Here, all partial waves rapidly grow with increasing energy at first. Then, some kind of saturation occurs, that is the cross sections does not increase anymore, they are nearly constant. The overall shape is again closely related to the behaviour of the local anion potential (the potential of the $A^2\Sigma^+$ state) or

rather the potential of the discrete state in this case, which is repulsive at all internuclear distances, see again Figure 2.7.

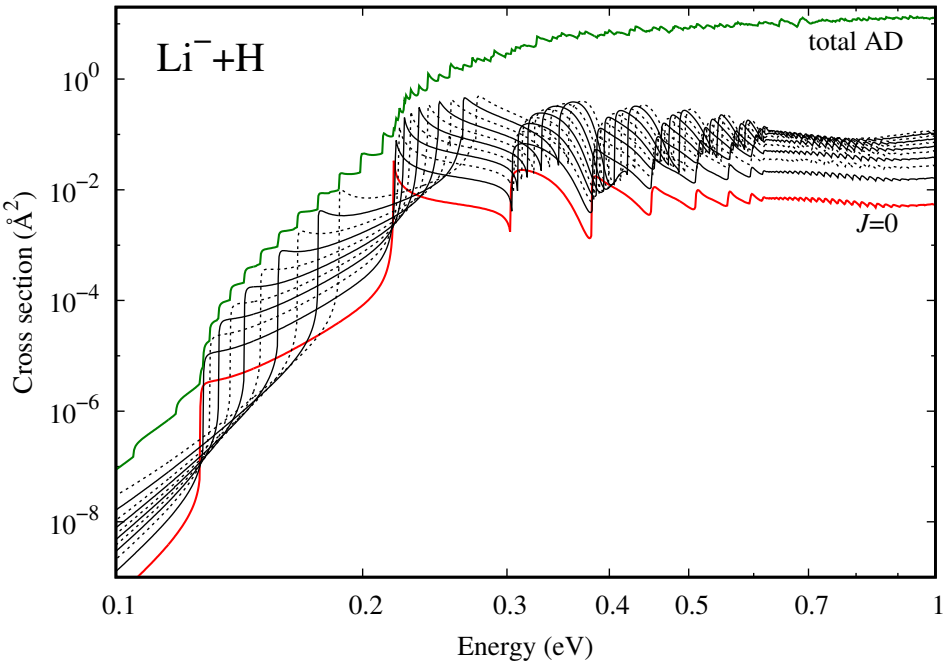

Figure 5.6: The AD cross sections of the Li^-+H collision for the partial waves $J = 0, \ldots, 10$ (from bottom to top, each other curve is dashed, $J = 0$ red) together with the total AD cross section (green) in the logarithmic scale.

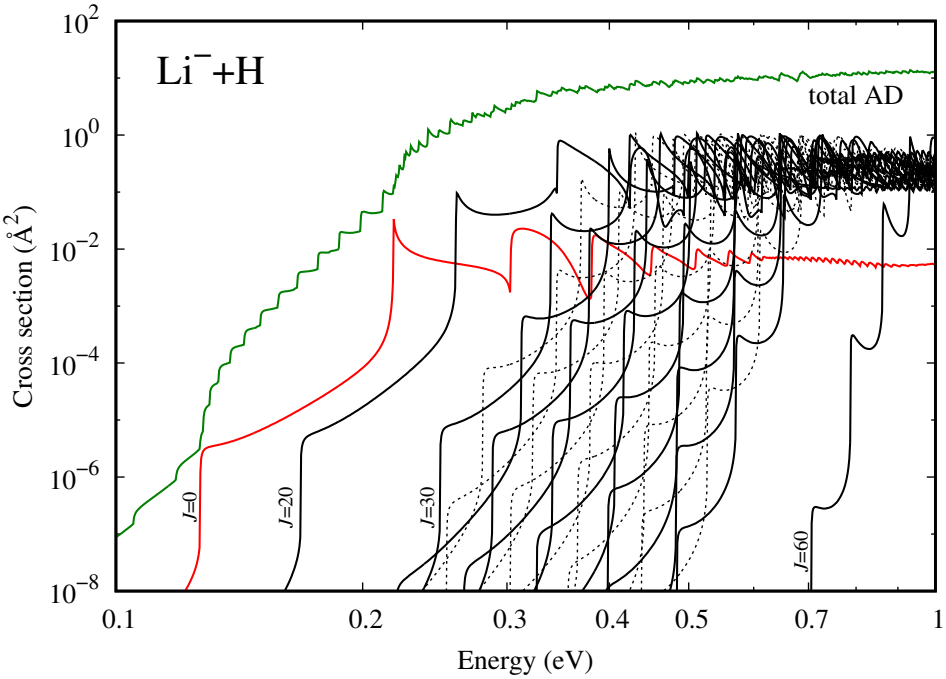

Figure 5.7: The AD cross sections of the Li^-+H collision for the partial waves $J = 0, 20, 60$ and $J = 30, 31, \ldots, 49, 50$ (from left to right, $J = 0$ red, each other curve is dashed starting $J = 31$) together with the total AD cross sections (green) in the logarithmic scale.

Zero energy, from which the collision energy is measured, is fixed by the asymptote of the discrete-state potential as $R \to \infty$. The electron detachment may occur if the ingoing particle reaches the region near the crossing point $R_c = 6.7$, where the coupling is located, see Figure 5.8. At energies below the energy of the crossing point $E_c = V_d(R_c) = 0.26$ eV, the quantum tunnel effect is not very effective, and thus, the cross sections are suppressed at these energies. The tunnel effect becomes more effective with increasing energy, which explains the rapid growth of the cross sections. If the collision energy is higher than the crossing energy ($E > E_c$), every ingoing particle reaches the inner region. Then, the occurrence of the electron detachment depends on the particular shape and magnitude of the coupling potential. Therefore, the cross sections are saturated at high energies. The energy of the crossing point rises with increasing J according to the formula

$$E_c^{(J)} = E_c + \frac{J(J+1)}{2\mu R_c^2}, \tag{5.4}$$

but the position of the crossing point remains the same because the neutral potential is modified by the centrifugal term as well. Thus, the initial growth is shifted to higher energies for higher partial waves.

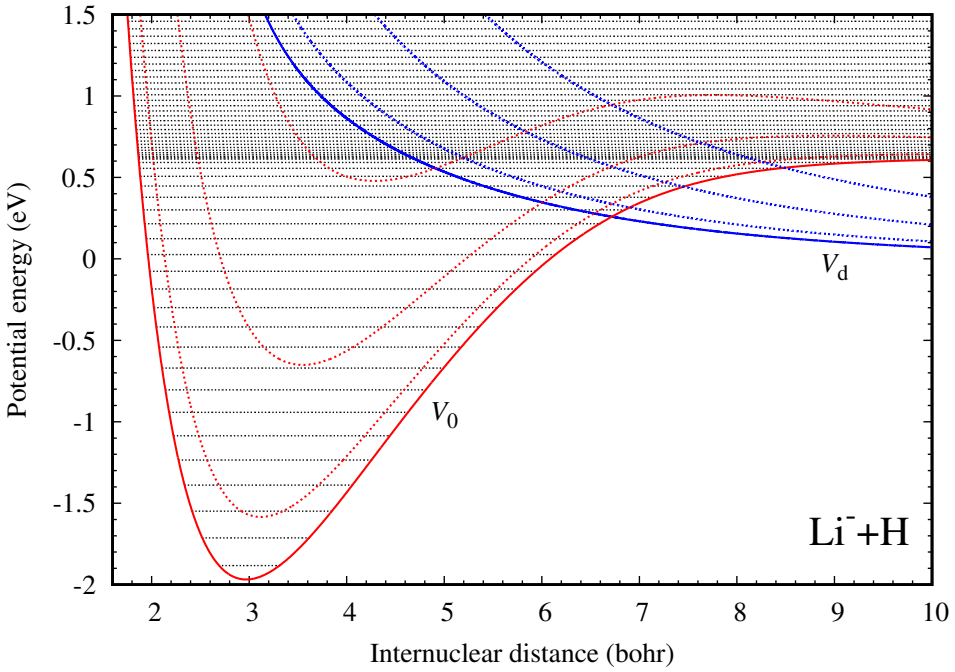

Figure 5.8: The effective neutral and discrete-state potentials of the Li^-+H collision for $J = 0, 20, 40, 60$ (red and blue curves from bottom to top respectively). Horizontal dashed lines denote vibrational levels including the discretized continuum in the neutral potential ($J = 0$).

Orbital resonances can not be observed in cross sections of the Li^-+H collision since the potential is repulsive, and therefore, a local minimum is not presented, that is no quasi-stable states with positive energies exist. On the other hand, Wigner cusps exist and the threshold behaviour is very apparent in this case. We graphically illustrate their origin in the case of the partial wave $J = 0$ in

Figure 5.9, where the left-hand part depicts the potentials in the vicinity of the crossing and the right-hand part shows the AD cross section of the partial wave $J = 0$ rotated by 90 degrees counter-clockwise.

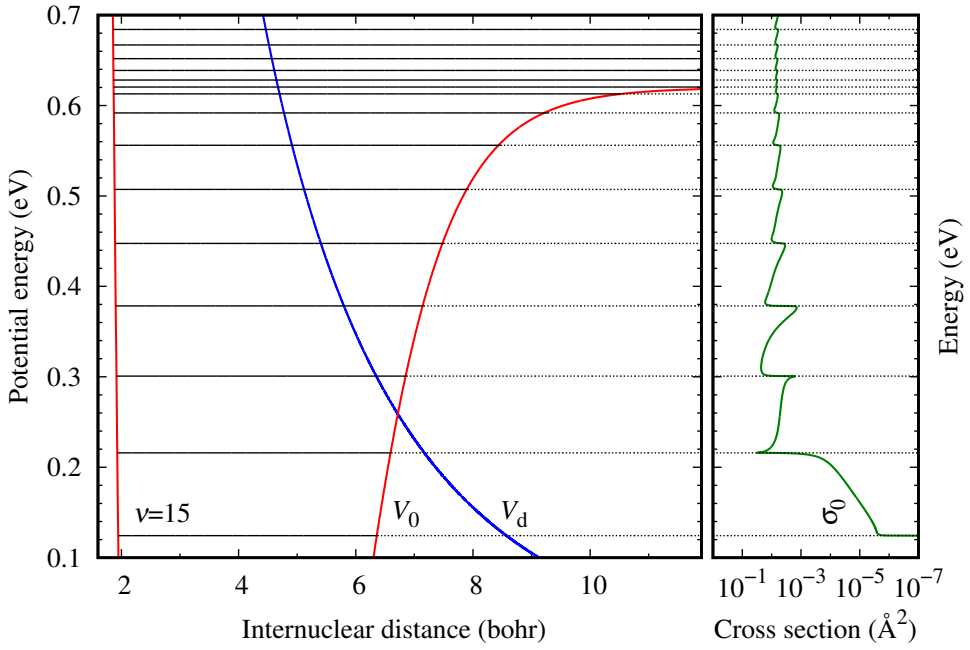

Figure 5.9: The illustration of the origin of Wigner cusps in the AD cross section of the Li^-+H collision for the partial wave $J = 0$. The left-hand figure shows the vicinity of the crossing of the neutral potential (red curve) and the discrete-state potential (blue), vibrational energies of the neutral potential are represented by solid horizontal lines. The right-hand figure depicts the cross section of the partial wave $J = 0$ (green) rotated by 90 degrees counter-clockwise. Dotted horizontal lines indicate the connection between the threshold behaviour in the cross section and the vibrational levels in the potential. The most bottom showed vibrational state is the fifteenth state designated by $\nu = 15$ (the ground state is counted as zeroth).

5.4 Numerical tests

The Schwinger-Lanczos method works very well in this case. The necessary number of iterations is about twelve iterations or less. Even five or four iterations are sufficient at very low energies ($E \leq 0.2$ eV). All presented cross sections were computed as the sum of individual vibrational contributions by Formula (1.52). Results obtained from T-matrix (1.51) agree with the other formula very well. The relative errors are in the order of 10^{-5} or less. No numerical instabilities were encountered in contrast to the previous case.

A relatively small number of mesh points and vibrational states were required (particular choices are discuss below), which speeds up the calculations compared to the Li+H^- collision (Section 4.4). However, the lack of use of $V_{d\epsilon}(R)$ separable approximation very significantly prolongs computational times. Nevertheless, the times are still shorter than in the Li+H^- calculations, see Table 5.3 and compare the results with Table 4.4. The calculations were performed with the optimal

parameters listed in Table 5.2 at 1000 energies logarithmically distributed in the interval [0.1,1.0] eV on one CPU core of a computer cluster. Higher partial waves take less time since the calculation stops if the cross section is less than 10^{-10} Å^2. The acceleration of Lanczos iterations by the preconditioning is not significant. For comparison, the calculations of the partial wave $J = 0$ with one, five and ten separable terms were performed and they took only 4 s, 37 s and 155 s respectively. Unfortunately, these results are not valid because of the non-convergence of the separable expansion. Thus, the use of some separable approximation of $V_{\mathrm{d}\epsilon}(R)$ is very desirable.

Table 5.3: Computational times of cross section calculations of the $\mathrm{Li}^- + \mathrm{H}$ collision for the partial waves $J = 0, 20, 40$ at 1000 logarithmically-distributed energies in the energy interval [0.1,1.0] eV.

J	preconditioning	no preconditioning
0	5.75 h	5.80 h
20	4.98 h	5.16 h
40	2.62 h	2.62 h

Further, we briefly discuss the sufficient number of mesh points N_{R}, the upper endpoints of the nonlocal grid $R_{\max}$ and DVR grid R_{DVR}, and the number of vibrational states N_{v}. The lower endpoint of the nonlocal grid $R_{\min}$ needs to be chosen non-zero from the same reason as before, see Section 4.4.

We found out that $R_{\max} = 10$ is the minimal size of the nonlocal grid that can be used. Only the region above the dissociation limit in the AD cross section for the partial wave $J = 0$ is sensitive to the change of R_{DVR} (Figure 5.10). It seems that the oscillations above the limit, which is denoted by the vertical dotted line, converge to a smooth curve with the increasing size of DVR grid. We selected $R_{\mathrm{DVR}} = 20$ as the optimal endpoint.

As we mention earlier, the smaller numbers of vibrational states and mesh points are sufficient. The results are converged with respect to the number of vibrational states with $N_{\mathrm{v}} = 60$ in the entire considered energy interval (Figure 5.11). The relative difference between the curves with $N_{\mathrm{R}} = 800$ and $1,500$ is less than 1 %, therefore, we use $N_{\mathrm{R}} = 800$ as the optimal number of mesh points (Figure 5.12). The chosen number of points on the grid with $R_{\max} = 10$ corresponds to the equidistant step 1.25×10^{-2}, which is smaller than the sufficient step $1/3 \times 10^{-2}$ used in calculations of cross sections of the Li+H$^-$ collision, see Section 4.4.

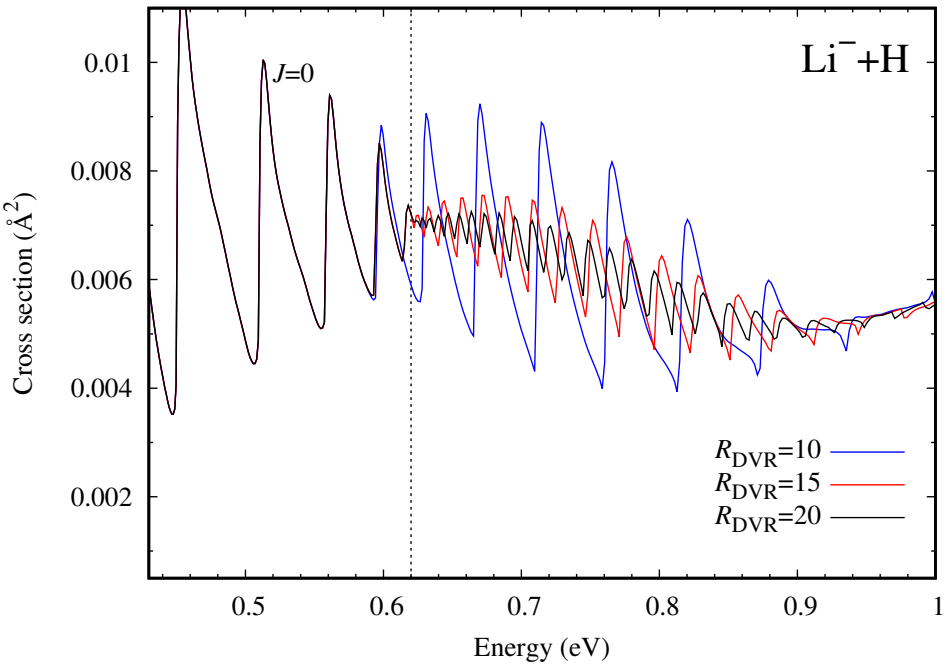

Figure 5.10: The AD cross section of the Li^-+H collision for the partial wave $J = 0$ with the upper endpoints of the nonlocal grid $R_{max} = 10$ and the DVR grid $R_{DVR} = 10, 15, 20$. The vertical dotted line denotes the dissociation limit, which is given by the electron affinity of lithium atom 0.62 eV determined from the MOLPRO calculations.

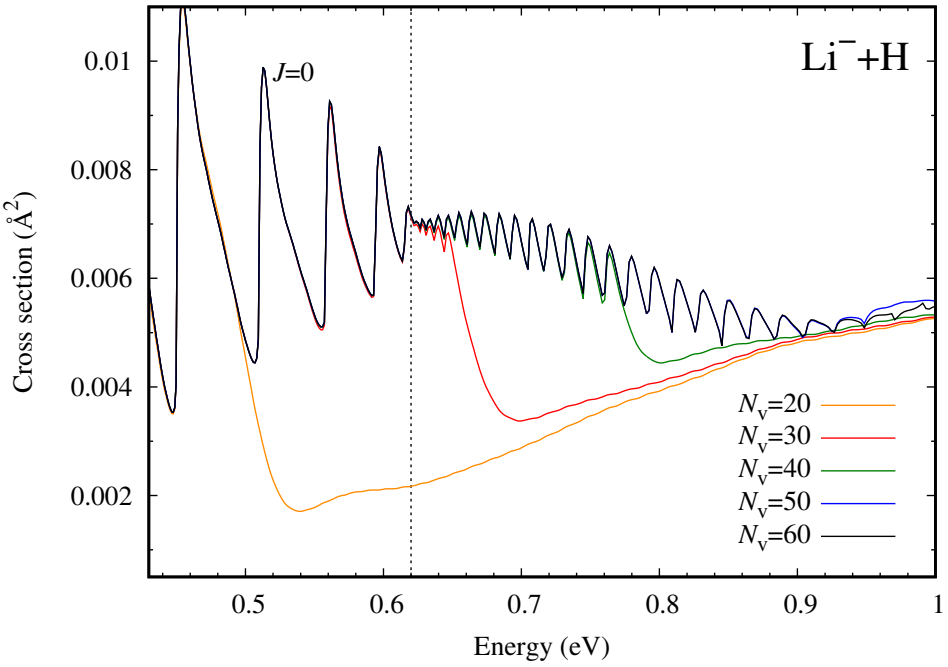

Figure 5.11: The convergence of the AD cross section of the Li^-+H collision for the partial wave $J = 0$ with the increasing number of vibrational states $N_v = 20, 30, 40, 50, 60$. The vertical dotted line denotes the dissociation limit, which is given by the electron affinity of lithium atom 0.62 eV determined from MOLPRO calculations.

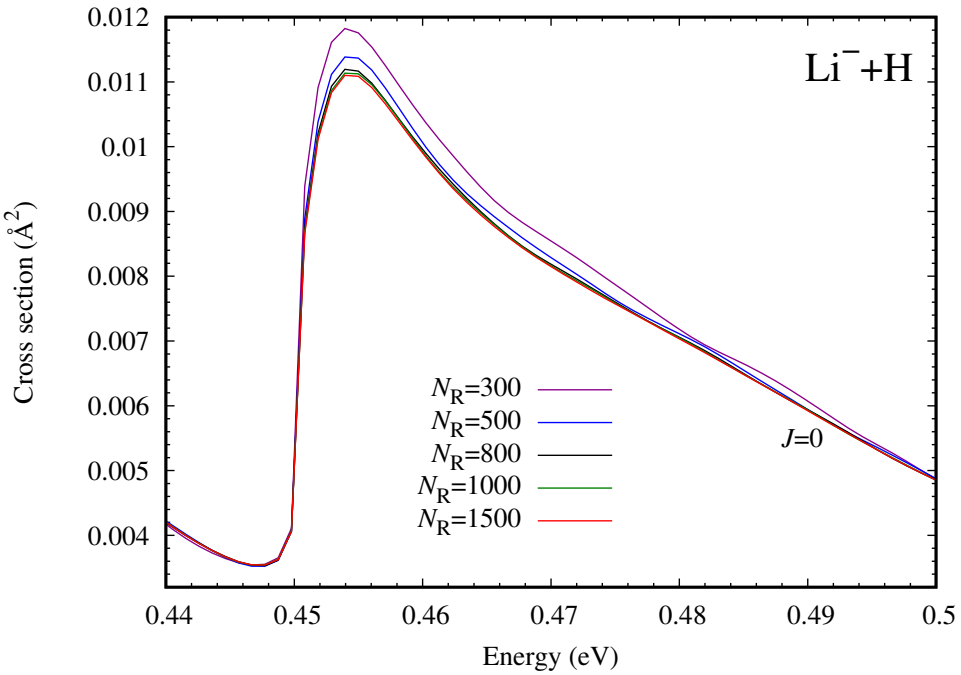

Figure 5.12: The AD cross section of the $Li^- + H$ collision for the partial wave $J = 0$ calculated with the numbers of mesh points $N_R = 300, 500, 800, 1000, 1500$. The showed region is located in the vicinity of the Wigner cusp, where the differences are the largest.

5.5 Test of physical parameters

In this section, we present three additional nonlocal resonant models. The forms of the resonance width and the background term (Formulas (2.6) and (2.15)) of the new models are preserved. We changed only the R-dependent coefficients, which were originally obtained from the interpolation of the R-dependent data by suitable functions, see Sections 2.5 and 2.7. However, the choice of these functions was quite ambiguous. In fact, the data sometimes resembled randomly distributed points without any particular trend, especially for the threshold exponent $\alpha(R)$. Therefore, we present the new models and test the sensitivity of cross sections to these modifications.

We refer to the new models as the NRM2, NRM3, and NRM4 models. The model NRM1 is the designation for the original nonlocal model presented in Section 2.7.

All coefficients of the model NRM2 differ from the original dependencies except for the parameter $a(R)$, which is the same. The coefficients, which were obtained by the fitting procedure described in Section 2.5, are given by

$$a_{\mathrm{bg}}(R) = 0.0254(R - 3.776)^4 - 0.678, \tag{5.5}$$

$$b_{\mathrm{bg}}(R) = 0.289(R - 2.956)^2 - 4.742, \tag{5.6}$$

$$a(R) = (6.093R^2 - 34.03R + 48.07)\mathrm{e}^{-1.224R}, \tag{5.7}$$

$$b(R) = 0.670\mathrm{e}^{-0.863R}, \tag{5.8}$$

$$\alpha(R) = 0.164R - 0.337. \tag{5.9}$$

The discrete-state potential was also slightly modified

$$V_{\mathrm{d}}(R) = 160.7e^{-3.169R} + 0.319\frac{1}{R}e^{-0.233R} - \frac{2.25}{[(R-14.45)^2 + 94.91]^2 + 33.18}. \tag{5.10}$$

In the remaining models, we just modified the original model by changing the threshold exponent $\alpha(R)$.

For the model NRM3, we have

$$\alpha(R) = \frac{1}{2\pi}\tan^{-1}\left[9.87(R-3.463)\right] + \frac{1}{4}, \tag{5.11}$$

and we fixed the exponent to be constant $\alpha(R) = 0.1$ in the last model NRM4.

In the case of the NRM3 and NRM4 models, the eigenphase sum only slightly differs from the original model NRM1. The eigenphase sums obtained from the models NRM1 and NRM2 differ more distinctly (Figure 5.13).

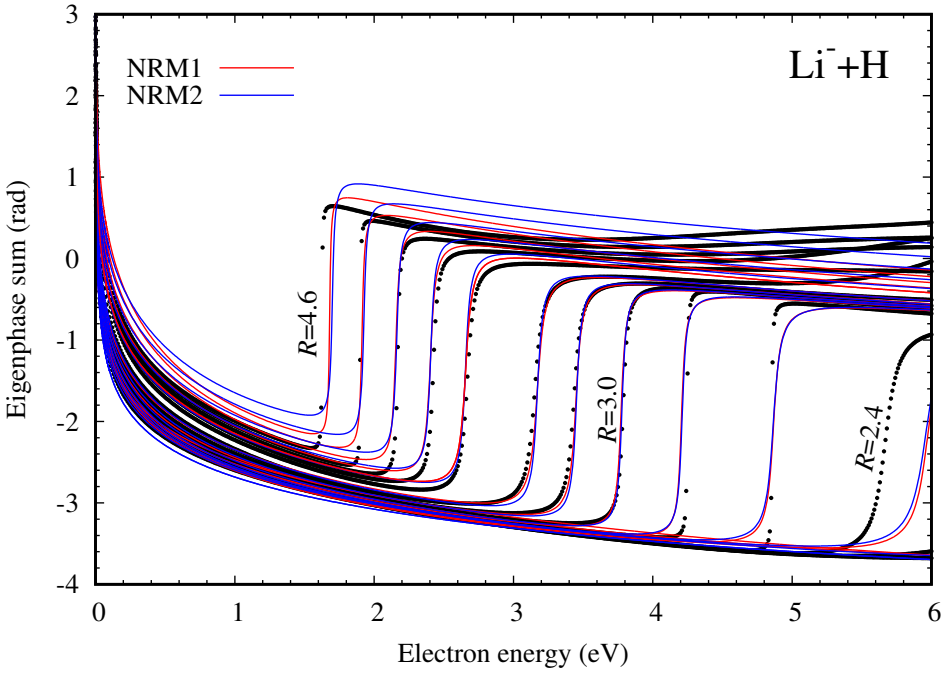

Figure 5.13: The comparison of the eigenphase sum of the Li^-+H collision obtained from the nonlocal models NRM1 (red) and NRM2 (blue) with the *ab initio* data (dots) at 13 values of the internuclear distance ($R = 2.0$ to 4.6 with step 0.2 from right to left, $R = 3.6$ is omitted).

We calculated the AD cross section for the partial waves $J = 0, \ldots, 60$ for all additional models. The modification of the threshold exponent in the models NRM3 and NRM4 do not have a large impact on the shape of the cross sections expect for a very abrupt threshold behaviour of the results from the NRM4, see Figures 5.14 and 5.15, where the partial wave $J = 0$ and the total AD cross

section are shown respectively. Although, the fitted eigenphase sums of the NRM1 and NRM2 are very similar, the results noticeably differ. The real difference is distorted due to the use of the logarithmic scale. The total AD cross section for the NRM2 is more than twice the size of the total cross section obtained from NRM1. Furthermore, sharp threshold structures are significantly suppressed in the results obtained from the NRM2. The explanation of the disagreement is following. The R-dependent coefficients of the resonance width serve as well as an extrapolation in the vicinity of the crossing point, where no *ab initio* data are available (Section 2.4). To compare the models we calculated the eigenphase sum at internuclear distances closer to the crossing point $R_c = 6.7$, specifically at $R = 5.0, 5.5, 6.0$, and 6.5, see Figure 5.16, where the resonant eigenphase sum (without the background) is shown. The mutual differences get bigger as we approach to the crossing point. The eigenphase sums for the models NRM3 and NRM4 slightly differ from the original model NRM1, which is consistent with the very similar shape of the corresponding total cross sections.

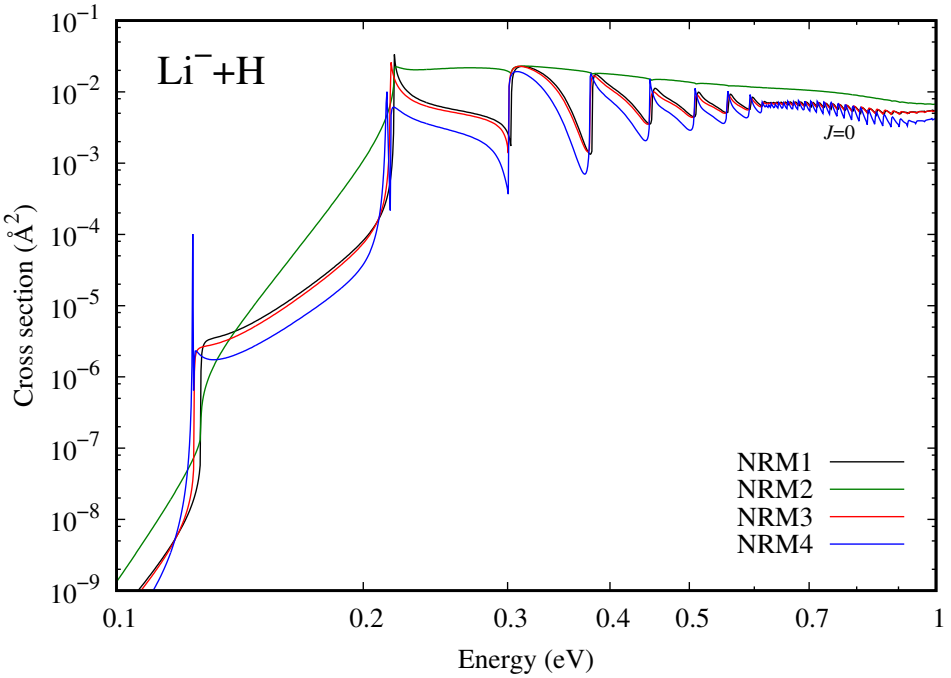

Figure 5.14: The AD cross section of the Li^-+H collision for the partial wave $J = 0$ obtained from all proposed nonlocal models NRM1 (original model), NRM2, NRM3, and NRM4 in the logarithmic scale.

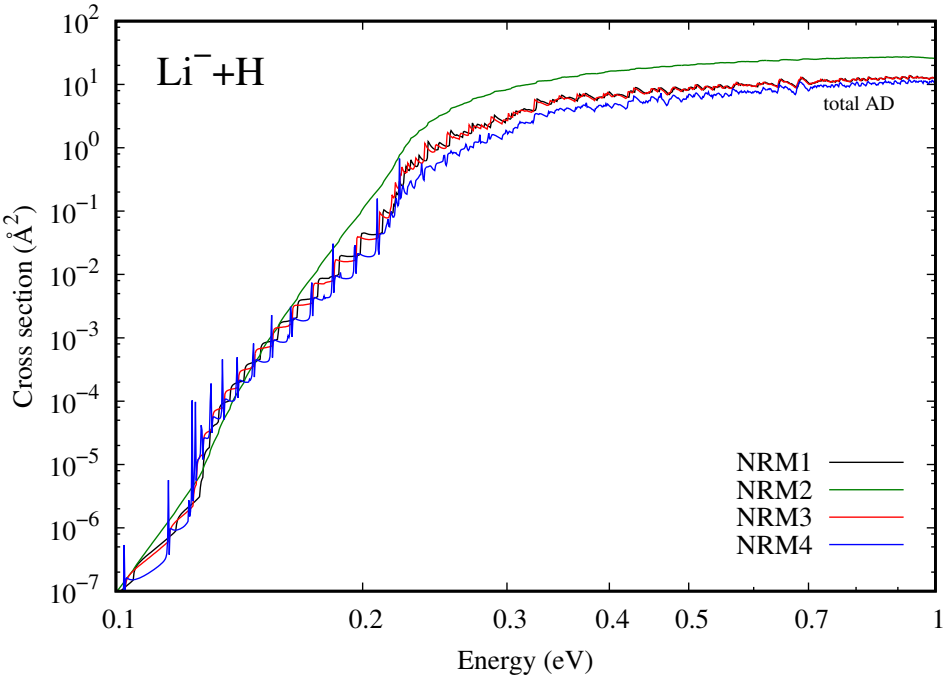

Figure 5.15: The total AD cross section of the Li^-+H collision obtained from all proposed nonlocal models NRM1 (original model), NRM2, NRM3, and NRM4 in the logarithmic scale.

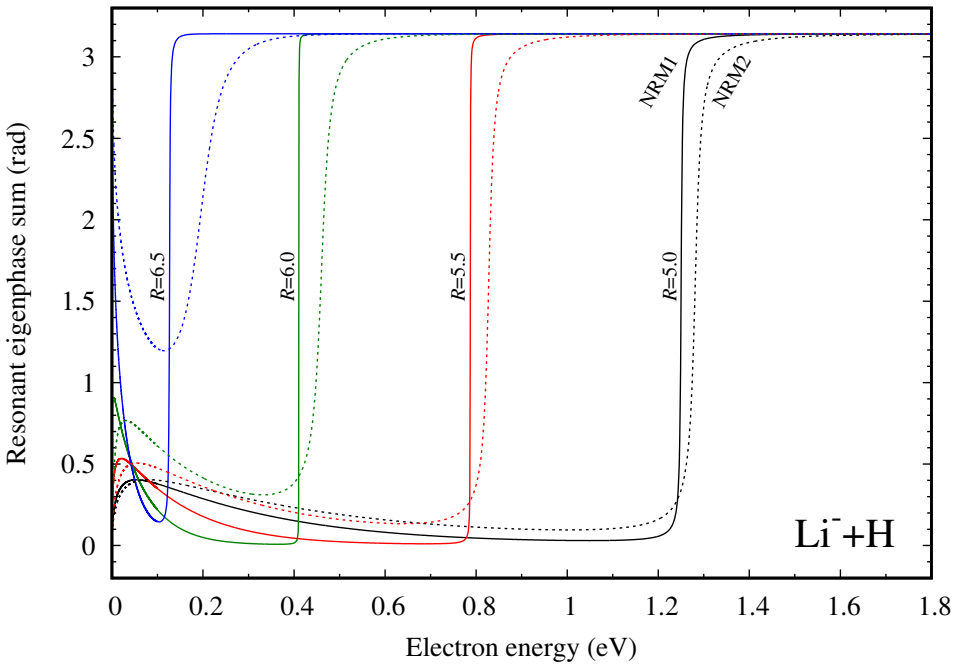

Figure 5.16: The resonant eigenphase sum of the Li^-+H collision obtained from the nonlocal models NRM1 (original model, solid curves) and NRM2 (dashed) at the internuclear distances $R = 5.0, 5.5, 6.0, 6.5$ (from right to left), which are close to the crossing point at $R_c = 6.7$, where no scattering data are available.

The vicinity of the crossing point is usually important in order to obtain the quantitatively correct results. We can estimate the influence of the immediate vicinity from classical physics. Let us consider a classical particle with the reduced mass of LiH ($\mu = 1605.5871$ [28]) and with certain energy E moving in the potential of the discrete state $V_\mathrm{d}(R)$. The particle bounces back at the point where $E = V_\mathrm{d}(R)$. We compute time which the particle spends in the region $R < R_\mathrm{c}$ and we compare it with mean lifetime of the resonance at such R_0, where $E = V_\mathrm{d}(R_0)$. If the time is greater or equal to the mean lifetime, we can assume that the particle probably decays. Then, the region of $R_0 < R < R_\mathrm{c}$ is substantial in the description of associative detachment processes and the region $R < R_0$ is only reached by tunnelling.

The calculation is quite simple. The kinetic energy of the considered particle is given by

$$T_\mathrm{kin}(R) = E - V_\mathrm{d}(R) = \frac{1}{2}\mu v(R)^2. \tag{5.12}$$

The velocity $v(R)$ of the particle then equals

$$v(R) = \sqrt{\frac{2(E - V_\mathrm{d}(R))}{\mu}} \tag{5.13}$$

The particle spends time τ between points R_1 and R_2 as follows

$$\tau = \int_{R_1}^{R_2} \frac{\mathrm{d}R}{v(R)} = \int_{R_1}^{R_2} \sqrt{\frac{\mu}{2(E - V_\mathrm{d}(R)}}\mathrm{d}R. \tag{5.14}$$

Mean lifetime τ_res [5] of a resonance with a width Γ is given by

$$\tau_\mathrm{res} = \frac{\hbar}{\Gamma}. \tag{5.15}$$

The known resonance which is the nearest to the crossing point is the resonance which appears in the eigenphase sum at $R = 4.6$, see Figures 2.3 or 5.13. The resonance is not well described by the fitted model. To obtain more precise width, we fitted the eigenphase sum at $R = 4.6$ by the energy-independent Breit-Wigner formula with a logarithmically-dependent background term

$$\delta(\epsilon) = A\log(\epsilon) + B - \tan^{-1}\left(\frac{\Gamma/2}{\epsilon - E_\mathrm{R}}\right), \tag{5.16}$$

where E_R determines the position of the resonance and constants A, B are parameters of the background. The coefficients were determined by means of the least squares. Specifically, we are interested only in the width, which is equal to $\Gamma = 7.44 \times 10^{-3}$ eV. Thus, the mean lifetime[1] equals $\tau_\mathrm{res} = 0.88 \times 10^{-13}$ s.

We considered the energy of the particle E and the points R_1, R_2 to be equal to $E = V_\mathrm{d}(R = 4.6) = 0.642$ eV, $R_1 = 4.6$ and $R_2 = R_\mathrm{c} = 6.7$. The time which the particle spends in this region is $\tau = 0.20 \times 10^{-13}$ s.

[1]Here, we list necessary physical constants and unit conversions [41]: the reduced Planck constant $\hbar = 6.58\times10^{-16}$ eV·s, the mass of electron $m_\mathrm{e} = 9.11\times10^{-31}$ kg, 1 eV $= 1.60\times10^{-19}$ J, and 1 bohr $= 0.53 \times 10^{-10}$ m.

We keep in mind that the result is just an estimate based on classical physics but it provides a good insight into the scattering problem. The time which the particle spends in the region where the nonlocal potential is mostly located is less than the mean lifetime of the resonance at $R = 4.6$, since the resonance is very narrow. We conclude that the electron autodetachment is not very efficient in this region of internuclear distances and the quantum mechanics description involving details of the coupling potential and nonlocal effects is important to obtain the exact magnitude of the cross sections.

5.6 Local approximation

The cross sections given by the models NRM3 and NRM4 differ only slightly from the original model NRM1. Therefore, we consider only the NRM1 and NRM2 in the further discussion.

The local approximation (LCP) is defined by Equations (1.62) to (1.65). In this collision, we can calculate cross sections within this approach. Equation (1.65), which gives resonant energy, is a non-linear equation and it does not have a unique solution in the vicinity of the crossing in the case of polar molecules [3]. Three roots exist there. These solutions represent poles of the K-matrix and they define the position of the resonance of LiH^- in the continuum ($R < R_c$) and the position of the bound state at $R > R_c$. To find the resonant energy, that is to solve Equation (1.65), the bisection method [35] was used.

We determined the local complex potentials for the models NRM1 and NRM2. The real part defined by Formula (1.63) and the imaginary part $-\Gamma_{loc}/2$ given by Formula 1.64 can be seen in Figures 5.17 and 5.18. The potential energy curve of the anion state given by poles of the K-matrix is continuous. The 'bend back' of the potential given by three solutions of Equation (1.65) is caused by the long-range dipole interaction. In fact, if the dipole is supercritical, the point of turnover on the threshold (neutral potential) is at $R \to 0$. We do not observe this behaviour here since our models do not include the proper threshold behaviour of a supercritical dipole moment (threshold exponent is complex). The 'loops' in the imaginary part around the crossing point $R_c = 6.7$ are again caused by the non-uniqueness of the solution of Equation (1.65). We refer the reader to the cited review by Domcke [3], where situations for differently strong dipoles are discussed in great detail as well as the comparison with poles of the S-matrix.

To be able to calculate cross sections in the local approximation, we omitted the region where three solutions exist and we interpolated the potentials by cubic splines in this interval. We entirely ignored the 'loop' in the imaginary part.

We solved the radial Schrödinger equation[2] [42] with the local complex potential $W_{loc}(R)$ defined by Equations (1.62) to (1.65)

$$\left[\frac{\mathrm{d}^2}{\mathrm{d}R^2} + K^2 - \frac{J(J+1)}{R^2} - 2\mu W_{loc}(R)\right] u_J(R) = 0, \tag{5.17}$$

where $K = \sqrt{2\mu E}$ is the wave number belonging to energy E. The radial wave function $u_J(R)$ obeys the boundary condition $u_J(R = 0) = 0$. The Schrödinger equation was solved using the Numerov algorithm [43]. Cross sections can be

[2]The Lippman-Schwinger equation with the same potential can be solved as well.

again determined by Formula (1.51) from scattering in a complex potential. In this case, the scattering amplitude a_J [9] is equal to

$$a_J = \mathrm{e}^{\mathrm{i}\gamma}\sin\gamma, \tag{5.18}$$

where γ is complex phase shift, which can be computed from asymptotic behaviour

$$u_J(R) \xrightarrow{R\to\infty} \sin\left(KR - \frac{\pi}{2}J + \gamma\right). \tag{5.19}$$

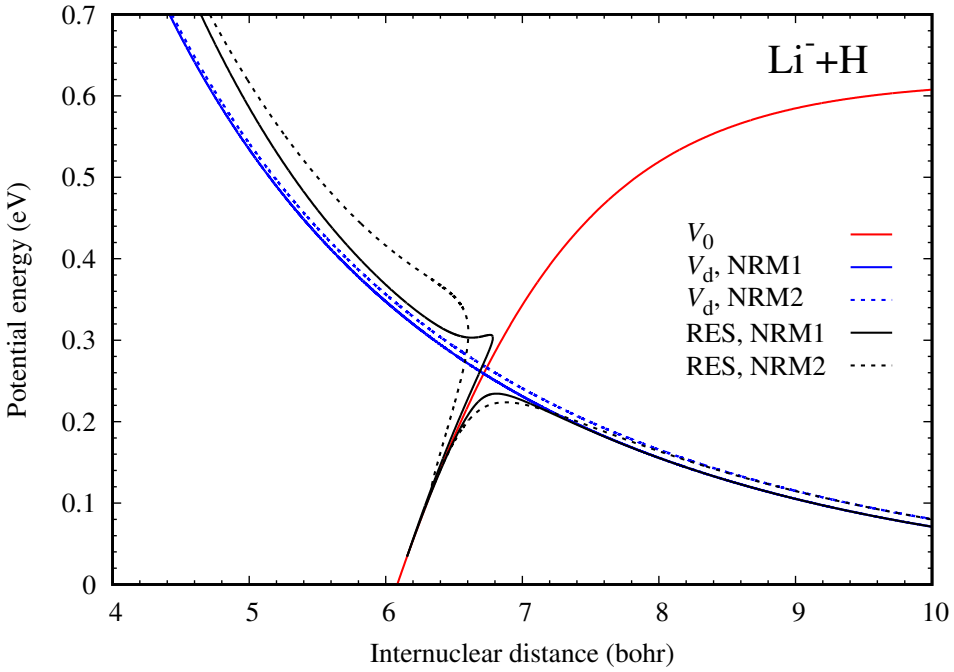

Figure 5.17: The real part of the local complex potential determined as poles of the K-matrix for the models NRM1 (black solid) and NRM2 (black dashed) of the Li^-+H collision in the vicinity of the crossing of the neutral potential (red) and the discrete state potential (blue solid curve for NRM1, blue dashed for NRM2).

We calculated the AD cross sections in the local approximation for the partial waves $J = 0, \ldots, 60$ for the models NRM1 and NRM2. The results for the original model NRM1 can be seen in Figure 5.19. The local result is smaller almost by one order of magnitude in comparison with the nonlocal total cross section from the same model. As we mention earlier, the qualitative shape is well described by the local approximation but no Wigner cusps appear owing to the energy independence of the local complex potential.

In the end, we compare the nonlocal and local results (Figure 5.20). There is no such distinct difference in the nonlocal and local result in the case of NRM2. The nonlocal cross section is approximately three times larger at high energies and it is even smaller at very low energies. It seems that the nonlocal effects are essential. The local approximation gives quantitatively very different results. However, the omission of the 'loops' in Γ_{loc} may have significant consequences to the magnitude of the local cross sections.

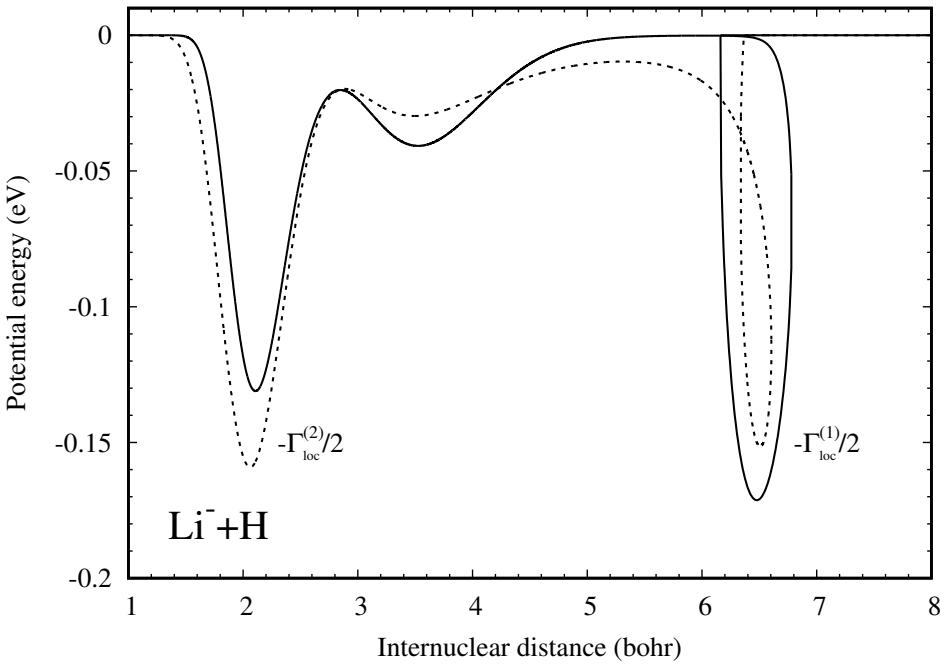

Figure 5.18: The imaginary part of the local complex potential $-\Gamma_{\rm loc}/2$ of the Li^-+H collision for the models NRM1 (solid curve) and NRM2 (dashed).

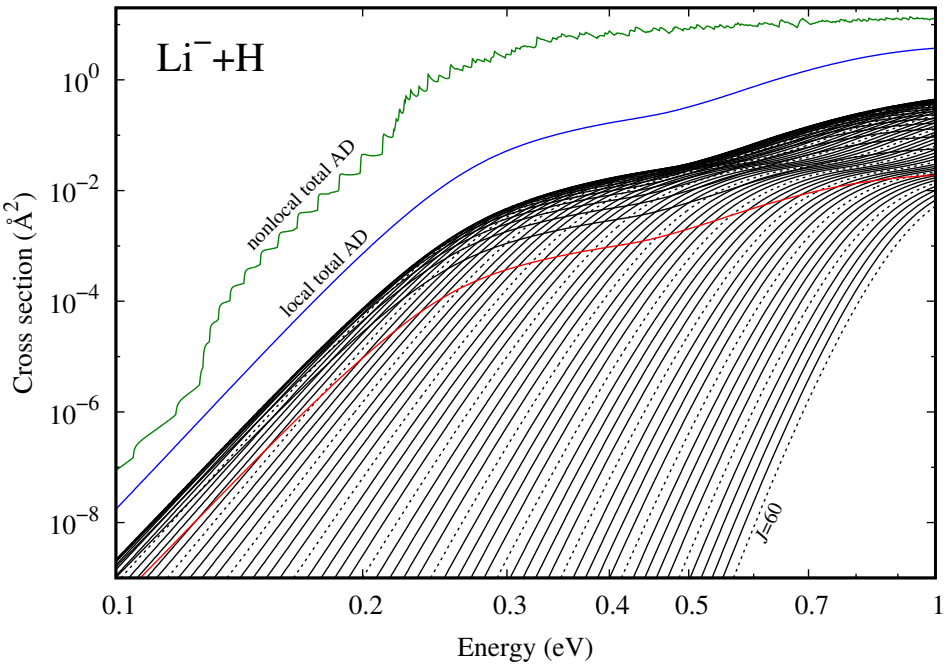

Figure 5.19: The AD cross sections of the Li^-+H collision for the partial waves $J = 0, \ldots, 60$ obtained from the local approximation (first from bottom to top, then from left to right, $J = 0$ red, every fifth is dashed starting from $J = 5$), the total local AD (blue) and the total nonlocal AD (green) cross sections in the logarithmic scale. All curves are determined from the original model NRM1.

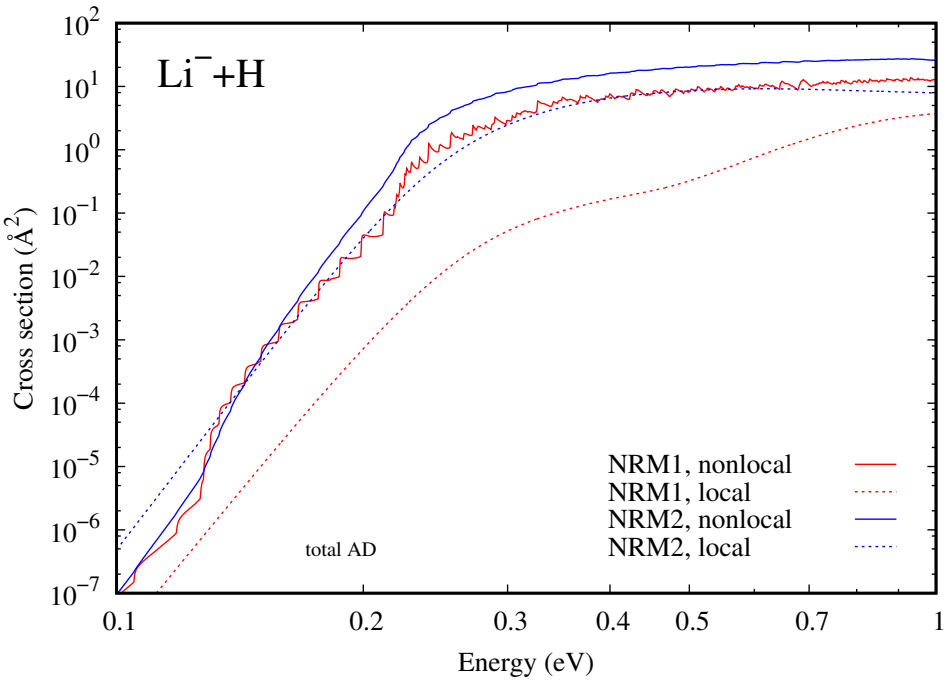

Figure 5.20: The comparison of the nonlocal and local total AD cross sections of the Li^-+H collision obtained from the models NRM1 and NRM2 in the logarithmic scale.

5.7 Rate constant

We end the analysis of the Li^-+H collision by the discussion of rate constant. In this case, there is no problem with the integration of sharp peaks since orbital resonances do not exist. We are limited by the energy interval [0.1,1] eV, where the cross sections were calculated, only at high temperatures because the total cross section is an increasing function of energy. The region above 1 eV starts to contribute at temperatures $T \geq 1500$ K (Figure 5.21). Some extrapolation of the cross section above 1 eV (perhaps a constant function) can be used but again we will no longer deal with it.

The rate constant of the Li^-+H collision rapidly increases at low temperature, which is related to the behaviour of the cross section, see Figure 5.22, where we compare the nonlocal and local results (the vertical axis is in the logarithmic scale).

The temperature-independent rate constant of the Li^-+H collision was estimated by Stancil et al. [14] to the same value 4×10^{-10} cm^3s^{-1} as in the case of the Li+H^- collision. We predict much smaller rate constant (by many orders of magnitude) at temperatures below 1000 K. At temperatures above 1500 K the results from nonlocal calculations are probably not very different from the estimate, but as we mention, data for cross sections at higher energies are needed, which involves the inclusion of the dissociation channel to our description of the studied process. The differences among the nonlocal and local results are given by the various magnitude of the cross sections. The uncertainty of the rate constant with respect to the different nonlocal models persists and it have to be removed in future work by better description of the vicinity of the crossing, which mainly

depends on obtaining the scattering data in this region.

The significant difference between the rate constants of the studied AD processes, compare the results in Figures 4.20 and 5.22, is expected from the shapes of the anion potentials. The ground anion potential ($X^2\Sigma^+$ state), which participates in the Li+H$^-$ collision, is attractive at some nuclear configurations. On the other hand, the first excited anion potential ($A^2\Sigma^+$ state), which is involved in the description of the Li$^-$+H channel, is repulsive at all internuclear distances, which corresponds with the suppression of the cross section and rate constant at low energies and temperatures respectively.

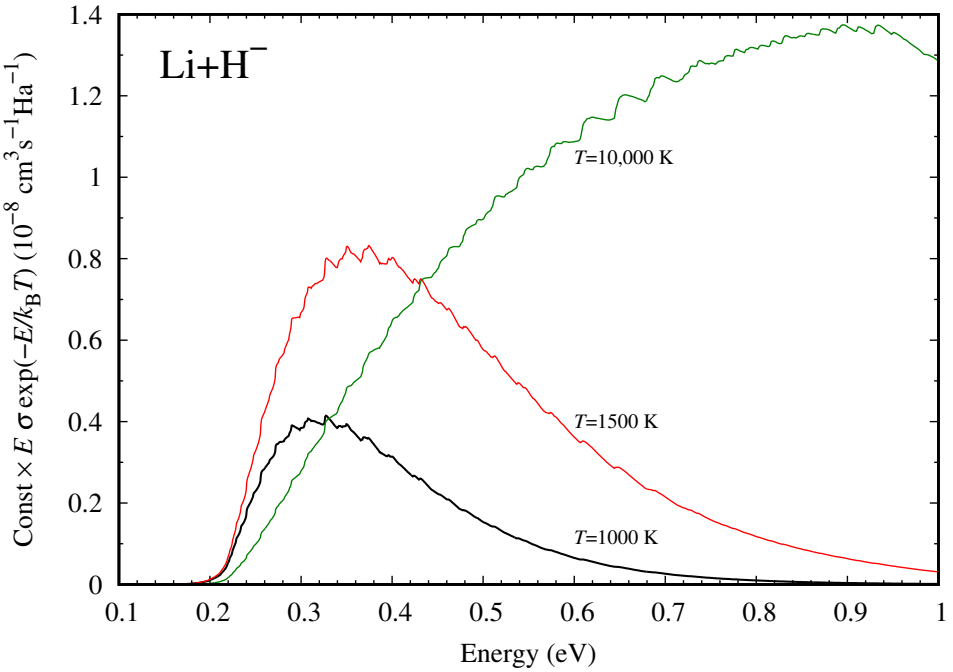

Figure 5.21: The integrand of the rate constant integral at temperatures $T = 1000, 1500$ and 10,000 K (black, red and green curves respectively) with the total AD cross section obtained from the nonlocal model NRM2 of the Li$^-$+H collision.

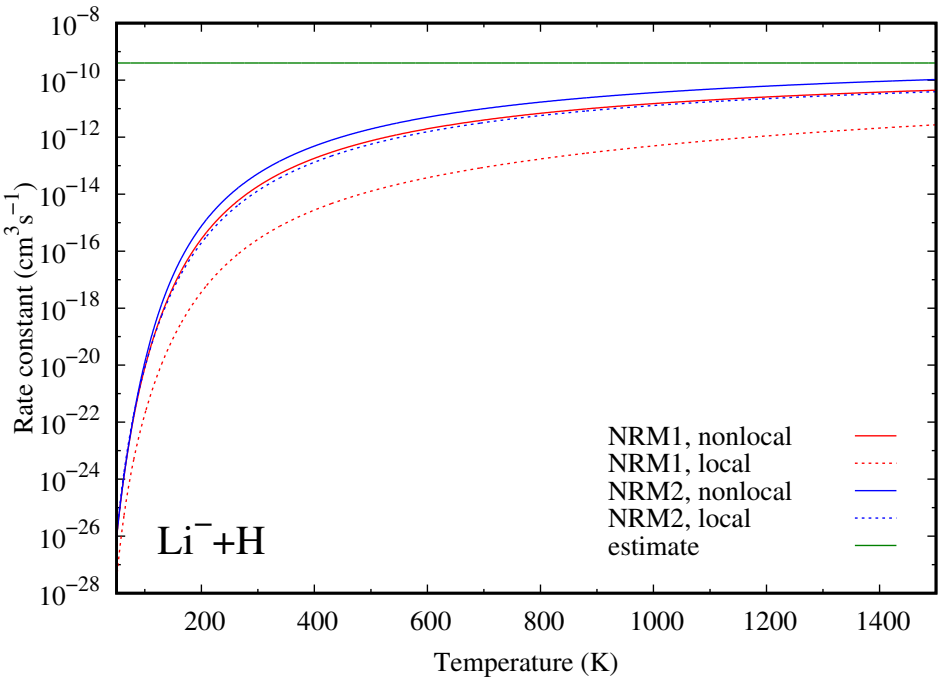

Figure 5.22: The temperature-dependent rate constant of the Li^-+H collision calculated from the nonlocal and local total AD cross sections for the models NRM1 and NRM2. The temperature-independent estimate made by Stancil et al. [14] is also shown as the horizontal green line. The vertical axis is in the logarithmic scale.

Conclusion

In this master thesis, we performed the first calculation of the cross sections and temperature-dependent rate constants of the associative detachment processes of Li with H^- and H with Li^- within the nonlocal resonant theory but without the full inclusion of the low-energy behaviour of scattering quantities due to the supercritical dipole moment of the molecule LiH. The calculations involved the construction of the nonlocal resonant models from the potential energy curves of LiH and LiH^- and from the eigenphase sum of electron-LiH scattering.

The separability of the nonlocal potential (or coupling potential) is necessary to the effective calculation of cross sections but the constructed coupling potentials are not separable in energy and space variables. Therefore, we developed the new method, which approximates these couplings by the sum of several separable terms, to shorten computational times. The proposed procedure written in Fortran 95 consists of two steps. First, the coupling is evaluated on the properly chosen energy and space grids and the resulting matrix is decomposed by the singular value decomposition method. In the second step, the SVD energy-dependent functions are fitted by an appropriate simple function, which allows us to use the analytic formula of integral transform in the evaluation of the nonlocal potential.

The separation method worked very well in the case of the Br^-+H collision (test example) and the Li+H^- collision, but it turned out to be unusable for the Li^-+H collision because of the problems in the fitting procedure, which may be related to the supercriticility of the dipole moment of LiH. We performed these calculations without any coupling separation, which results in the significant but manageable increase of computational time. The improvement of the fitting procedure is possible. The replacement of the polynomial in the fitting function by a rational function may provide a comparable approximation of the data with better numerical stability and possibly with less parameters.

The use of the nonlocal theory was not typical in the case of the Li+H^- channel because the corresponding state of LiH^- is not embedded in the electronic continuum. The anion state is bound for all nuclear configurations but the non-adiabatic coupling is involved due to the close proximity of this anion state to the continuum threshold. We found out that the description of this collision with various choices of the discrete state is equivalent since the final results differ only slightly.

In the Li^-+H channel, we found out the uncertainty given by a factor two in the magnitude of the results for two different nonlocal models, which are consistent with the *ab initio* data. The difference is mainly caused by the fact that, unfortunately, no scattering data from the vicinity of the crossing of the neutral and anion potentials were available to us, and the models provide different extrapolations in this region. The local approximation is not capable of the quantitatively correct description of the cross sections in the Li^-+H case. The results differ several times from the nonlocal calculations.

In contrast to data used in cosmological simulations [1], our calculations predict the considerable difference in the magnitude of the rate constants of the studied collisions. The result of the Li+H^- collision is a decreasing function of

temperature. Its magnitude is smaller but of the same order of magnitude at temperatures below 1000 K as the temperature-independent estimate, the only available independent result. The rate constant of the Li^-+H collision rapidly increases with temperature and it is smaller by several orders of magnitude than the result of the other channel at temperatures below 1000 K.

In future we plan to improve the scattering data close to the crossing point and to fully include the supercritical dipole moment to the description of processes within the nonlocal resonant theory. It means that we have to most likely consider the infinite series of bound dipole states in the system of LiH+e^-, which requires the change of the parametrization of the electronic Hamiltonian. The resonant part should remain unchanged but the background part should be expanded by energies of the dipole bound states, which implies the appearance of an coupling of the discrete and dipole states. It is possible that considering only one dipole state would be sufficient because the dipole energies converge exponentially fast to the threshold energy.

Bibliography

[1] S. Lepp, P. C. Stancil, and A. Dalgarno. Atomic and molecular processes in the early Universe. *Journal of Physics B: Atomic, Molecular and Optical Physics*, 35:R57–R80, 2002.

[2] S. C. O. Glover, J. Chluba, S. R. Furlanetto, J. R. Pritchard, and D. W. Savin. Atomic, Molecular and Optical Physics in the early Universe: From Recombination to Reionization. *Advances in Atomic, Molecular, and Optical Physics*, 63:135–270, 2014.

[3] W. Domcke. Theory of resonance and threshold effects in electron-molecule collisions: The projection-operator approach. *Physics Reports (Review Section of Physics Letters)*, 208(2):97–188, 1991.

[4] P. Čársky and R. Čurík, editors. *LOW-ENERGY ELECTRON SCATTERING from MOLECULES, BIOMOLECULES and SURFACES*. CRC Press, 2012.

[5] J. R. Taylor. *Scattering Theory: The Quantum Theory on Nonrelativistic Collisions*. John Wiley & Sons, Inc., 1972.

[6] H. Feshbach. A unified theory of nuclear reactions II. *Annals of Physics*, 19(2):287–313, 1962.

[7] U. Fano. Effects of configuration interaction on intensities and phase shifts. *Physical Review*, 124(6):1866–1878, 1961.

[8] M. Abramowitz and I. A. Stegun, editors. *Handbook of Mathematical Functions with Formulas, Graphs, and Mathematical Tables*. New York: Dover Publications, tenth edition, 1972.

[9] M. Čížek. *RESONANT PROCESSES IN ATOMIC COLLISIONS - theoretical considerations and calculations*. PhD thesis, The Faculty of Mathematics and Physics, Charles University in Prague, 1999.

[10] E. P. Wigner. On the Behaviour of Cross Sections Near Thresholds. *Physical Review*, 73(9):1002–1009, 1948.

[11] O. H. Crawford. Bound states of a charged particle in a dipole field. *Proceedings of the Physical Society*, 91(2):279–284, 1967.

[12] I. I. Fabrikant. Long-range effects in electron scattering by polar molecules. *Journal of Physics B: Atomic, Molecular and Optical Physics*, 49:1–20, 2016.

[13] M. Čížek, J. Horáček, M. Allan, I. I. Fabrikant, and W. Domcke. Vibrational excitation of hydrogen fluoride by low-energy electrons: theory and experiment. *Journal of Physics B: Atomic, Molecular and Optical Physics*, 36:2837–2849, 2003.

[14] P. C. Stancil, S. Lepp, and A. Dalgarno. The lithium chemistry of the early Universe. *Astrophysical Journal*, 458:401–406, 1996.

[15] P. F. Bernath. *Spectra of Atoms and Molecules.* Oxford University Press, 1995.

[16] F. X. Gadéa and T. Leininger. Accurate ab initio calculations for LiH and its ions, LiH^+ and LiH^-. *Theoretical Chemistry Accounts*, 116:566–575, 2006.

[17] H.-J. Werner, P. J. Knowles, G. Knizia, F. R. Manby, M. Schütz, et al. MOLPRO, version 2012.1, a package of ab initio programs. See http://www.molpro.net.

[18] H.-J. Werner and P. J. Knowles. A second order multiconfiguration SCF procedure with optimum convergence. *Journal of Chemical Physics*, 82:5053, 1985.

[19] H.-J. Werner and P. J. Knowles. An efficient internally contracted multiconfiguration–reference configuration interaction method. *Journal of Chemical Physics*, 89:5803, 1988.

[20] T. H. Dunning Jr. Gaussian basis sets for use in correlated molecular calculations. I. The atoms boron through neon and hydrogen. *Journal of Chemical Physics*, 90:1007, 1989.

[21] M. Puchalski, D. Kędziera, and K. Pachucki. Lithium electric dipole polarizability. *Physical Review A*, 84:052518–1–9, 2011. Erratum *Phys. Rev. A* 85, 019910, 2012.

[22] J. C. Rienstra-Kiracofe, G. S. Tschumper, H. F. Schaefer, S. Nandi, and G. B. Ellison. Atomic and Molecular Electron Affinities: Photoelectron Experiments and Theoretical Computations. *Chemical Review*, 102:231–282, 2002.

[23] J. Tennyson. Electron-molecule collision calculations using the R-matrix method. *Physics Report*, 491:29–76, 2010.

[24] L. A. Morgan, J. Tennyson, and C. J. Gillan. The UK molecular R-matrix codes. *Computer Physics Communications*, 114:120–128, 1998.

[25] J. M. Carr, P. G. Galiatsatos, J. D. Gorfinkiel, A. G. Harvey, M. A. Lysaght, D. Madden, Z. Mašín, M. Plummer, J. Tennyson, and H. N. Varambhia. UKRmol: a low-energy electron- and positron-molecule scattering suite. *European Physical Journal D*, 66:58, 2012.

[26] H. Friedrich. *Scattering Theory.* Springer, 2013.

[27] W. Domcke. Projection-operator approach to potential scattering. *Physical Review A*, 28:2777, 1983.

[28] S. Bubin and L. Adamowicz. Nonrelativistic molecular quantum mechanics without approximations: Electron affinities of LiH and LiD. *Journal of Chemical Physics*, 121(13):6249–6253, 2004.

[29] M. Čížek, J. Horáček, A.-Ch. Sergenton, D. B. Popović, M. Allan, W. Domcke, T. Leininger, and F. X. Gadea. Inelastic low-energy electron collisions with the HBr and DBr molecules: Experiment and theory. *Physical Review A*, 63:062710–1–14, 2001.

[30] H.-D. Meyer, J. Horáček, and L. S. Cederbaum. Schwinger and anomaly-free Kohn variational principles and a generalized Lanczos algorithm for nonsymmetric operators. *Physical Review A*, 43(7):3587–3596, 1991.

[31] S. K. Adhikari and I. H. Sloan. Separable operator expansion for the T-matrix. *Nuclear Physics A*, 241:429–442, 1975.

[32] H. Bateman. On the numerical solution of linear integral equations. *Proceedings of the Royal Society London Series A*, 100:441–449, 1922.

[33] K. Houfek, M. Čížek, and J. Horáček. Dissociative attachment of low-energy electrons to vibrationally excited hydrogen molecules. *Czechoslovak Journal of Physics*, 52(1):29–40, 2002.

[34] J. Horáček, M. Čížek, and W. Domcke. Generalization of the nonlocal resonance model for low-energy electron collisions with hydrogen halides: the variable threshold exponent. *Theoretical Chemistry Accounts*, 100:31–35, 1998.

[35] W. H. Press, S. A. Teukolsky, W. T. Vetterling, and B. P. Flannery. *Numerical Recipes in C: The Art of Scientific Computing*. Cambridge University Press, Second edition, 1992.

[36] W. Domcke and C. Mündel. Calculation of cross sections for vibrational excitation and dissociative attachment in HCl and DCl beyond the local-complex-potential approximation. *Journal of Physics B*, 18(22):4491–4509, 1985.

[37] A. S. Dickinson and P. R. Certain. Calculation of Matrix Elements for One-Dimensional Quantum-Mechanical Problems. *Journal of Chemical Physics*, 49(9):4209, 2003.

[38] J. Horáček and W. Domcke. Calculation of cross sections for vibrational excitation and dissociative attachment in electron collisions with HBr and DBr. *Physical Review A*, 53(4):2262–2271, 1996.

[39] J. Horáček, F. Gemperle, and H.-D. Meyer. Calculation of dissociative attachment of electrons to diatomic molecules by the Schwinger-Lanczos approach. *Journal of Chemical Physics*, 104(21):8433–8441, 1996.

[40] J. A. Fedchak, R. L. Champion, L. D. Doverspike, and Yicheng Wang. Slow collisions of Na^- and K^- with atomic hydrogen. *Journal of Physics B*, 27(14):3045, 1994.

[41] E. R. Cohen and B. N. Taylor. The 1986 adjustment of the fundamental physical constants. *Reviews of Modern Physics*, 59(4):1121–1148, 1987.

[42] B. H. Bransden and C. J. Joachain. *Physics of atoms and molecules*. Longman Scientific & Technical, 1983.

[43] S. E. Koonin and D. C. Meredith. *COMPUTATIONAL PHYSICS - Fortran Version*. Westview Press, 1990.